

# Electrical control of quantum dot spin qubits

A dissertation presented  
by

Edward Alexander Laird

to  
The Department of Physics  
in partial fulfillment of the requirements  
for the degree of  
Doctor of Philosophy  
in the subject of

Physics

Harvard University  
Cambridge, Massachusetts

2009

© 2009 by Edward Alexander Laird  
All rights reserved.

## Electrical control of quantum dot spin qubits

### Abstract

This thesis presents experiments exploring the interactions of electron spins with electric fields in devices of up to four quantum dots. These experiments are particularly motivated by the prospect of using electric fields to control spin qubits.

A novel hyperfine effect on a single spin in a quantum dot is presented in Chapter 2. Fluctuations of the nuclear polarization allow single-spin resonance to be driven by an oscillating electric field. Spin resonance spectroscopy revealed a nuclear polarization built up inside the quantum dot device by driving the resonance.

The evolution of two coupled spins is controlled by the combination of hyperfine interaction, which tends to cause spin dephasing, and exchange, which tends to prevent it. In Chapter 3, dephasing is studied in a device with tunable exchange, probing the crossover between exchange-dominated and hyperfine-dominated regimes. In agreement with theoretical predictions, oscillations of the spin conversion probability and saturation of dephasing are observed.

Chapter 4 deals with a three-dot device, suggested as a potential qubit controlled entirely by exchange. Preparation and readout of the qubit state are demonstrated, together with one out of two coherent exchange operations needed for arbitrary manipulations. A new readout technique allowing rapid device measurement is described.

In Chapter 5, an attempt to make a two-qubit gate using a four-dot device is presented. Although spin qubit operation has not yet been possible, the electrostatic interaction between pairs of dots was measured to be sufficient in principle for coherent qubit coupling.

# Contents

Abstract . . . . .	iii
Table of Contents . . . . .	iv
List of Figures . . . . .	vi
Acknowledgements . . . . .	vii
<b>1 Introduction</b>	<b>1</b>
1.1 Organization of this thesis . . . . .	2
1.2 Quantum computing . . . . .	3
1.3 GaAs heterostructures, quantum dots and charge sensing . . . . .	4
1.4 Double quantum dots and spin blockade . . . . .	8
1.5 Electron spin resonance . . . . .	10
1.6 The singlet-triplet basis . . . . .	12
1.7 Summary of contributions . . . . .	14
<b>2 Gate-driven hyperfine-mediated electron spin resonance</b>	<b>16</b>
2.1 Introduction . . . . .	17
2.2 Device and measurement . . . . .	18
2.3 EDSR spectroscopy . . . . .	21
2.4 Theory . . . . .	24
2.4.1 Comparison with data . . . . .	26
2.5 Nuclear polarization . . . . .	28
2.6 Addressing individual spins . . . . .	29
2.7 Open issues and discussion . . . . .	31
<b>3 Effect of Exchange Interaction on Spin Dephasing in a Double Quantum Dot</b>	<b>33</b>
3.1 Introduction . . . . .	34
3.2 Device . . . . .	36
3.3 Methods . . . . .	36
3.4 Measurement of exchange energy, hyperfine interaction strength and readout visibility . . . . .	38
3.5 Saturation singlet probability . . . . .	40
3.6 Time-dependence of the singlet probability . . . . .	42
3.7 Summary and acknowledgements . . . . .	43
<b>4 Coherent operation of an exchange-only qubit</b>	<b>45</b>
4.1 Introduction . . . . .	46
4.2 Exchange in a three-spin system . . . . .	47

4.3	Device and methods . . . . .	49
4.4	Coherent exchange in a triple dot . . . . .	52
4.5	Conclusion and acknowledgements . . . . .	53
<b>5</b>	<b>Towards a two-qubit gate in the singlet-triplet basis</b>	<b>54</b>
5.1	Introduction . . . . .	55
5.2	Device and methods . . . . .	57
5.3	Measuring the coupling . . . . .	59
5.4	Summary and outlook . . . . .	59
<b>A</b>	<b>Fabrication recipe</b>	<b>61</b>
A.1	Introduction . . . . .	61
A.2	Generic photolithography recipe . . . . .	61
A.3	Complete fabrication procedure . . . . .	62
A.3.1	Mesa etch . . . . .	62
A.3.2	Ohmic contacts . . . . .	62
A.3.3	Gate pads . . . . .	63
A.3.4	Fine gates . . . . .	63
<b>B</b>	<b>Constructing and using a multiplexed reflectometry setup</b>	<b>65</b>
B.1	Hardware inside the cryostat . . . . .	65
B.2	Hardware outside the cryostat . . . . .	69
B.2.1	The demodulation box . . . . .	71
B.3	Igor code . . . . .	72
B.3.1	do2dfast() . . . . .	73
B.3.2	tuneg() . . . . .	74
B.3.3	calsensor() . . . . .	75
B.4	Tuning hints . . . . .	76
<b>C</b>	<b>Synchronizing two Tektronix AWG520s</b>	<b>80</b>

# List of Figures

1.1	Heterostructures and quantum dots . . . . .	5
1.2	Charge quantization and charge sensing . . . . .	6
1.3	Double quantum dots . . . . .	7
1.4	Spin blockade . . . . .	8
1.5	Electron spin resonance . . . . .	10
1.6	Bloch sphere in the singlet-triplet basis . . . . .	13
2.1	Measurement setup and pulse scheme . . . . .	18
2.2	Spin resonance signal as a function of magnetic field and microwave frequency	21
2.3	Spin resonance signal as a function of time, magnetic field and microwave power . . . . .	22
2.4	Nuclear polarization driven and detected via EDSR . . . . .	28
2.5	EDSR signal in a device incorporating a micromagnet . . . . .	30
2.6	An additional half-frequency EDSR line . . . . .	31
3.1	Level diagram and pulse scheme . . . . .	35
3.2	Exchange measured as a function of detuning . . . . .	37
3.3	Saturation singlet probability . . . . .	41
3.4	Singlet probability as a function of time . . . . .	43
4.1	An exchange-only qubit . . . . .	47
4.2	Electron states of a triple quantum dot . . . . .	48
4.3	Fast measurements with two charge sensors . . . . .	50
4.4	Coherent spin exchange . . . . .	52
5.1	A capacitive two-qubit interaction . . . . .	56
5.2	Charge stability diagrams . . . . .	57
5.3	Measuring the coupling . . . . .	58
B.1	Reflectometry cryostat . . . . .	66
B.2	Cold finger and sample PC board . . . . .	69
B.3	Room temperature measurement schematic . . . . .	70
B.4	Demodulation box . . . . .	72

# Acknowledgements

After seven years of excitement, confusion, frustration, fatigue, serendipity, and a fair few occasions when I thought I would never finish<sup>1</sup> it is a great pleasure to look back over my graduate school experience and remember the people whose help was essential to my PhD.

First I would like to thank my advisor, Charlie Marcus. Charlie's high standards and strong aesthetic sense were inspirational throughout my time working for him, and kept me on a path of maximal PhD enjoyment globally no matter how disordered the topography locally. As well as constantly supplying interesting problems to work on, Charlie provided great practical help in resolving them through his endless inventiveness, willingness to advise on almost any level of detail, and dedication to keeping the lab well-equipped and efficient.

I would also like to thank my committee members, Micha Lukin and Eugene Demler, for asking pertinent, interesting questions, and for stimulating lectures.

Two theorists with whom I collaborated closely were Jake Taylor and Emmanuel Rashba. I am grateful to both of them for generously sharing their knowledge with me and for tirelessly immersing themselves in the details of our ongoing projects.

The experiments described here relied heavily on the exceptionally quiet wafers from Art Gossard's MBE machines at Santa Barbara. I would like to thank the student who grew them, Micah Hanson, collaborator on every one of my papers; perhaps we will get to meet one day.

Within the Marcuslab, I have been enormously helped and educated by interacting with knowledgeable, enthusiastic people. I am especially grateful to three senior students and postdocs I worked with during my first four years. Dominik Zumbühl patiently taught me

---

<sup>1</sup>Usually in the McKay basement in the small hours of the morning.

fabrication and measurement. Jason Petta mentored me through my first successful experiment and set an example of efficient research that I am still trying to emulate. David Reilly brought not only the revolutionary technology of fast readout but also a wide knowledge of physics and of life that made him great fun to work with.

For the spin resonance experiment I had the great pleasure of collaborating with Christian Barthel, whose forthright wit and example of shameless scavenging were frequent sources of relief and sustenance as we painfully tuned our way through a long sequence of not-quite-satisfactory devices. In the last few months I have enjoyed working with Teesa Christian. Leaving the fridge in her care, I felt like a parent using a babysitter for the first time. My fears for its safety proved unfounded; in fact, it is as though the babysitter has taken the baby off to college and then eloped with it. All I can do is express my hope that Teesa and the double-double experiment have a very happy future together.

Other lab members who particularly contributed to my happiness during my time here include Alex Johnson, from whom I learnt much about coding and skiing; Leo DiCarlo, who shared with Reilly a deep knowledge of electronics and a characteristic brand of Southern Hemisphere toilet humor; Jimmy Williams, my companion on many laps of Memorial Drive, who always managed to work hard while pretending to be unstressed; Ferdinand Kuemmeth, who saw through all my facile explanations; and Jim Medford, who quickly became a useful discussion partner on the spin qubit project. Many others generously taught me what they knew and kept the lab an entertaining place to be, including Jeff Miller, Ron Potok, Michael Biercuk, Nadya Mason, Douwe Monsma, Susan Watson, Nathaniel Craig, Josh Parks, Will Koehl, Floris Zwanenberg, Abram Falk, Sang Chu, Jerry Chow, Doug McClure, Slaven Garaj, Jacob Aptekar, Rob Barton, Hugh Churchill, Yongjie Hu, Maja Cassidy, Patrick Herring, Angela Kou, Bart Horn, Andrew Bestwick, Carolyn Stwertka,

Eli Levenson-Falk, Jennifer Harlow, Menyoung Lee, Alex Ogier, Michi Yamamoto, Reineer Heeres, David Marcos, Shu Nakaharai, Max Lemme, Sandro Erni, Morten Kjaergaard and more. From other groups, I benefited from discussions with Sandra Foletti, Hendrik Bluhm, Amir Yacoby, Mike Stopa, Jacob Krich and Mark Rudner among others.

No matter how hard I worked to make devices and apparatus, I could have accomplished nothing without the efforts of the CNS and DEAS technicians. I am grateful to Noah Clay, Steve Sheppard, Ed Macomber, Jiangdong Deng and especially Yuan Lu in the cleanroom, and to Louis Defeo and his colleagues in the machine shop. A succession of efficient administrators ensured all my orders got filled and helium was always on tap: James Reynolds, James Houlahan, James Gotfredson, Danielle Reuter, and Jess Martin.

Outside work, I would like to thank David for the propaganda that got me into this, and Tyler, Jack, Mary, and the Cambridge Running Club for helping me to get through it. I acknowledge those teachers from my distant pre-PhD life who encouraged and developed my interest in physics, especially Rodney Archard, Tchavdar Todorov, Tony Weidberg, Keith Burnett and Armin Reichold.

Lastly I thank my parents and family for their encouragement, help and love during my PhD and throughout my life.

# Chapter 1

## Introduction

Recent advances in nanoscale fabrication and measurement make it possible to study quantum behavior in individual electronic devices. Although quantum effects tend to become more important for smaller devices, demonstrating coherence in an individual quantum system remains difficult. This is because the system under study must satisfy two frequently conflicting requirements. To prevent decoherence, it must be well isolated from its uncontrolled environment; but for measurement, it must be coupled to a detection apparatus.

The payoffs from being able to control and measure individual quantum systems are threefold. Firstly, experiments beyond average measurements on ensembles become feasible, allowing fundamental studies of quantum mechanics [1, 2, 3]. Secondly, delicate quantum states are sensitive probes of their microscopic environment [4, 5]. Finally, information encoded in quantum bits ('qubits') can be efficiently manipulated using a quantum computer [6, 7].

This thesis focuses on controlling electron spins in GaAs quantum dots [8]. The electron spin is the simplest non-trivial quantum system, described by a two-dimensional Hilbert space. Since it couples only via its magnetic moment, it is often fairly well-isolated from its environment (better isolated, at least, than the electron charge.) Because the well-established techniques of spin resonance allow for any desired single-spin transformation,

the electron spin is a paradigmatic qubit [9].

## 1.1 Organization of this thesis

This thesis will present experiments on up to electron spins in systems of up to four coupled GaAs quantum dots. In the rest of this chapter, I will first explain briefly why a quantum computer is desirable and what the technical requirements are. I will then introduce the material system, quantum dots in GaAs heterostructures, and describe charge sensing, the measurement technique used throughout this thesis. Double quantum dots lead spin and charge to be coupled through the phenomenon of spin blockade, allowing quantum operations in the singlet-triplet basis of a pair of electrons. This chapter will conclude with a brief summary of new contributions reported in this thesis.

In the second chapter, I will describe a novel mechanism of electric dipole spin resonance mediated by an oscillating hyperfine coupling and driven by an electric field. Because time-varying electric fields are easy to generate and localize, this technique for spin manipulation can be technically easier than conventional magnetically driven spin resonance. Chapter 3 studies the dephasing of a pair of spins in a double quantum dot under the combined effects of exchange and hyperfine interactions. Chapter 4 develops techniques to manipulate and read out spin in a triple quantum dot, with the aim of realizing an exchange-only qubit. Chapter 5 describes progress towards a two-spin-qubit gate in the singlet-triplet basis, using four electrons in a pair of double dots.

Three appendices give technical information relating to the experiments. Appendix A details my fabrication recipe. Appendix B describes the construction of a radio-frequency reflectometry apparatus and gives a brief description of tuning. Appendix C explains how to synchronize two Tektronix arbitrary waveform generators precisely.

## 1.2 Quantum computing

The process of computation involves encoding information in physical objects ('bits') and manipulating those objects until they encode the desired solution to some problem. Present-day classical computers restrict themselves to a subset of the manipulations allowed by the laws of physics, namely those that map eigenstates of the measurement operator into each other. A quantum computer does not obey this restriction and can carry out the general unitary transformations allowed by quantum mechanics [6, 7].

Several problems are known for which a quantum computer is dramatically more efficient than a quantum computer. The two most famous quantum algorithms are Shor's algorithm and Grover's algorithm. Shor's algorithm factorizes  $n$ -digit numbers in a time that scales as  $n^2$ , rather than  $e^{n^{1/3}}$  classically [10], and Grover's algorithm finds unique solutions to mathematical functions of  $n$  bits in a time that scales as  $2^{n/2}$  rather than  $2^n$  [11].

Actually making a quantum computer, a machine that can carry out arbitrary unitary transformations on non-trivial inputs, seems at first sight impossible with any foreseeable technology. Several theorems make it seem slightly less impossible. First, any unitary transformation on a collection of quantum bits ('qubits') can be decomposed into a series of one- and two-qubit unitary transformations [12]. In fact, any one of a large class of two-bit transformations is sufficient; this class includes the so-called controlled-phase (CPHASE) and square-root-of-swap ( $\sqrt{\text{SWAP}}$ ) gates [13]. Secondly, it is not even necessary to perform arbitrary one-qubit transformations; a discrete subset of transformations suffices for efficient approximation [14, 6]. Finally, even imperfectly realized quantum gates can be corrected at the price of a tolerable increase in computational complexity [15].

Any physical realization of a quantum computer must satisfy extremely demanding requirements, but electron spins in semiconductor quantum dots may be suited to act as

a basis [16, 9]. Since the spin projection can take on two values, it naturally forms a well-defined quantum bit, or qubit, comparatively insensitive to decoherence. At attainable temperatures, thermal relaxation can be used to prepare spins in a known-state. Arbitrary single-qubit gates are possible by electron spin resonance [17], and the universal  $\sqrt{\text{SWAP}}$  gate can be carried out via Heisenberg exchange between two spins. And spin-selective electron tunnel rates allow for qubit readout [18]. Whether these elements can ever be combined to make a practical computer is not known. Experiments on manipulating and measuring single spins, including those reported here, are partly motivated by a desire to answer this question.

### 1.3 GaAs heterostructures, quantum dots and charge sensing

The attraction GaAs/AlGaAs heterostructures as a substrate for quantum dots is the unrivaled tunability of the confinement potential. Individual parameters of the Hamiltonian – electric and magnetic fields, energy levels and tunnel couplings – can be varied rapidly in a single device. Electron spin states can be mapped to charge states and read out electronically [18, 19]. Finally, well-established lithographic techniques can be applied, permitting in principle devices of almost arbitrary size and complexity.

Fabrication of a quantum dot device begins with a heterostructure grown by molecular beam epitaxy [22]. A layer of dopant atoms (usually Si substituting Ga) donates electrons to a quantum well formed at the heterointerface, creating a two-dimensional electron gas (2DEG) located  $\sim 100$  nm below the surface (Fig. 1.1(a)). Electrical contact to the 2DEG is achieved through PtAuGe contact pads deposited on the surface of the wafer and annealed to diffuse AuGe down to the 2DEG. To create nanostructures, TiAu topgates are patterned using electron beam lithography. Voltages of order  $\sim -300$  mV locally deplete

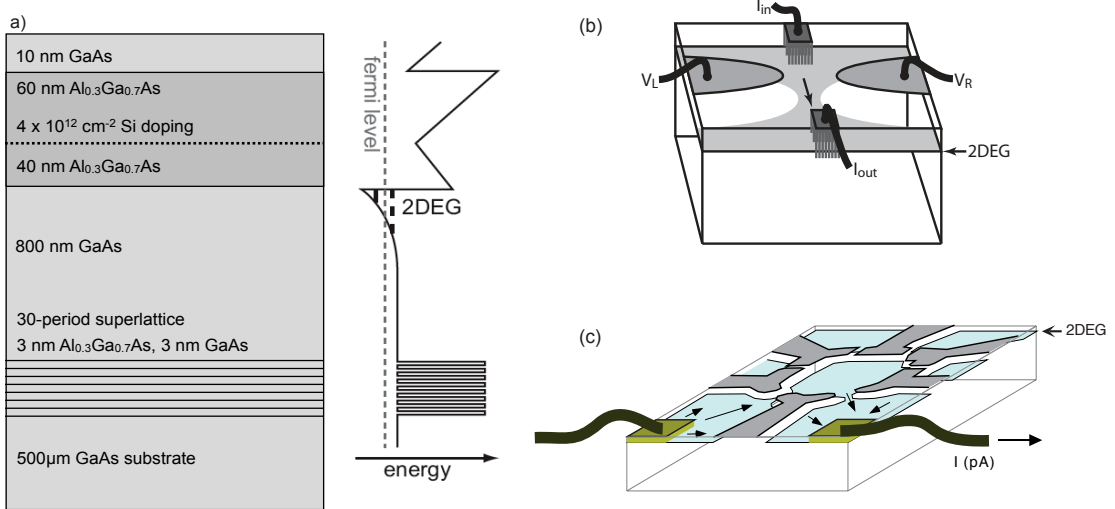


Figure 1.1: Heterostructures and quantum dots. (a) Schematic of GaAs/AlGaAs heterostructure and potential profile of the conduction band, showing formation of the 2DEG at the interface. The specific parameters shown here are those of the wafers 031104B and 050329A grown by the Gossard group at Santa Barbara and used in the experiments described in this thesis. (b) In a quantum point contact device, topgate voltages deplete the 2DEG, creating a one-dimensional channel for electrical transport [20]. (c) A ring of topgates creates a quantum dot [21].

the 2DEG, forming two kinds of structure important for this thesis: quantum point contacts (QPCs) and quantum dots [23, 24]. A QPC is formed when two topgates define a narrow channel through which electrical current can flow 1.1. Changes in the electrical potential in the channel, caused by varying the topgate voltage or by the motion of nearby charges, lead to changes in the electrical resistance of the current path. A quantum dot is formed in a potential minimum defined by a ring of topgates. The topgate voltages control the size, shape and depth of the minimum, and hence the equilibrium electron occupation of the quantum dot. The potential barrier(s) between the dot and the rest of the 2DEG, which control the electron tunnel rate to and from the leads, are also tunable. Measurements are typically performed in a dilution refrigerator at an electron temperature  $\sim 150$  mK.

As well as high mobility, a heterostructure for well-tuned quantum dots must have two other properties. Good control over the potential at the 2DEG requires that the

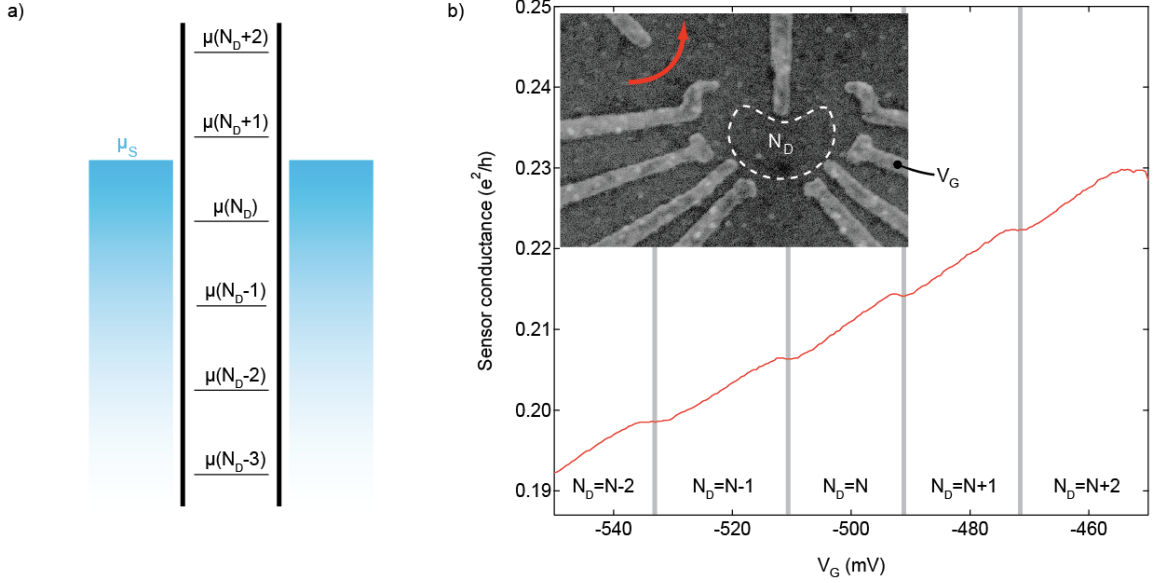


Figure 1.2: (a) The chemical potential  $\mu(N)$  of a quantum dot for various electron occupancies  $N$ . The dot will be filled up to the chemical potential of the leads  $\mu_s$ . Reducing a gate voltage raises the chemical potential in the dot, decreasing the electron number. (b) Conductance of a charge sensing point contact as a gate voltage  $V_G$  is swept. Steps correspond to changes in the dot occupancy  $N_D$ , marked along the bottom axis. The overall background slope reflects the direct electrostatic coupling of  $V_G$  to the point contact. Inset: The device, with locations of dot and charge sensor indicated.

heterointerface be located close to the surface, and a stable device potential implies that charges do not switch between donors in the dopant layer [25]. The heterostructures used in this thesis, although exceptionally stable, do not have especially good properties in the other respects; this makes device tunability a serious difficulty and the most time-consuming obstacle overcome in the experiments described here.

Although the gate voltages that control the charge on the dot vary continuously, the charge itself is quantized when the potential barrier to the leads is made large enough. The number of electrons  $N_D$  on the dot is determined by background charges, gate voltages and the electrochemical potentials  $\mu_S$  and  $\mu_D$  of the leads. With no bias applied across the dot, so that  $\mu_S = \mu_D$ ,  $N_D$  satisfies:

$$\mu(N_D) < \mu_s < \mu(N_D + 1) \quad (1.1)$$

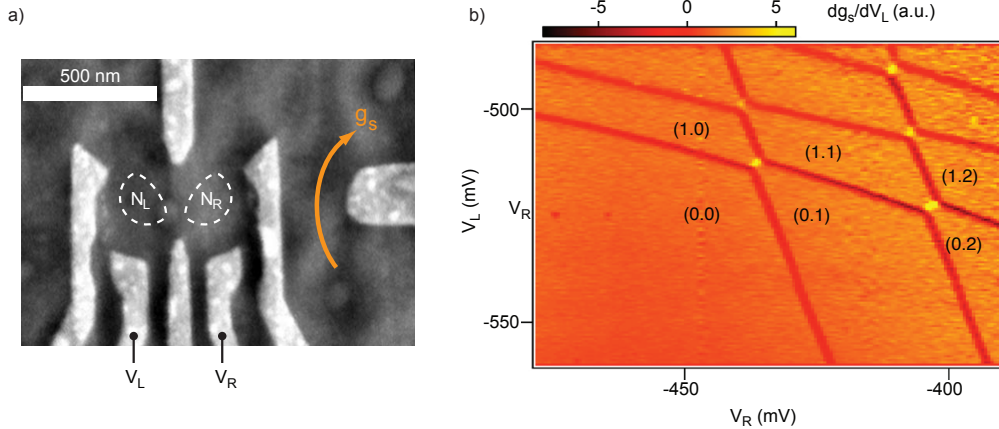


Figure 1.3: (a) A few-electron double quantum dot device with a charge sensor of conductance  $g_s$ . (b) Charge stability diagram of the device, measured using the charge sensor as a function of  $V_L$  and  $V_R$  [28]. Transition lines running approximately vertical (horizontal) separate regions of separate right (left) dot occupancy. Capacitive coupling between dots leads to anticrossings that show up as bright diagonal lines. The equilibrium electron occupancy for each gate configuration is indicated.

where  $\mu(N)$  is the chemical potential of a dot containing  $N$  electrons.

Sweeping the voltage  $V_G$  on a gate with capacitance  $C_G$  to the dot changes the chemical potential and therefore  $N_D$ . It is usually valid to separate the energy of a single dot into a charging term, parameterized by a constant total dot capacitance  $C$ , and a much smaller confinement term. In this approximation, changing  $V_G$  by

$$\Delta V_G = e/C_G \quad (1.2)$$

changes  $N_D$  by one [26].

The occupation can be measured using a nearby charge sensor QPC, as shown in Fig. 1.2(b) [27]. As gate voltage  $V_G$  is swept, the sensor conductance  $g_s$  has a step every time  $N_D$  changes. The regularity of the steps in Fig. 1.2(b) validates the approximations in the previous paragraph.

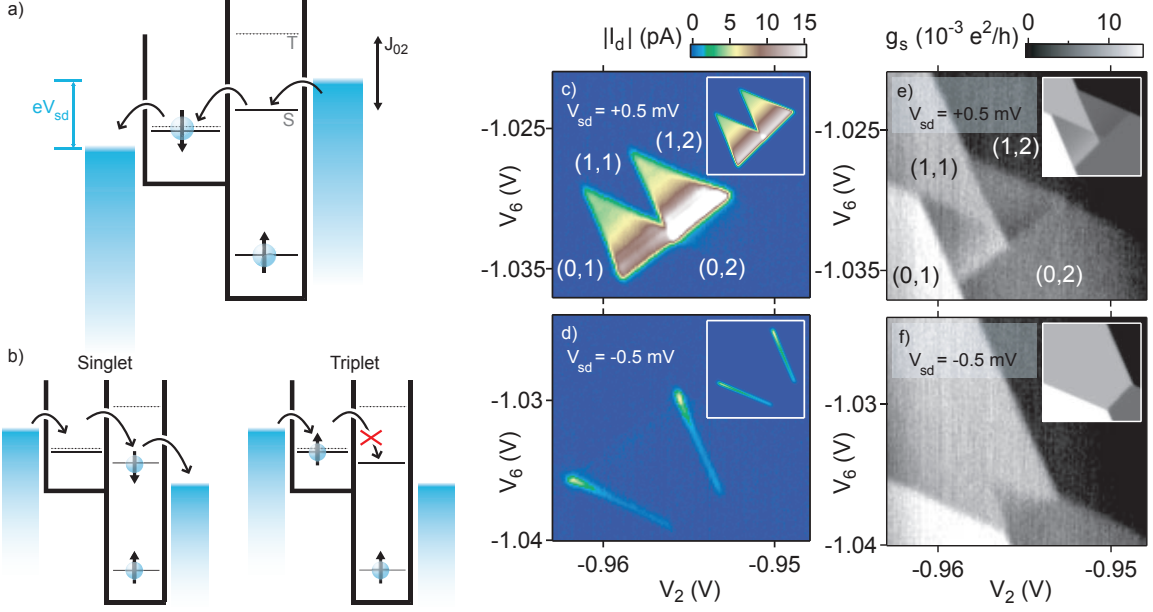


Figure 1.4: Spin blockade in a double quantum dot. (a) Chemical potential of dots and leads under positive bias  $V_{sd}$ . The triplet state of the right dot is higher in energy by the exchange  $J_{02}$ , but this does not prevent electron transport through the device. (b) Under negative bias, exchange makes electron tunneling spin-selective, suppressing transport. (c) and (d) Current  $I_d$  through the device for positive and negative bias, showing strong asymmetry. (e) and (f) Charge sensing signal, also showing asymmetry [31].

## 1.4 Double quantum dots and spin blockade

A richer and more tunable spectrum of electron states can be achieved in double quantum dots (Fig. 1.3(a)) [29]. To some extent, the properties of each dot can be tuned separately. The occupations ( $N_L, N_R$ ) of left and right dots respectively are controlled mainly by the gate voltages  $V_L$  and  $V_R$ , resulting in the charge stability diagram shown in Fig. 1.3(b) [30, 28]. Small enough devices can be completely emptied, allowing precise control of the number of electrons in each dot.

One of the most important features of double dots from the point of view of spin physics is that the exchange between two electrons occupying the device can be tuned over a very wide range. The exchange, defined as the energy difference between the lowest  $m_s = 0$  spin-triplet and spin-singlet levels, arises because Pauli exclusion requires overall antisymmetry

of the wavefunction under electron interchange. The ground state, with symmetric spatial wavefunction at zero magnetic field, must therefore be spin-antisymmetric, i. e. a singlet [32].

The magnitude of the exchange depends on the degree to which the two spatial wavefunctions overlap. When the electrons occupy separate dots, the exchange can be arbitrarily small, but for electrons occupying the same dot, the exchange is as large as several hundred microelectron volts, leading to a strong coupling of spin and charge degrees of freedom.

The most dramatic manifestation of this coupling is an asymmetry of electron tunneling through the double dot, known as spin blockade [33, 31]. Spin blockade can be observed when the device is configured close to the degeneracy of (1,1) and (0,2) occupations. An electrical bias applied across the device introduces a chemical potential difference between left and right leads, driving electrons to tunnel through the device by occupying states of successively lower chemical potential. Under positive bias, the dots' chemical potentials can be tuned as shown in Fig. 1.4(a) and an electrical current flows (Fig. 1.4(c)). However, under negative bias, if the electron loaded from the left forms a triplet state with the electron already present on the right, it cannot escape to either side (Fig. 1.4(b)). Transport stops until one of the spins is flipped or exchanged via higher-order tunneling with the leads, so that the average current  $I_d$  through the double dot is strongly suppressed (Fig. 1.4(d)).

The same asymmetry is also evident in charge sensing [31]. For the configuration of Fig. 1.4(a), the device shuttles rapidly between the charge states (0,2), (1,1) and (0,1), spending approximately equal time in each. The time-averaged sensor conductance will therefore be an average of the values corresponding to these three charge states, as seen in the lower triangle of (Fig. 1.4(e)). (In the upper triangle, the chemical potentials are such that transport occurs via the sequence of charge transitions  $(0, 2) \rightarrow (1, 1) \rightarrow (1, 2) \rightarrow (0, 2)$ ,

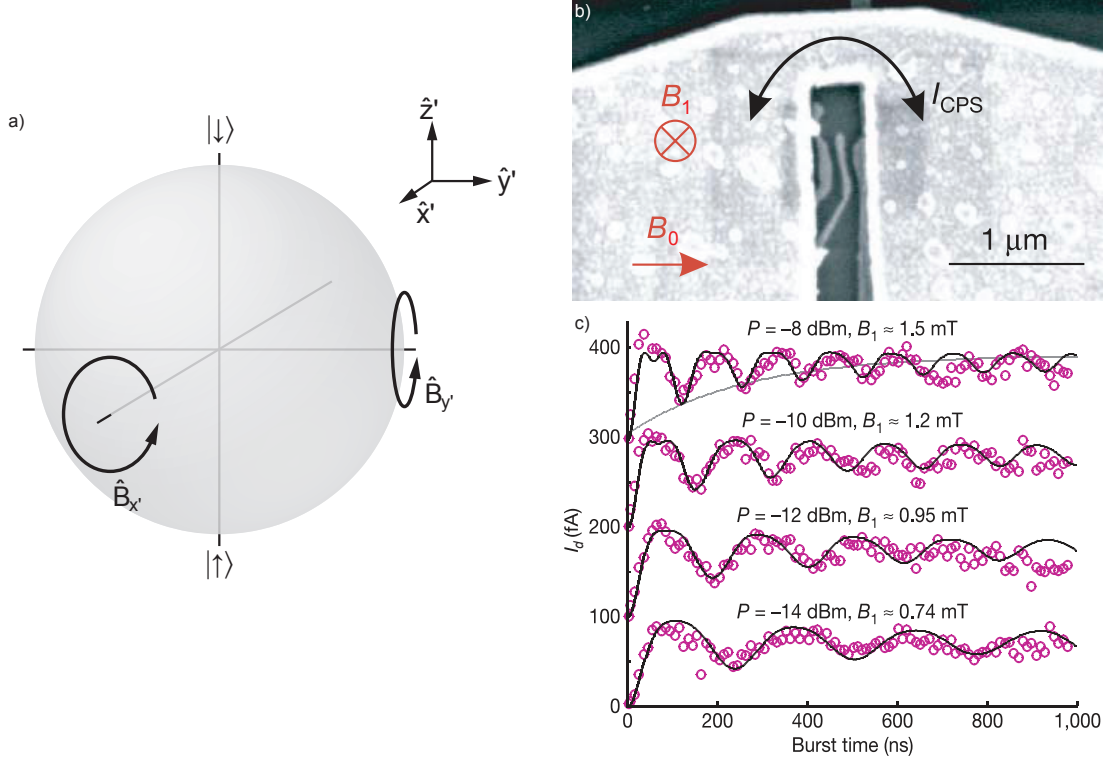


Figure 1.5: (a) Bloch sphere of a single spin in the rotating frame. ESR bursts drive rotations about two independent axes, allowing arbitrary spin rotations. (b) A device used to demonstrate ESR in a single-spin quantum dot [17]. The ESR field  $\mathbf{B}_1$  is driven with a microwave current  $I_{CPS}$  through a stripline. (c) Coherent oscillations of the electron spin state, detected via the spin-blocked current  $I_d$  [17].

and the average sensor conductance is again an average of values corresponding to these states.) However, for the spin-blocked configuration, the (1,1) charge configuration dominates, as seen in Fig. 1.4(f).

## 1.5 Electron spin resonance

To see how electron spin resonance allows arbitrary single-qubit operations, consider the evolution of an electron spin under the influence of a static field  $\mathbf{B}_0$  defining the  $z$ -axis, and an oscillating field  $2\mathbf{B}_1$  along the  $x$ -axis [34]. Schrödinger's equation is:

$$i\hbar \frac{d|\psi\rangle}{dt} = -g\mu_B(B_0S_z + 2B_1S_x \cos(\omega t + \phi))|\psi\rangle, \quad (1.3)$$

where  $|\psi\rangle$  is the spin wavefunction,  $g$  the electron  $g$ -factor,  $\mu_B$  the Bohr magneton,  $\mathbf{S} = (S_x, S_y, S_z)$  the electron spin, and  $\phi$  the phase of the oscillating field. This equation has a simpler form in a frame rotating about the  $z$  axis at frequency  $\omega$ . To transform to this frame, we make the substitutions:

$$\mathbf{S} = e^{i\omega t S_z} \mathbf{S}' e^{-i\omega t S_z} \quad (1.4)$$

$$|\psi\rangle = e^{-i\omega t S_z} |\psi'\rangle. \quad (1.5)$$

The Schrödinger equation becomes:

$$i\hbar \frac{d|\psi'\rangle}{dt} = \hbar [(\omega - \omega_L) S_{z'} + \Omega (S_{x'} \cos \phi + S_{y'} \sin \phi)] + \text{terms oscillating with frequency } 2\omega \quad (1.6)$$

where

$$\omega_L \equiv g\mu_B B_0/\hbar \quad (1.7)$$

$$\Omega \equiv g\mu_B B_1/2\hbar \quad (1.8)$$

are the Larmor and Rabi frequencies. Under the approximation (almost always justified)  $\Omega \ll \omega$ , the effect of the oscillating terms averages away, and so in the rotating frame the spin evolves as though under the influence of a static magnetic field

$$\mathbf{B}' = \frac{\hbar}{g\mu_B} \begin{pmatrix} \Omega \cos \phi \\ \Omega \sin \phi \\ \omega - \omega_L \end{pmatrix}. \quad (1.9)$$

Usually the oscillating magnetic field is applied with angular frequency  $\omega = \omega_L$ , so that by applying ESR bursts with appropriate phase, the electron spin can be rotated around any axis in the  $(x', y')$  plane (Fig. 1.5). By combining up to three rotations around  $x'$  and  $y'$  axes, arbitrary rotations on the Bloch sphere can be performed, and therefore arbitrary unitary transformations of the spin [35].

ESR was first demonstrated in a quantum dot in Ref. [17]. To create large enough oscillating magnetic fields, a microwave stripline was deposited over the double-dot device (Fig. 1.5(b)). Coherent spin rotations were detected via the breaking of spin blockade when microwaves were applied (Fig. 1.5)(c).

There are several technological reasons why one may wish to avoid using magnetically driven ESR as a means of spin manipulation. Generation of local time-varying fields implies on-chip ohmic heating, whereas quantum dot operation requires dilution refrigerator temperatures. Since the power density needed to generate a given  $B_1$  scales with the inverse square of the device dimension, this limitation becomes more severe for nanoscale devices. (Using superconducting striplines is of limited help, as the current density used in Ref. [17] approaches the critical current of Nb [36]) Apart from ohmic heating, the stripline design shown in Fig. 1.5(b) would also disturb nearby devices or a charge sensor.

One could hope to circumvent these difficulties by applying a global  $\mathbf{B}_1$  [37]. However, this creates electric fields and eddy current heating throughout the chip, as well as posing the problem of how to address individual spins. These difficulties provide motivation for seeking to manipulate spins electrically.

## 1.6 The singlet-triplet basis

In the singlet-triplet basis, two electron spins are used to encode each qubit [38, 39]. In return, all logic operations become possible by using gate voltage pulses rather than time-varying magnetic fields.

The two states of the qubit are represented by the singlet  $S$  and  $m_s = 0$  triplet  $T$  states of a double quantum dot in the  $(1, 1)$  charge configuration. The corresponding Bloch sphere is shown in Fig. 1.6. Single-qubit manipulations are carried out by making use of

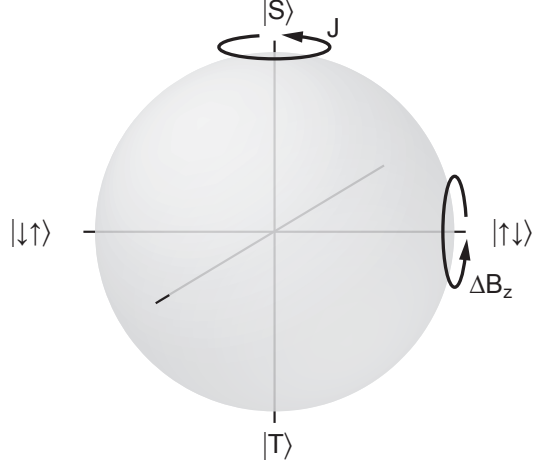


Figure 1.6: Bloch sphere in the singlet-triplet basis. The two logic states are represented by the singlet  $S$  and  $m_s = 0$  triplet  $T$  states of the  $(1, 1)$  charge configuration. The two hyperfine-split states  $|\uparrow\downarrow\rangle$  and  $|\downarrow\uparrow\rangle$  are represented by points on the equator of the sphere. Single-qubit rotations are accomplished via rotations about two independent axes driven by exchange  $J$  and a magnetic field or hyperfine difference between dots  $\Delta B_z$ .

two interactions, whose combination allows for any unitary transformation in this basis: Exchange  $J$ , which drives rotations about the  $z$ -axis, and a magnetic field difference  $\Delta B_z$  between the dots, which drives rotations about the  $x$ -axis.

The qubit can be initialized and read out as follows [40, 39]. The device is configured in  $(0, 2)$ , where tunneling to the leads causes rapid relaxation to the singlet state. Rapidly pulsing the gate voltages (in  $\sim 1$  ns) to configure the device in  $(1, 1)$  preserves the electron spin, preparing the state  $S$ . To read out the qubit, this sequence is reversed. For state  $S$ , the two electrons can recombine as a singlet in  $(0, 2)$ ; however, for state  $T$ , the electrons remain on separate dots. This difference in the charge state, detected with a charge sensor, allows electrical readout of the qubit.

All the elements for single-qubit operation have now been realized, although not in the same device. Tuning the wavefunction overlap between electrons using gate voltages allows rapid control of the exchange interaction, demonstrated by coherent qubit rotations [40]. Controlled rotations about an orthogonal axis can be achieved by establishing an energy

difference between  $|\uparrow\downarrow\rangle$  and  $|\downarrow\uparrow\rangle$  states using a controlled hyperfine interaction [41]. Optimized charge sensing permits single-shot qubit readout [19]. And coherence times over  $1\ \mu\text{s}$  can be achieved using a spin echo sequence to suppress hyperfine dephasing [40].

## 1.7 Summary of contributions

The key contributions reported here are as follows:

- In Chapter 2, electrically driven spin resonance of a single electron is demonstrated. By studying the magnetic field dependence of the resonance strength, it is shown that a novel mechanism couples the electric field to the electron spin, namely a fluctuating hyperfine field. Driving the resonance is found to create a nuclear polarization in the quantum dot. Using a micromagnet to create a magnetic field gradient across the device, a technique to address individual spins in a multi-electron device is presented.
- In Chapter 3, the exchange between a pair of electrons in a double quantum dot is carefully adjusted and measured, and its effect on spin dephasing is studied. An exchange comparable to or stronger than the hyperfine coupling was found to lead to a saturation of dephasing, in agreement with a prediction from quasistatic theory. The spin dephasing was also measured as a function of time, and oscillations of the spin-flip probability were observed, again in agreement with theory.
- In Chapter 4, a triple quantum dot device incorporating two point contact charge sensors was fabricated. The technique of multiplexed reflectometry, not previously applied to point contacts, was used to monitor both charge sensors at MHz frequencies. The device was tuned to a charge configuration where it could be operated as a qubit, and preparation, readout, and coherent control of the electron spins was demonstrated.

- In Chapter 5, a prototype two-qubit device was fabricated and measured. Although spin-qubit operation proved impossible in this device, the coupling strength was measured for the first time in the qubit charge configuration and found to be in principle sufficient for two-qubit gates.

## Chapter 2

# Gate-driven hyperfine-mediated electron spin resonance

E. A. Laird, C. Barthel, E. I. Rashba, C. M. Marcus

*Department of Physics, Harvard University, Cambridge, Massachusetts 02138*

M. P. Hanson, A. C. Gossard

*Department of Materials, University of California, Santa Barbara, California 93106*

A recently discovered mechanism of electric dipole spin resonance, mediated by the hyperfine interaction, is investigated experimentally and theoretically. The effect is studied using a spin-selective transition in a GaAs double quantum dot. The resonant frequency is sensitive to the instantaneous hyperfine effective field, revealing a nuclear polarization created by driving the resonance. A device incorporating a micromagnet exhibits a magnetic field difference between dots, allowing electrons in either dot to be addressed selectively. An unexplained additional signal at half the resonant frequency is presented.<sup>2</sup>

---

<sup>2</sup>This chapter is adapted from Refs. [42, 43] with permission, © (2007) by the American Physical Society].

## 2.1 Introduction

Electric dipole spin resonance (EDSR) is a method to electrically manipulate electron spins.

In this technique, two fields are applied; a static magnetic field  $\mathbf{B}$  and an oscillating electric field  $\tilde{\mathbf{E}}(t)$  resonant with the electron precession (Larmor) frequency [44, 45, 46, 47]. Spin resonance techniques are of interest for quantum computing schemes based on single electron spins, because they allow arbitrary one-qubit operations [9]. Single-spin EDSR is a particularly desirable experimental tool because it allows spin manipulation without time-dependent magnetic fields, which are difficult to generate and localize at the nanoscale [48, 49, 50, 17].

Achieving EDSR requires a mechanism to couple  $\tilde{\mathbf{E}}$  to the electron spin  $\sigma$ . This coupling can be achieved by the traditional spin-orbit interaction, which couples  $\sigma$  to the electron momentum  $\mathbf{k}$ , or by an inhomogeneous Zeeman interaction, which couples  $\sigma$  to the electron coordinate  $\mathbf{r}$  [51, 47, 52, 53, 54]. Single-spin EDSR has recently been achieved in quantum dots using both techniques [55, 56].

Recently, we presented an experimental and theoretical study of a novel EDSR effect mediated by the spatial inhomogeneity of the hyperfine nuclear field [42]. An electron moving under the influence of the electric field  $\tilde{\mathbf{E}}(t)$  experiences this inhomogeneity as an oscillating hyperfine coupling which drives spin transitions. In this paper, we illuminate the underlying physics and present new experimental data on a still unexplained phenomenon at half the resonant frequency.

This EDSR effect is observed via spin-blocked transitions in a few-electron GaAs double quantum dot [57]. As expected for a hyperfine mechanism, but in contrast to  $\mathbf{k}-\sigma$ -coupling mediated EDSR, the resonance strength is independent of  $\mathbf{B}$  at low field and shows, when averaged over nuclear configurations, no Rabi oscillations as a function of time. We find

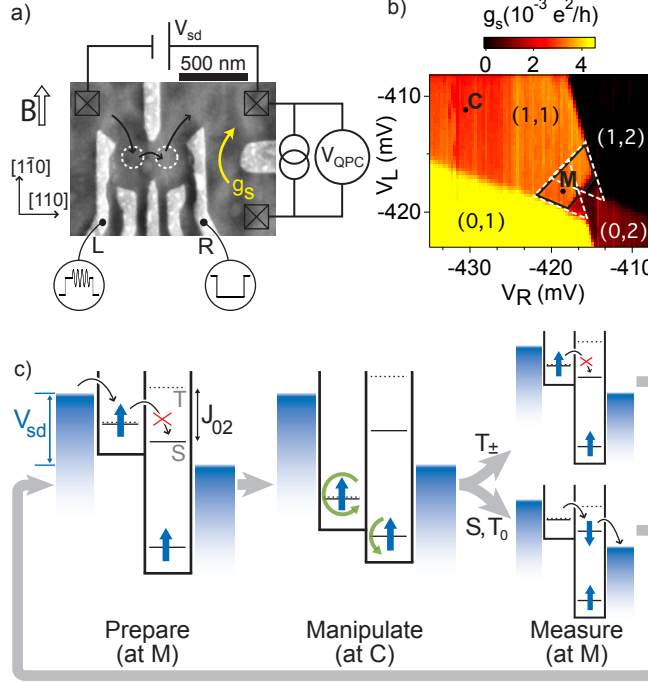


Figure 2.1: (a) Micrograph of a device lithographically identical to the one measured, with schematic of the measurement circuit. Quantum dot locations are shown by dashed circles, and a bias  $V_{sd}$  drives sequential tunneling in the direction marked by black arrows. The conductance  $g_s$  of the QPC on the right is sensitive to the dot occupation. The direction of the magnetic field  $\mathbf{B}$  and the crystal axes are indicated. (b) QPC conductance  $g_s$  measured at  $V_{sd} \sim 600 \mu\text{eV}$  near the (1,1)-(0,2) transition. Equilibrium occupations for different gate voltages are shown, as are gate voltage configurations during the measurement/reinitialization (M) and manipulation (C) pulses. The two white dashed triangles outline regions where transport is not Coulomb blocked; the solid black line outlines where spin blockade is active. A plane background has been subtracted. (c) Energy levels of the double dot during the pulse cycle (See text).

that at large  $\mathbf{B}$  driving the resonance creates a nuclear polarization, which we interpret as the backaction of EDSR on the nuclei [58, 59, 17, 60, 61]. Finally, we demonstrate that spins can be individually addressed in each dot by creating a local field gradient.

## 2.2 Device and measurement

The device for which most data is presented (Figure 1(a)) was fabricated on a GaAs/Al<sub>0.3</sub>Ga<sub>0.7</sub>As heterostructure with two-dimensional electron gas (2DEG) of density  $2 \times 10^{15} \text{ m}^{-2}$  and mo-

bility  $20 \text{ m}^2/\text{Vs}$  located 110 nm below the surface. Voltages applied to Ti/Au top gates locally deplete the 2DEG, defining a few-electron double quantum dot. A nearby charge sensing quantum point contact (QPC) is sensitive to the electron occupation ( $N_L, N_R$ ) of the left ( $N_L$ ) and right ( $N_R$ ) dots [27, 30]. The voltages  $V_L$  and  $V_R$  on gates L and R can be rapidly pulsed; in addition, L is coupled to a microwave source. The static magnetic field  $\mathbf{B}$  was applied in the plane of the heterostructure, and measurements were performed in a dilution refrigerator at 150 mK electron temperature.

The characteristic feature of tunnel-coupled quantum dots is a discrete electron energy spectrum. An overall shift to the spectrum, proportional to the electron occupation, is induced by  $V_L$  and  $V_R$ , which therefore determine which occupation is energetically favoured. Figure 1(b) shows the QPC conductance  $g_s$  as a function of  $V_L$  and  $V_R$ ; different conductances correspond to different  $(N_L, N_R)$ . For most  $V_L, V_R$  configurations, only one value of  $(N_L, N_R)$  is energetically accessible; these correspond in Figure 1(b) to regions of uniform  $g_s$ .

A bias  $V_{sd}$  applied across the device drives electron transport via sequential tunneling subject to two constraints [8]. The first constraint, Coulomb blockade, arises because for most gate configurations electrostatic repulsion prevents additional electrons from tunneling onto either dot. This constraint inhibits transport except when  $V_L, V_R$  are tuned so that three occupation configurations are near-degenerate. The energy cost of an extra electron tunneling through the device is then small enough to be provided by the bias voltage. Values of  $V_L$  and  $V_R$  satisfying this condition correspond to the two white dashed triangular regions marked in Figure 1(b), for which transport is permitted via the transition sequences  $(0, 2) \rightarrow (0, 1) \rightarrow (1, 1) \rightarrow (0, 2)$  or  $(0, 2) \rightarrow (1, 2) \rightarrow (1, 1) \rightarrow (0, 2)$ .

A second constraint, spin blockade, is caused by the Pauli exclusion principle, which

leads to an intra-dot exchange energy  $J_{02}$  in the right dot [33, 31]. As shown in the first panel of Figure 1(c), the effect of this exchange is to make the  $(1, 1) \rightarrow (0, 2)$  transition selective in the two-electron spin state, inhibited for triplet states but allowed for the singlet. The hyperfine field difference between dots converts the  $m_s = 0$  component  $T_0$  of the blocked triplet  $T$  to an unblocked singlet  $S$  within  $\sim 10$  ns, as we have confirmed by the technique of [40]. However, decay of  $m_s = \pm 1$  components  $T_{\pm}$  requires a spin flip and therefore proceeds much more slowly. This spin flip becomes the rate-limiting step in transport, and so the time-averaged occupation is dominated by the  $(1,1)$  portion of the transport sequence [31]. Gate configurations where spin blockade applies correspond to the black solid outlined region of Figure 1(b); inside this region,  $g_s$  has the value corresponding to  $(1,1)$ . Any process that induces spin flips will partially break spin blockade and lead to a decrease in  $g_s$ .

Unless stated otherwise, EDSR is detected via changes in  $g_s$  while the following cycle of voltage pulses  $V_L$  and  $V_R$  [17] is applied to L and R (Figure 1(c)). The cycle begins inside the spin blockade region (M in Figure 1(b)), so that the two-electron state is initialized to  $(1,1)T_{\pm}$  with high probability. A  $\sim 1 \mu\text{s}$  pulse to point C prevents electron tunneling regardless of spin state. Towards the end of this pulse, a microwave burst of duration  $\tau_{\text{EDSR}}$  at frequency  $f$  is applied to gate L. Finally the system is brought back to M for  $\sim 3 \mu\text{s}$  for readout/reinitialization. If and only if a spin (on either dot) was flipped during the pulse, the transition  $(1,1) \rightarrow (0,2)$  occurs, leading to a change in average occupation and in  $g_s$ . If this transition occurs, subsequent electron transitions reinitialize the state to  $(1,1)T_{\pm}$  by the end of this step, after which the pulse cycle is repeated. This pulsed EDSR scheme has the advantage of separating spin manipulation from readout.

Changes in  $g_s$  are monitored via the voltage  $V_{\text{QPC}}$  across the QPC sensor biased at 5 nA. For increased sensitivity, the microwaves are chopped at 227 Hz and the change in

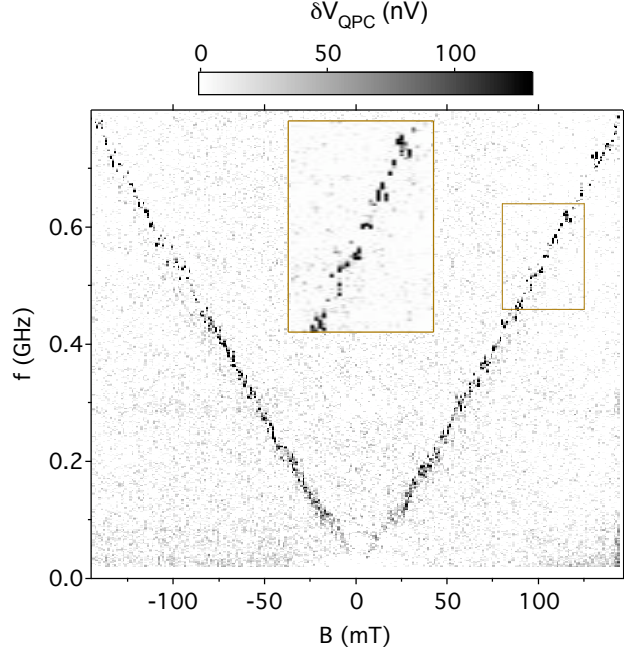


Figure 2.2: Signal of spin resonance  $\delta V_{\text{QPC}}$  as a function of magnetic field  $B$  and microwave frequency  $f$ . EDSR induces a breaking of spin blockade, which appears as a peak in the voltage across the charge sensor  $\delta V_{\text{QPC}}$  at the Larmor frequency. Field- and frequency-independent backgrounds have been subtracted. Inset: Jitter of resonant frequency due to random Overhauser shifts.

voltage  $\delta V_{\text{QPC}}$  is synchronously detected using a lock-in amplifier. We interpret  $\delta V_{\text{QPC}}$  as proportional to the spin-flip probability during a microwave burst, averaged over the 100 ms lock-in time constant.

### 2.3 EDSR spectroscopy

Resonant response is seen clearly as  $B$  and  $f$  are varied for constant  $\tau_{\text{EDSR}} = 1 \mu\text{s}$  (Figure 2.) A peak in  $\delta V_{\text{QPC}}$ , corresponding to a spin transition, is seen at a frequency proportional to  $B$ . This is the key signature of spin resonance. (A feature corresponding to lifted spin blockade around  $B=0$  is not seen or expected, because this measurement technique is sensitive only to the differential effect of the microwaves [17].) From the slope of the resonant line in Figure 2 a  $g$ -factor  $|g| = 0.39 \pm 0.01$  is found, typical of similar GaAs

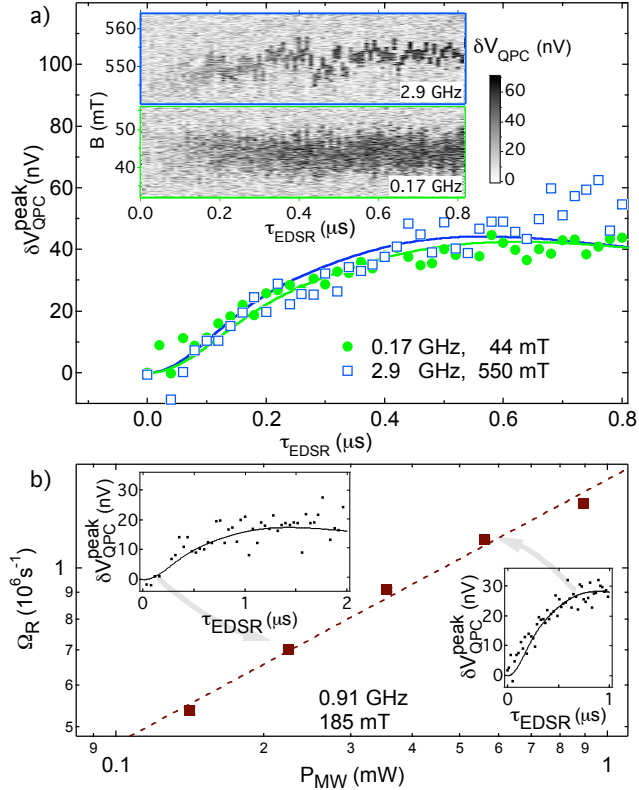


Figure 2.3: (a) Measured EDSR peak strength  $\delta V_{QPC}^{\text{peak}}$  (symbols) versus microwave pulse duration  $\tau_{EDSR}$  for two frequencies, along with theoretical fits (curves) obtained by numerically evaluating and scaling Equation (4) (see text). Both the applied power ( $P_{MW} \sim 0.6$  mW) and the calibrated power at the device are equal at these two frequencies (see footnote to Section 4.1). Inset: Raw data from which the points in the main figure are extracted. Each vertical cut corresponds to one point in the main figure. Jitter in the field position of the resonance reflects time-dependent Overhauser shifts. (b) Spin-flip rate  $\Omega_R$  as a function of applied microwave power  $P_{MW}$ , along with a fit to the form  $\Omega_R \propto \sqrt{P_{MW}}$  (dashed line). Insets:  $\delta V_{QPC}^{\text{peak}}$  versus  $\tau_{EDSR}$  for two values of the microwave power, showing the fits from which points in the main figure are derived.

devices [62, 63]. We attribute fluctuations of the resonance frequency (Figure 2 inset) to Overhauser shift caused by the time-varying hyperfine field acting on the electron spin. Their range is  $\sim \pm 22$  MHz, corresponding to a field of  $\sim 4$  mT, consistent with Overhauser fields in similar devices [64, 65, 40].

Information about the EDSR mechanism can be obtained by studying the peak height as a function of duration, strength, and frequency of the microwave burst (Figure 3). To reduce the effects of the shifting Overhauser field, the microwave source is frequency modulated at

3 kHz in a sawtooth pattern with depth 36 MHz about a central frequency  $\bar{f}$ . The resonance line as a function of  $\tau_{\text{EDSR}}$  is shown in the inset of Figure 3(a). For equal microwave power at two different frequencies  $\bar{f}$ , the peak heights  $\delta V_{\text{QPC}}^{\text{peak}}$  are plotted in Figure 3(a) (main panel). The two data sets are similar in turn-on time and saturation value; this is the case for frequencies up to  $\bar{f} = 6$  GHz. From similar data (insets of Figure 3(b)), using theory to be described, we extract the dependence of the spin-flip rate  $\Omega_R$  on microwave power  $P_{\text{MW}}$  shown in the main panel of Figure 3(b). Coherent Rabi-type oscillations in  $\delta V_{\text{QPC}}^{\text{peak}}(\tau_{\text{EDSR}})$  are not observed for any microwave power or magnetic field over the range measured.

The  $B$ -independence of the EDSR strength rules out spin-orbit mediated EDSR of the  $\mathbf{k} - \boldsymbol{\sigma}$  type (either Dresselhaus or Rashba), for which the Rabi frequency is proportional to  $B$  [47, 54, 55]. This is in contrast to the results of [55], where the spin-orbit effect was found to dominate in a similar device to ours. A possible explanation is the device orientation relative to  $\mathbf{B}$  and the crystal axes. In both our experiment and [55], the gate geometry suggests a dominant  $\tilde{\mathbf{E}}(\mathbf{t})$  oriented along one of the diagonal axes ([110] or [1 $\bar{1}$ 0]), leading to an in-plane spin-orbit effective field  $\mathbf{B}_{\text{eff}}^{\text{SO}}$  perpendicular to  $\tilde{\mathbf{E}}(\mathbf{t})$ . In our geometry (see Figure 1(a)), this orientation of  $\mathbf{B}_{\text{eff}}^{\text{SO}}$  is parallel to  $\mathbf{B}$ , and therefore ineffective at driving spin transitions. In the geometry of [55],  $\mathbf{B}$  is perpendicular to  $\mathbf{B}_{\text{eff}}^{\text{SO}}$ , so that the  $\mathbf{k} - \boldsymbol{\sigma}$  spin-orbit mechanism becomes more efficient.

Although the strength of the EDSR line is field-independent, the hyperfine-induced jitter becomes more pronounced with increasing field. As seen from the upper inset to Figure 3(a), repeated scans over the resonance at high field display larger fluctuations in the position of the peak center. This difference presumably reflects slower nuclear spin diffusion [4] as well as incipient polarization (see Section 5). In none of the data was any periodicity of the jitter detectable [66].

## 2.4 Theory

A theoretical description of  $\delta V_{\text{QPC}}^{\text{peak}}(\tau_{\text{EDSR}})$  and its dependence on  $B$  and  $P_{\text{MW}}$  can be obtained by modeling EDSR as arising from the coupling of an electron in a single dot to an oscillating electric field  $\tilde{\mathbf{E}}(t)$  and the hyperfine field of an ensemble of nuclei <sup>3</sup> [68, 69]. Then the center of the dot oscillates as  $\mathbf{R}(t) = -e\tilde{\mathbf{E}}(t)/m\omega_0^2$ , where  $m$  is the electron effective mass, and  $\omega_0$  is its confinement frequency in a parabolic dot. As a result, the Hamiltonian of the hyperfine coupling of the electron spin  $\mathbf{S} = \boldsymbol{\sigma}/2$  with spatial coordinate  $\mathbf{r}$  to nuclear spins  $\mathbf{I}_j$  located at  $\mathbf{r}_j$  becomes time dependent,  $H_{\text{hf}} = A\sum_j \delta(\mathbf{r} + \mathbf{R}(t) - \mathbf{r}_j)(\mathbf{I}_j \cdot \mathbf{S})$ . Here  $A$  is the hyperfine coupling constant and the summation over  $j$  runs over all nuclear spins. After expanding  $H_{\text{hf}}$  in  $\mathbf{R}(t)$  (assumed small compared to the dot size) and averaging over the orbital ground-state wave function  $\psi_0(\mathbf{r})$  of the dot, the time dependent part of  $H_{\text{hf}}$  becomes  $H_{\text{hf}}(t) = \mathbf{J}(t) \cdot \boldsymbol{\sigma}$ , where  $\mathbf{J}(t)$  is an operator in all  $\mathbf{I}_j$ . Choosing the  $z$ -axis in spin space along  $\mathbf{B}$ , the components of  $\mathbf{J}(t)$  are  $J_z = \frac{1}{2}A\sum_j \psi_0^2(\mathbf{r}_j)I_j^z$  and

$$J_{\pm}(t) = \frac{eA}{m\omega_0^2} \sum_j \psi_0(\mathbf{r}_j) \tilde{\mathbf{E}}(t) \cdot \nabla \psi_0(\mathbf{r}_j) I_j^{\pm}. \quad (2.1)$$

The time-dependent off-diagonal components  $J_{\pm}(t)$  drive EDSR, while the quasi-static diagonal component  $J_z$  describes detuning of EDSR from the Larmor frequency  $\omega_L$  by an amount  $\omega_z$  randomly distributed as  $\rho(\omega_z) = \exp(-\omega_z^2/\Delta^2)/(\Delta\sqrt{\pi})$  [70]. The dispersions  $\Delta$  of the detuning and  $\Omega_R$  of the Rabi frequency are the root-mean-square values of  $J_z$  and  $J_{\pm}$  respectively. Whereas  $J_z$  is dominated by fluctuations of  $\mathbf{I}_j$  symmetric about the dot

---

<sup>3</sup>There exists some physical similarity between the hyperfine mechanism of EDSR described in this paper and EDSR due to the coupling of electron spin to a random exchange field in semimagnetic semiconductors [67].

centre,  $J_{\pm}$  is dominated by fluctuations antisymmetric in the  $\tilde{\mathbf{E}}$  direction because  $\tilde{\mathbf{E}} \cdot \nabla \psi_0(\mathbf{r})$  is odd with respect to the  $\tilde{\mathbf{E}}$  projection of  $\mathbf{r}$ . Finally,

$$\Delta = \frac{A}{2\hbar} \sqrt{\frac{I(I+1)m\omega_0 n_0}{2\pi\hbar d}}, \quad \Omega_R = \frac{e\tilde{E}A}{\hbar^2\omega_0} \sqrt{\frac{I(I+1)n_0}{8\pi d}}, \quad (2.2)$$

with  $I = 3/2$  for GaAs,  $n_0$  the nuclear concentration, and  $d$  the vertical confinement. It is seen that  $\Omega_R$  is independent of  $B$ ; this is in contrast to EDSR mediated by the conventional  $\mathbf{k} - \boldsymbol{\sigma}$  spin-orbit coupling, where Kramers' theorem requires that the Rabi frequency vanish linearly as  $B \rightarrow 0$  [47, 71, 54].

In an instantaneous nuclear spin configuration with detuning  $\delta\omega = 2\pi f - (\omega_L + \omega_z)$  and Rabi frequency  $\Omega$ , the spin-flip probability from an initial  $\uparrow$  spin state is [72]:

$$p_{\downarrow}(\tau_{\text{EDSR}}) = \frac{\Omega^2}{(\delta\omega/2)^2 + \Omega^2} \sin^2 \left[ \sqrt{(\delta\omega/2)^2 + \Omega^2} \tau_{\text{EDSR}} \right]. \quad (2.3)$$

(We neglect the electron spin relaxation and nuclear-spin dynamics, which remain slow compared with the Rabi frequency even in the EDSR regime [40, 69].) To compare with the time-averaged data of Figure 3, we average Equation (2.3) over  $\omega_z$  with weight  $\rho(\omega_z)$  and over  $\Omega$  with weight  $\rho(\Omega) = 2\Omega \exp(-\Omega^2/\Omega_R^2)/\Omega_R^2$ . This latter distribution arises because the  $J_{\pm}$  acquire Gaussian-distributed contributions from both  $I_j^x$  and  $I_j^y$  components of the nuclear spins, hence it is two-dimensional. Averaging over  $\omega_z$  and  $\Omega$  results in a mean-field theory of the hyperfine-mediated EDSR. The resulting spin-flip probability

$$\bar{p}_{\downarrow}(\tau_{\text{EDSR}}; \Delta, \Omega_R) = \int_{-\infty}^{+\infty} d\omega_z \rho(\omega_z) \int_0^{+\infty} d\Omega \rho(\Omega) p_{\downarrow}(\tau_{\text{EDSR}}) \quad (2.4)$$

shows only a remnant of Rabi oscillations as a weak overshoot at  $\tau_{\text{EDSR}} \sim \Omega_R^{-1}$ . The absence of Rabi oscillations is characteristic of hyperfine-driven EDSR when the measurement integration time exceeds the nuclear evolution time [4], and arises because  $J_{\pm}$  average to zero.

### 2.4.1 Comparison with data

To compare theory and experiment, the probability  $\bar{p}_\downarrow(\tau_{\text{EDSR}}; \Delta, \Omega_R)$  is scaled by a QPC sensitivity  $V_{\text{QPC}}^0$  to convert to a voltage  $\delta V_{\text{QPC}}^{\text{peak}}$ . After scaling, numerical evaluation of Equation (4) gives the theoretical curves shown in Figure 3(a). The parameters that determine these curves are as follows: The Larmor frequency spread,  $\Delta = 2\pi \times 28$  MHz, is taken as the quadrature sum of the jitter amplitude seen in Figure 2 and half the frequency modulation depth, whereas  $\Omega_R$  and  $V_{\text{QPC}}^0$  are numerical fit parameters. The 44 mT data (green curve in Figure 3(a)) give  $\Omega_R = 1.7 \times 10^6$  s<sup>-1</sup> and  $V_{\text{QPC}}^0 = 2.4$   $\mu$ V. Holding  $V_{\text{QPC}}^0$  to this value, the 550 mT data give  $\Omega_R = 1.8 \times 10^6$  s<sup>-1</sup> (blue curve in Figure 3(a)) and the 185 mT data give the dependence of  $\Omega_R$  on microwave power  $P_{\text{MW}}$  shown in Figure 3(b). The Rabi frequency  $\Omega_R$  increases as  $\sqrt{P_{\text{MW}}}$  (Figure 3(b)) and is independent of  $B$ , both consistent with Equation (1). The  $B$ -independence of  $\Omega_R$  — also evident in the EDSR intensity in Figure 2—and the absence of Rabi oscillations support our interpretation of hyperfine-mediated EDSR in the parameter range investigated <sup>4</sup>

Estimating  $\hbar\omega_0 \sim 1$  meV [63],  $\tilde{E} \sim 3 \times 10^3$  Vm<sup>-1</sup> at maximum applied power <sup>5</sup>,  $d \sim 5$

---

<sup>4</sup>Although  $\Omega_R$  is found to be substantially smaller than the inhomogeneous dephasing rate  $1/T_2^* \sim 100$  MHz, oscillations would still be expected from a coherent process. Quasistatic dephasing processes, such as the hyperfine process dominant here, allow Rabi oscillations to persist even when  $\Omega T_2^*$  is considerably less than unity [55, 73].

<sup>5</sup>The power at the device is calibrated separately at each frequency from the threshold for non-resonant lifting of spin blockade, which we take to indicate a microwave amplitude large enough to configure the dot temporarily in a different charge state. This amplitude corresponds in Figure 1(b) to the 4mV distance from point C to the nearest charge transition. The data in Figure 3(a) and the last data point in Figure 3(b) use power  $2 \pm 1$  dB below this threshold, corresponding to 3.2 mV. Dropped uniformly across the 500 nm width of the device this voltage gives a field  $\tilde{E} \sim 3 \times 10^3$  Vm<sup>-1</sup>.

nm, and using values from the literature  $n_0 = 4 \times 10^{28} \text{ m}^{-3}$  and  $A n_0 = 90 \text{ } \mu\text{eV}$  [74] we calculate  $\Omega_R \sim 11 \times 10^6 \text{ s}^{-1}$ , an order of magnitude larger than measured. The discrepancy may reflect uncertainty in our estimate of  $\tilde{E}$ .

We have neglected any effect of residual exchange in (1,1) during the ESR burst. From the width of the (1,1)-(0,2) charge transition, the interdot tunnel rate  $t_c$  is deduced to be much smaller than Boltzmann's constant multiplied by the electron temperature [75]. From the known (1,1)-(0,2) energy detuning  $\epsilon$  with gate voltages configured at C, we estimate an upper bound on the (1,1) exchange  $t_c^2/\epsilon \ll 80 \text{ neV}$ , of the same order as the hyperfine coupling. Since different choices of point C give qualitatively similar results, we conclude that (1,1) exchange is negligible.

Above, we generalized a mean-field description of the hyperfine interaction [76, 70] to the resonance regime. Justification for this procedure was provided recently in [69]. A distinctive feature of the mean-field theory is a weak overshoot, about 10 - 15%, that is expected in the data of Fig. 3(a) before  $\delta V_{\text{QPC}}^{\text{peak}}(\tau_{\text{EDSR}})$  reaches its asymptotic value at  $\tau_{\text{EDSR}} \rightarrow \infty$ . No overshoot is observed in the 550 mT data (blue symbols in Figure 3(a)), which was taken in a parameter range where an instability of the nuclear polarization begins to develop; see Section 5. For the 44 mT data (green symbols in Figure 3(a)), a considerable spread of experimental points does not allow a specific conclusion regarding the presence or absence of an overshoot. The theory of [69] suggests that the existence of the overshoot is a quite general property of the mean-field theory. However, after passing the maximum, the signal decays to its saturation value very fast, with Gaussian exponent  $e^{-\Omega_R^2 \tau_{\text{EDSR}}^2}$ . By contrast, the first correction to the mean-field theory decays slowly, as  $1/(N\Omega_R^2 \tau_{\text{EDSR}}^2)$ , where  $N$  is the number of nuclei in the dot. As a result, the two terms become comparable at  $\tau_{\text{EDSR}} \sim \sqrt{\ln N}/\Omega_R$ , which should make the maximum less pronounced. Because for

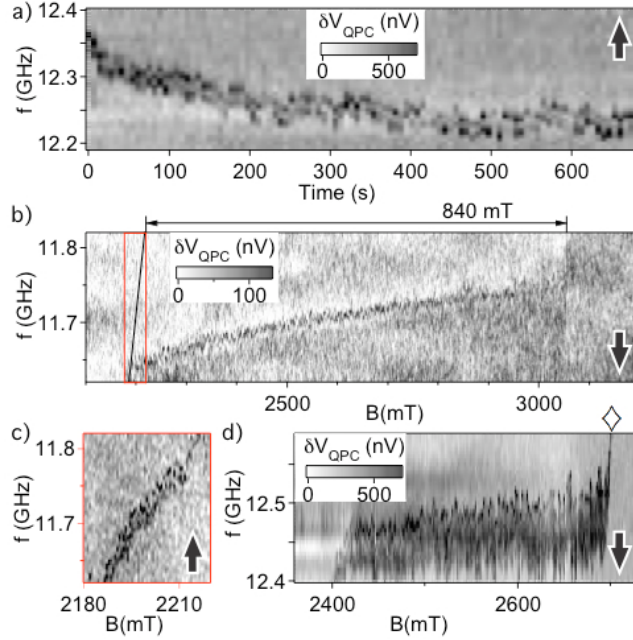


Figure 2.4: (a) Shift of the resonance frequency with time at constant  $B = 2390$  mT, showing build-up of nuclear polarization over  $\sim 200$  s. (b) A scheme to allow larger polarizations: the microwave frequency is repeatedly scanned over the resonance while  $B$  is swept upwards at  $6$  mT/min. Nuclear polarization partly counteracts  $B$ , moving the resonance away from its equilibrium position (black diagonal line) by up to  $840$  mT. (c) Similar data taken at lower microwave power and opposite frequency sweep direction, showing approximately the equilibrium resonance position. (Grey scale as in (b)). (d) Similar data as in (b), with faster sweep rate ( $22$  mT/min), showing more clearly the displacement and subsequent return to equilibrium of the resonance.  $\diamond$  marks the escape of the resonance from the swept frequency window. In all plots, arrows denote frequency sweep direction.

$N \sim 10^5$  the factor  $\sqrt{\ln N} \sim 3$ , the corrections to the mean-field theory manifest themselves surprisingly early, at times only about  $\tau_{\text{EDSR}} \approx 3/\Omega_R$ , making the overshoot difficult to observe.

## 2.5 Nuclear polarization

Consistent with a hyperfine mechanism, this EDSR effect can create a non-equilibrium nuclear polarization [60]. If  $f$  is scanned repeatedly over the resonance at high power, a shift of the resonance develops (Figure 4(a)), corresponding to a nuclear spin alignment parallel to  $\mathbf{B}$ . The effect is stronger at higher  $B$ , and saturates over a timescale  $\sim 200$  s. In Figure 4(b),

we show how to build up a substantial polarization: While slowly increasing  $B$ , we scan  $f$  repeatedly downwards, i.e., in the direction which tracks the moving resonance. The resonance frequency remains approximately fixed, showing that the developing polarization compensates the increase in  $B$ . From the maximum line displacement from equilibrium, an effective hyperfine field of 840 mT can be read off, corresponding to a nuclear polarization of  $\sim 16\%$ . Figure 4(c) shows similar data for lower power and opposite frequency sweep direction, indicating the approximate equilibrium line position. Figure 4(d), similar to Figure 4(b) but with a faster sweep rate, makes the displacement and eventual escape of the resonance clearer although the maximum polarization is less.

The resonance shift is observed to be towards lower frequency, corresponding to a nuclear polarization parallel to  $\mathbf{B}$ . This can be understood if the pulse cycle preferentially prepares the electron ground state  $T_+$  over  $T_-$ , either because it is more efficiently loaded or because of electron spin relaxation. EDSR then transfers this electron polarization to the nuclei [61]. We emphasize that the line shift is opposite to what is given by the usual Overhauser mechanism for inducing nuclear polarization via electron resonance [77, 58].

## 2.6 Addressing individual spins

In quantum information applications, it is desirable to address individual spins selectively [9]. A scheme to allow this is presented in Figure 5. In an otherwise similar device (Figure 5(a)), we incorporated a 100 nm thick micron-scale permalloy (84% Ni, 16% Fe) magnet over 35 nm of atomic-layer-deposited alumina [53, 78]. This device was measured with external field  $\mathbf{B}$  normal to the heterostructure plane. A finite-element simulation of the field  $\mathbf{B}^{\text{mag}}$  due to the micromagnet, assuming complete permalloy magnetization along  $\mathbf{B}$ , yields the field profiles shown in Figure 5(b). The difference in total field  $B^{\text{tot}} = |\mathbf{B} + \mathbf{B}^{\text{mag}}|$

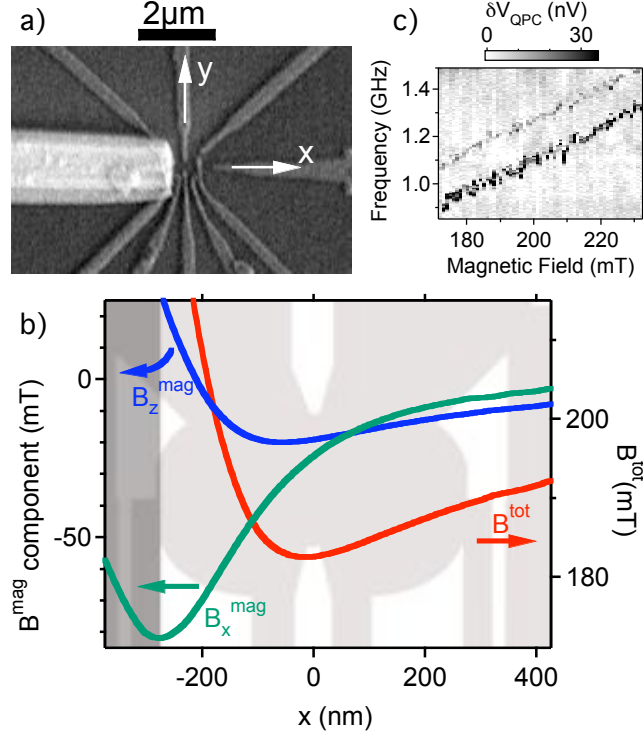


Figure 2.5: (a) A device similar to that of Figure 1, incorporating a micromagnet. (b) Total field magnitude  $B^{\text{tot}}$  (right axis) and the  $x$  and  $z$  components of the micromagnet contribution  $\mathbf{B}^{\text{mag}}$  (left axis), simulated at  $y = 0$  for external field  $B = 200$  mT along  $\hat{\mathbf{z}}$  (out of the plane).  $B_y^{\text{mag}}$  vanishes by symmetry. The gate layout is shown in the background. (c) The associated split EDSR line. The lower resonance is stronger, as expected if the left electron is confined close to the minimum of  $B_{\text{tot}}$ .

between dots is  $\sim 5$  mT. As expected, the EDSR line measured in this device is frequently split (Figure 5(c)). The splitting, 10 – 20 mT depending on precise gate voltage and pulse parameters, is not observed without the magnet and presumably reflects the field difference between dots. Since this splitting is considerably larger than the Overhauser field fluctuations, spins in left and right dots can be separately addressed by matching  $f$  to the local resonance condition [56].

The observation of a field difference between dots raises the possibility of EDSR driven by a field gradient [56]. We cannot exclude a contribution from this effect to the signal in Figure 5(c); however we did not observe the Rabi oscillations which would be expected if the field gradient were the primary EDSR mechanism.

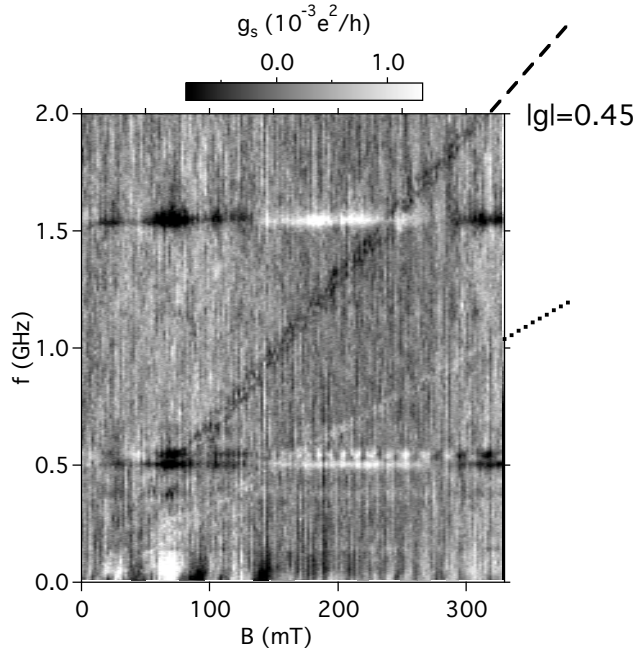


Figure 2.6: Spin resonance signal (measured in conductance) in the device of Figure 5(a). The EDSR signal shows up as a decrease in conductance as expected at frequency corresponding to  $|g| = 0.45$  (marked with dashed line.) An additional signal of opposite sign appears at exactly half this frequency (dotted line). The larger splitting of both signals below 100mT is consistent with a greater contribution of  $B_x^{\text{mag}}$  to the total field difference between dots. The horizontal features at 0.5 and 1.5 GHz result from resonances of the microwave circuit. As in Figure 2, field- and frequency-independent backgrounds have been subtracted, including any signal due to spin blockade lifting around  $B = 0$  [17].

## 2.7 Open issues and discussion

Finally, we discuss unexplained behavior observed only in the device of Figure 5(a). For the data described in this section, a simplified measurement scheme is used: Rather than applying gate pulses, the device is configured in the spin blockade region (point M in Figure 1(a)) throughout. Microwaves are applied continuously, and spin resonance is detected by directly measuring the QPC conductance  $g_s$ .

As well as the EDSR signal at full frequency  $f = g\mu_B B/h$ , an unexpected half-frequency signal is sometimes seen (Figure 6.) Furthermore, depending on the exact gate configuration, both full-frequency and half-frequency signals can have either sign; the change in  $g_s$  at full

frequency is usually negative as expected, but sometimes positive close to degeneracy of (1,1) and (0,2) charge configurations, where spin blockade is weakest [64]; by contrast, the change in  $g_s$  at half frequency is usually positive but sometimes negative far from degeneracy. For most gate configurations, full-frequency and half-frequency signals have opposite sign, as seen in Figure 6.

A half-frequency response is as far as we know unprecedented in spin resonance, and suggests second harmonic generation (SHG) from the microwave field. SHG is generally a non-linear phenomenon; it occurs for example in optical materials with non-linear polarizability [79] and in non-linear electronic components. For hydrogenic donors in a semiconductor, the nonlinear dependence of  $g$ -tensor on electric field has been predicted to drive EDSR at subharmonics of the Larmor frequency [80]. In our system, a hyperfine field at a harmonic of the microwave frequency arises if the confinement potential is non-parabolic.

However, SHG alone does not explain the sign of the conductance change seen at half-frequency in Figure 6. The positive signal would be consistent with a reduced admixture of (0,2), corresponding to a unexpected enhancement of the spin lifetime by microwaves. Alternatively, a positive signal could be caused by an admixture of the (0,1) charge state; but it is observed even for the gate configurations where (0,1) is energetically inaccessible (in the top right of the spin blockade region of Figure 1(b)). Also, there is no reason why (0,1) should be admixed for one resonance but not the other. These anomalous behaviours are therefore left unexplained.

We acknowledge useful discussions with Al. L. Efros, H.-A. Engel, F. H. L. Koppens, J. R. Petta, D. J. Reilly, M. S. Rudner, J. M. Taylor, and L. M. K. Vandersypen. We acknowledge support from the DTO and from DARPA. E. I. R. was supported in part by a Rutherford Professorship at Loughborough University, U.K.

## Chapter 3

# Effect of Exchange Interaction on Spin Dephasing in a Double Quantum Dot

E. A. Laird, J. R. Petta, A. C. Johnson, C. M. Marcus

*Department of Physics, Harvard University, Cambridge, Massachusetts 02138*

A. Yacoby

*Department of Condensed Matter Physics, Weizmann Institute of Science, Rehovot 76100, Israel*

M. P. Hanson, A. C. Gossard

*Department of Materials, University of California, Santa Barbara, California 93106*

We measure singlet-triplet dephasing in a two-electron double quantum dot in the presence of an exchange interaction which can be electrically tuned from much smaller to much larger than the hyperfine energy. Saturation of dephasing and damped oscillations of the spin correlator as a function of time are observed when the two interaction strengths are comparable. Both features of the data are compared with predictions from a quasistatic model of the hyperfine field.<sup>2</sup>

---

<sup>2</sup>This chapter is adapted from Ref. [68] [with permission, © (2006) by the American Physical Society].

### 3.1 Introduction

Implementing quantum information processing in solid-state circuitry is an enticing experimental goal, offering the possibility of tunable device parameters and straightforward scaling. However, realization will require control over the strong environmental decoherence typical of solid-state systems. An attractive candidate system uses electron spin as the holder of quantum information [9, 39]. In III-V semiconductor quantum dots, where the highest degree of spin control has been achieved [81, 18, 82, 83, 84, 65, 40], the dominant decoherence mechanism is hyperfine interaction with the lattice nuclei [85, 70, 76]. A recent experiment [40] studied this decoherence in a qubit encoded in a pair of spins [38]. In this situation, the dynamics are governed by two competing effects: the hyperfine interaction, which tends to mix the singlet and triplet basis states, and exchange, which tends to preserve them.

The interplay of hyperfine and exchange effects has been studied recently via spin-blockaded transport in two double-dot systems [66, 64]. Oscillations and bistability [66] of the leakage current, as well as suppression of mixing with stronger exchange [64] were observed. The topic also has a long history in physical chemistry: recombination of a radical pair created in a triplet state proceeds significantly faster for radicals containing isotopes whose nuclei carry spin [86, 87]. By lifting the singlet-triplet degeneracy, the exchange interaction suppresses spin transitions; its strength can be deduced from the magnetic field dependence of the recombination rate [88, 89]. However, exchange is difficult to tune *in situ* in chemical systems.

In this Letter, singlet correlations between two separated electrons in a GaAs double dot system are measured as a function of a gate-voltage tunable exchange  $J$  and as a function of time  $\tau_S$  following the preparation of an initial singlet. This study gives insight into

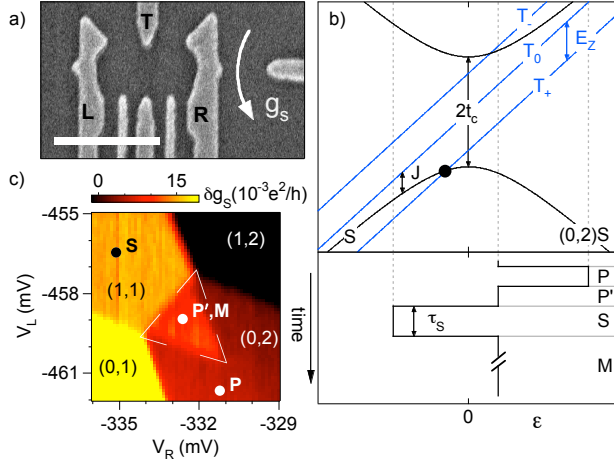


Figure 3.1: (a) Micrograph of a device with the same gate design as the one measured (Scale bar = 500 nm.) Voltages applied to gates L and R adjust the double dot detuning,  $\epsilon$ . Gate T sets the inter-dot tunnel coupling. The conductance  $g_s$  of a nearby sensor quantum point contact monitors the average occupation of each dot. (b) Upper panel: Level diagram for the double dot near the (1,1)-(0,2) transition ( $\epsilon = 0$ ) plotted versus  $\epsilon$ . Exchange ( $J$ ) and Zeeman ( $E_Z$ ) energies are indicated. • denotes the S-T<sub>+</sub> degeneracy. Labels ( $m, n$ ) denote the occupancies of the left and right dot respectively. Lower panel: The prepare (P, P') - separate (S) - measure (M) pulse scheme.  $\sim 90\%$  of the cycle is spent in M. (c)  $g_s$  close to the (1,1)-(0,2) transition during application of pulses, showing the pulse triangle (marked) and the positions of points P, P', S and M. A background plane has been subtracted.

the interplay of local hyperfine interactions and exchange in a highly controllable quantum system. We measure the probability  $P_S(\tau_S)$  that an initial singlet will be detected as a singlet after time  $\tau_S$  for  $J$  ranging from much smaller than to much greater than the rms hyperfine interaction strength in each dot,  $E_{\text{nuc}}$ . When  $J \ll E_{\text{nuc}}$ , we find that  $P_S$  decays on a timescale  $T_2^* \equiv \hbar/E_{\text{nuc}} = 14$  ns. In the opposite limit where exchange dominates,  $J \gg E_{\text{nuc}}$ , we find that singlet correlations are substantially preserved over hundreds of ns. In the intermediate regime, where  $J \sim E_{\text{nuc}}$ , we observe oscillations in  $P_S$  that depend on the ratio  $E_{\text{nuc}}/J$ . Our results show that a finite exchange energy can be used to extend spin correlations for times well beyond  $T_2^*$ .

These observations are in reasonable agreement with recent theory, which predicts a singlet probability (assuming perfect readout)  $P_S^0(\tau_S)$  that exhibits damped oscillations as

a function of time and a long-time saturation that depends solely on the ratio  $E_{\text{nuc}}/J$  [90].

To compare experiment and theory quantitatively we introduce an empirical visibility,  $V$ , to account for readout inefficiency,  $P_S(\tau_S) = 1 - V(1 - P_S^0(\tau_S))$ .

## 3.2 Device

The device used in the experiment, shown in Fig. 1(a), is fabricated on a GaAs/Al<sub>0.3</sub>Ga<sub>0.7</sub>As heterostructure with a two-dimensional electron gas (density  $2 \times 10^{15} \text{ m}^{-2}$ , mobility  $20 \text{ m}^2/\text{Vs}$ ) 100 nm below the surface. Ti/Au top gates define a few-electron double quantum dot. The inter-dot tunnel coupling  $t_c$  and (0,2)-(1,1) detuning  $\epsilon$  are also separately tunable. A charge-sensing quantum point contact with conductance  $g_s \sim 0.2e^2/h$  allows the occupancy of each dot to be separately measured [27, 30]. We monitor  $g_s$  using a lock-in amplifier with a 1 nA current bias at 335 Hz, with a 30 ms time constant.

## 3.3 Methods

Measurements were made in a dilution refrigerator at electron temperature  $T_e \approx 100 \text{ mK}$  measured from the width of the (1,1)-(0,2) transition [75]. Gates L and R (see Fig. 1) were connected via filtered coaxial lines to the outputs of a Tektronix AWG520. We report measurements for two settings of tunneling strength, controlled using voltages on gate T and measured from the width of the (1,1)-(0,2) transition:  $t_c \approx 23 \mu\text{eV}$  (“large  $t_c$ ”) and  $t_c < 9 \mu\text{eV}$  (“small  $t_c$ ”) [75]. Except where stated, measurements were made in a perpendicular magnetic field of 200 mT, corresponding to a Zeeman energy  $E_Z = 5 \mu\text{eV} \gg E_{\text{nuc}}$ .

Figure 1(b) shows the relevant energy levels near the (1,1)-(0,2) charge transition, where measurements are carried out, as a function of energy detuning  $\epsilon$  between these two charge

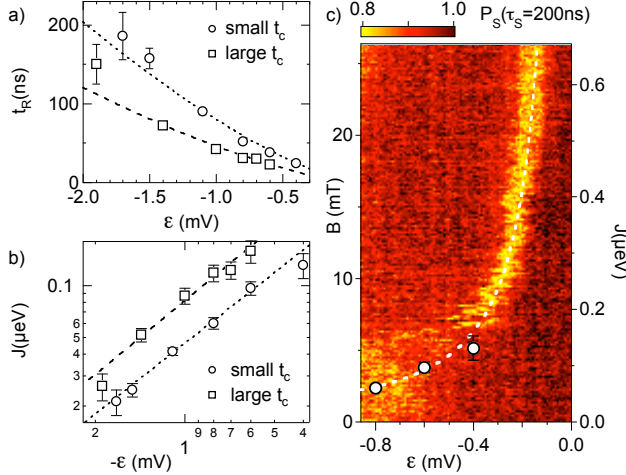


Figure 3.2: (a) Period  $t_R$  of first Rabi oscillation versus exchange point detuning for small and large tunnel coupling. (b) Exchange energy as a function of detuning, deduced from the data in (a), together with empirical power-law fits  $J \propto |\epsilon|^{-1.4 \pm 0.1}$ .  $t_R$  corresponding to the fits is shown as curves in (a). (c) Color scale plot of  $P_S$  as a function of S-point detuning and magnetic field  $B$  obtained using the pulse sequence in Fig. 1(b). The bright band indicates rapid decoherence where  $J = g\mu_B B$ . The white points and the dashed line are the same data and fits plotted in (b).

states. With  $t_c=0$ , the (1,1) singlet S and  $m_s = 0$  triplet  $T_0$  are degenerate; the  $m_s = \pm 1$  triplets  $T_{\pm}$  are split off in energy from  $T_0$  by  $\mp E_Z$ . Finite  $t_c$  leads to hybridization of the (0,2) and (1,1) singlets, inducing an exchange splitting  $J$  between S and  $T_0$ . The (0,2) triplet (not shown) is split off by the much larger intra-dot exchange energy  $J_{(0,2)} \sim 600$   $\mu\text{eV}$  [31] and is inaccessible. Rapid mixing due to hyperfine interaction occurs between states whose energies differ by less than  $E_{\text{nuc}}$ . This occurs at large negative  $\epsilon$  (lower left of Fig. 1(b)), where S and  $T_0$  mix, and at  $J(\epsilon) = E_Z$  (black dot in Fig. 1(b)), where S and  $T_{\pm}$  mix.

A cycle of gate configurations is used to prepare and measure two-electron spin states [40], as illustrated in Fig. 1(b). A 200 ns preparation step (denoted P in Fig. 1) configures the dot in (0,2) at a position where the series (0,2)T $\rightarrow$ (0,1) $\rightarrow$ (0,2)S is energetically allowed and occurs rapidly, giving efficient initialization to a singlet. The gates then shift (waiting 200 ns at P' to reduce pulse overshoot) to a separation point (S) in (1,1) for a time  $\tau_S$

during which singlet-triplet evolution occurs. Finally, the gates are set to the measurement point (M) for  $\tau_M = 5 \mu\text{s}$ , for spin-to-charge conversion. Inside the pulse triangle marked in Fig. 1(c), the triplet states will remain in (1,1) over the measurement time  $\tau_M$  [65, 91]. Since  $\sim 90\%$  of the pulse cycle is spent at M, the relatively slow measurement of the sensor  $g_s$  gives a time-averaged charge configuration at the M point. The time-averaged  $g_s$  signal is calibrated to give a singlet state probability  $P_S(\tau_S)$  by comparing the signal in the pulse triangle with the values measured in the (1,1) and (0,2) regions of the charge stability diagram. When the gates are configured so that M is outside the pulse triangle in (0,2), both singlet and triplet relax rapidly to (0,2);  $g_s$  in this region defines  $P_S = 1$ . When M is in (1,1), the value of  $g_s$  defines  $P_S = 0$ .

### 3.4 Measurement of exchange energy, hyperfine interaction strength and readout visibility

We first measure  $J(\epsilon)$ ,  $E_{\text{nuc}}$ , and  $V$  at two values of  $t_c$ , allowing the saturation probability  $P_S(\infty)$  to be measured as a function of  $J$ . This saturation probability is found to depend on the ratio  $E_{\text{nuc}}/J$  approximately as predicted by theory [90]. We then measure the time evolution  $P_S(\tau_S)$ , which shows damped oscillations, also in reasonable agreement with theory [90].  $J(\epsilon)$  is measured using the Rabi (or Larmor) sequence described in Ref. [40], in which an adiabatic (compared with  $E_{\text{nuc}}$ ) ramp over  $1 \mu\text{s}$  to (1,1) is used to prepare and measure the electron spin state in the  $\{|\uparrow\downarrow\rangle, |\downarrow\uparrow\rangle\}$  basis. An exchange pulse produces coherent rotations with a period  $t_R$  (shown in Fig. 2(a)) from which we deduce the exchange

coupling  $J(\epsilon) = h/t_R$ <sup>3</sup>. Values of  $J(\epsilon)$  for small and large  $t_c$  are shown in Fig. 2(b), along with a fit to an empirical power-law form  $J \propto \epsilon^{-\alpha}$ , giving  $\alpha \sim 1.4$ <sup>4</sup>. In Fig. 2(c), these values of  $J(\epsilon)$  are compared with the results of an alternative method in which rapid dephasing at the S-T<sub>+</sub> degeneracy produces a dip in  $P_S$  when the value of  $\epsilon$  at the S point satisfies  $J(\epsilon) = E_Z$ .  $J(\epsilon)$  can then be measured from a knowledge of the field, using  $E_Z = g\mu_B B$  where  $\mu_B$  is the Bohr magneton, and taking the value  $g = -0.44$ , measured (using an in-plane field) in a different quantum dot device on made from the same wafer [92].  $J(\epsilon)$  measured by this technique is in qualitative agreement with the power-law derived from Fig. 2(b); discrepancies may be due to an anisotropic  $g$ -factor, nuclear polarization effects, or may indicate a dependence of  $J(\epsilon)$  on field. Since the first method more closely matches the conditions under which data in the rest of the paper was taken and is more precise in the range of  $J$  of interest, we henceforth take the function  $J(\epsilon)$  from Fig. 2(b).

Parameters  $E_{\text{nuc}}$  and  $V$  are extracted from  $P_S(\tau_S)$  measured for the S-point at large negative  $\epsilon$ , where  $J \ll E_{\text{nuc}}$ . In this regime the initial singlet evolves into an equal mixture of singlet and triplet with characteristic time  $h/E_{\text{nuc}}$ .  $P_S(\tau_S)$  for small and large  $t_c$  (shown in the insets of Fig. 3) are fit to the form for  $P_S^0(\tau_S)$  given in [90], with fit parameters  $E_{\text{nuc}} = 45 \pm 3$  neV ( $47 \pm 4$  neV) and  $V = 0.53 \pm 0.06$  ( $0.46 \pm 0.06$ ) for small (large)  $t_c$ <sup>5</sup>. These hyperfine energies correspond to an effective hyperfine field of 1.8 mT, similar to the

---

<sup>3</sup>When  $J \lesssim E_{\text{nuc}}$ ,  $J$  must be corrected downwards slightly because precession in the nuclear field enhances the average Rabi frequency. The correction to  $J$  never exceeds 13%.

<sup>4</sup>A simple level anticrossing with  $t_c$  and  $\epsilon$  independent would give  $J \propto \epsilon^{-1}$ . The discrepancy may be due to a detuning-dependent  $t_c$

<sup>5</sup>The dependence of  $V$  on  $t_c$  is not understood. The effect of alternative visibility parameters on the predictions of Figs. 3 and 4 is simply to scale them towards or away from  $P_S = 1$

value measured previously on this device [40]. The fit function  $P_S^0(\tau_S)$  depends on  $J$  at this detuning, which is too small to measure directly. To perform the fit, we choose a value  $J(\epsilon)$  extrapolated using the power-law from Fig. 2b; however, since  $J$  is so small at this large  $|\epsilon|$ , the best-fit parameters are essentially independent of details of the extrapolation, and, for example, are within the error bars for the alternative extrapolations  $J \propto |\epsilon|^{-1}$  and  $J = 0$ .

### 3.5 Saturation singlet probability

The variance of the hyperfine field arises either from a quantum superposition of nuclear-field eigenstates or through dynamics of the nuclear system on timescales faster than the measurement averaging time [90].  $P_S^0(\tau_S)$  is calculated by integrating Schrödinger's equation from the initial singlet for given nuclear field and averaging the resulting singlet probability over nuclear fields. The resulting  $P_S^0(\tau_S)$  shows a range of interesting behavior depending on the relative magnitudes of  $J$  and  $E_{\text{nuc}}$  [90]: In the limit  $J = 0$ ,  $P_S^0(\tau_S \rightarrow \infty)$  rapidly saturates to 1/2. As  $J$  is increased, hyperfine dephasing becomes less effective, with  $P_S^0(\infty)$  saturating at progressively higher values, approaching unity when  $J \gg E_{\text{nuc}}$ , and following a universal function of  $E_{\text{nuc}}/J$ . As a function of  $\tau_S$ ,  $P_S^0(\tau_S)$  is predicted to undergo damped oscillations, which when plotted versus  $\tau_S J$  follow another universal function of  $E_{\text{nuc}}/J$  and exhibit a universal phase shift of  $3\pi/4$  at large  $\tau_S J$ .

Knowing  $J(\epsilon)$  and  $E_{\text{nuc}}$  allows the long-time ( $\tau_S \gg h/J$ ) saturation of the measured  $P_S$  to be compared with theory [90]. We set  $\tau_S = 400$  ns and sweep the position of the S-point. For small and large  $t_c$ ,  $P_S(400$  ns) is plotted in Fig. 3 as a function of  $E_{\text{nuc}}/J$ , where  $E_{\text{nuc}}$  is obtained from the fits described above and  $J(\epsilon)$  are taken from Fig. 2. At the most negative detunings (in the regions marked by gray bars in Fig. 3)  $J$  is too small to be measured by either Rabi period or S-T<sub>+</sub> degeneracy methods; instead,  $J(\epsilon)$  is found by extrapolating

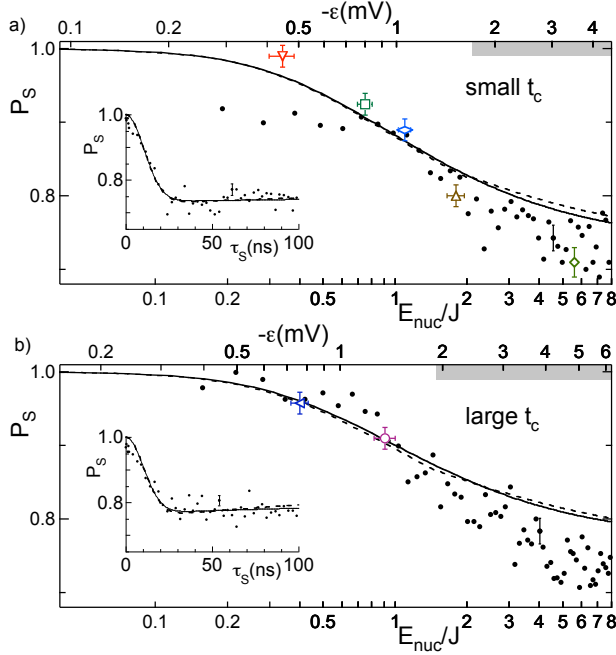


Figure 3.3: (a) Inset:  $P_S(\tau_S)$  for small  $t_c$  and  $\epsilon = -5.5$  mV, with fit (see text) giving  $E_{\text{nuc}} = 45 \pm 3$  neV and  $V = 0.53 \pm 0.06$ . Main panel: Measured  $P_S(\tau_S = 400 \text{ ns})$  (points) plotted against  $E_{\text{nuc}}/J$ . Open symbols correspond to  $P_S$  in the traces of Fig. 4(a) at the largest  $\tau_S$  measured for each  $\epsilon$ . Curve shows theoretical dependence (from [90]) of  $P_S(\tau_S \rightarrow \infty)$  on  $E_{\text{nuc}}/J$ , taking into account the measurement fidelity deduced from the inset. The gray bar along the top axis indicates the region where  $J(\epsilon)$  is extrapolated (see text). Dashed lines indicate the theoretical predictions (plotted as functions of  $\epsilon$ ) if an alternative extrapolation  $J \propto |\epsilon|^{-1}$  is chosen in this region. (b) Large  $t_c$  data. The fit to the inset gives  $E_{\text{nuc}} = 47 \pm 4$  neV and  $V = 0.46 \pm 0.06$ , from which the theoretical saturation  $P_S$  (curve in main panel) is calculated. Open symbols correspond to the large- $\tau_S$  values in Fig. 4(b). Error bars on the filled symbols shows the uncertainty in  $P_S$  arising from charge noise in the sensing point contact.

the power-law fits (Fig. 2.) Agreement with theory (discussed below) is insensitive to the details of the extrapolation, as shown by the dashed lines in Fig. 2.

The long- $\tau_S$   $P_S$  data shown in Fig. 3 agrees fairly well with the saturation values predicted from [90], taking into account the visibility (assumed independent of  $\epsilon$ ) obtained from the insets. In particular,  $P_S$  has the same dependence on  $E_{\text{nuc}}/J$  at both values of  $t_c$  measured, even though the function  $J(\epsilon)$  depends on  $t_c$ .  $P_S$  is up to  $\sim 0.06$  smaller than predicted at the largest detunings; both cotunneling and nuclear decorrelation over the duration of the separation pulse tend to equalize singlet and triplet occupations, although it

is unclear whether they are the cause of this effect.

### 3.6 Time-dependence of the singlet probability

We next investigate the time dependence of  $P_S(\tau_S)$  at finite  $J$ . For five (two) S-point detunings at small (large)  $t_c$ ,  $P_S(\tau_S)$  was measured out to  $\tau_S J / \hbar \approx 15$ . The results are shown in Fig. 4, together with the predicted time evolution from [90] with values for  $V$  and  $E_{\text{nuc}}$  taken from fits shown in the insets of Fig. 3. Because  $P_S$  remains close to unity, these data are particularly sensitive to calibration imperfections caused by quantum point contact nonlinearities and noise in the calibration data, whose effect to lowest order is to shift the data vertically. Traces in Fig. 4 are therefore shifted vertically to satisfy the constraint  $P_S(\tau_S = 0) = 1$ . In no case was this greater than  $\pm 0.05$ . Here and in Fig. 3, the error bars reflect uncertainty in  $P_S$  from charge noise in the sensing point contact; additional scatter in the data may be due to long nuclear correlation times [40, 64].

Damped oscillations are observed as predicted in [90]; however, even after taking account the empirical visibility factor, the amplitude of the oscillations is less than expected. This is likely due to the finite rise time of the separation pulse and to switching noise, which make each trace effectively an average over a range of  $J$  values. Where the amplitude is large enough for the period and phase of the oscillations to be made out, these approximately match the predictions of [90], although with two significant departures: The topmost trace, with smallest  $E_{\text{nuc}}/J$ , does not show clear oscillations, and the expected shift of the first minimum to smaller  $\tau_S J$  at intermediate  $J$  is not observed. We do not understand the origin of these effects. The amplitude of the oscillations falls off too rapidly for the expected  $3\pi/4$  phase shift at large  $\tau_S J$  to be visible. Similar oscillations of  $P_S$  are predicted close to the S-T<sub>+</sub> degeneracy with a characteristic frequency  $\sim \Delta = J - E_Z$ . We have searched for these

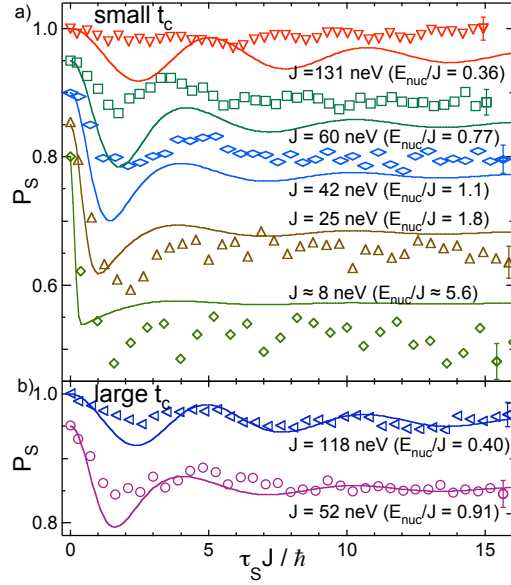


Figure 3.4: (a) Symbols: Experimental  $P_S(\tau_S)$  at small  $t_c$  for various  $J$ , plotted as a function of  $\tau_S J / \hbar$ . Curves: Predictions from [90] using  $E_{\text{nuc}}$  and  $V$  fit from Fig. 3(a). Adjacent traces after the first are offset by 0.05 for clarity. (b) Corresponding data and theory for large  $t_c$ . Lower trace is offset by 0.05 for clarity. Error bars reflect the contribution of sensor charge noise.

oscillations but do not observe them. We believe the reason for this is that  $\Delta$  varies much more rapidly with  $\epsilon$  in this region than  $J$  does at the S-T<sub>0</sub> near-degeneracy; the oscillations are therefore washed out by switching noise and pulse overshoot.

### 3.7 Summary and acknowledgements

In summary, after including the measured readout efficiency, we find that the singlet correlator shows damped oscillations as a function of time and saturates at a value that depends only on  $E_{\text{nuc}}/J$ . Both these features are qualitatively as expected from theory [90]; some of the departures from expected behavior may be qualitatively accounted for by cotunneling and nuclear decorrelation (which tend to equalize singlet and triplet probabilities at long times), and charge noise (which tends to smear out the oscillations seen in Fig. 4.)

We acknowledge useful discussions with W. Coish, H. A. Engel, D. Loss, M. Lukin, J. M.

Taylor. This work was supported by DARPA-QuIST and the ARO/ARDA STIC program.

## Chapter 4

# Coherent operation of an exchange-only qubit

E. A. Laird, C. M. Marcus

*Department of Physics, Harvard University, Cambridge, Massachusetts 02138*

J. M. Taylor

*National Institute of Standards and Technology, Gaithersburg, Maryland 20899*

D. P. DiVincenzo

*IBM T. J. Watson Research Center, Yorktown Heights, New York 10598*

M. P. Hanson, A. C. Gossard

*Department of Materials, University of California, Santa Barbara, California 93106*

A triplet quantum dot is tuned to a charge configuration useful for operation as an exchange-controlled spin qubit. For qubit readout, we apply the technique of frequency-multiplexed reflectometry to a pair of charge sensing quantum point contacts. With a series of gate pulses applied to the device, we demonstrate qubit initialization and readout and use the exchange interaction to carry out coherent spin manipulation.

## 4.1 Introduction

Electron spins confined in semiconductor quantum dots are an attractive physical basis for quantum computing because of their long coherence times and potential for straightforward scaling [9, 93, 39]. In the simplest proposal [9], the single-spin states  $|\uparrow\rangle$  and  $|\downarrow\rangle$  form the logical basis, with single-qubit operations via electron spin resonance (ESR) and two-qubit operations via exchange. The technical difficulty of single-spin ESR [17] inspired an alternative scheme in which the logical basis is formed from the singlet and triplet states of a spin pair [38, 40, 39]. No time-varying ESR field is then necessary, but an inhomogeneous static magnetic field is required for full single-qubit control [41]. Using three electron spins to represent each qubit removes the need for an inhomogeneous field; exchange between adjacent spins suffices for one and two-qubit operations as well as state preparation and readout [93]. Here we present a three-spin qubit defined in a triple quantum dot. A pair of proximal charge sensors, monitored independently using frequency-multiplexed reflectometry, allows rapid readout of the electron configuration. Pulsing gate voltages to tune the energy levels of the system, we demonstrate initialization, coherent operation, and measurement of the qubit.

The interactions of three spins have been explored experimentally [94] and theoretically [95] in the context of physical chemistry, where the recombination of two radicals, originally in an unreactive triplet state, can be catalyzed by exchange with a third spin. Few-electron triple quantum dots [96, 97, 98] have been used to realize charge reconfigurations corresponding to the elementary operations of quantum cellular automata have been measured [99], however, tunable spin interactions have not yet been demonstrated [100].

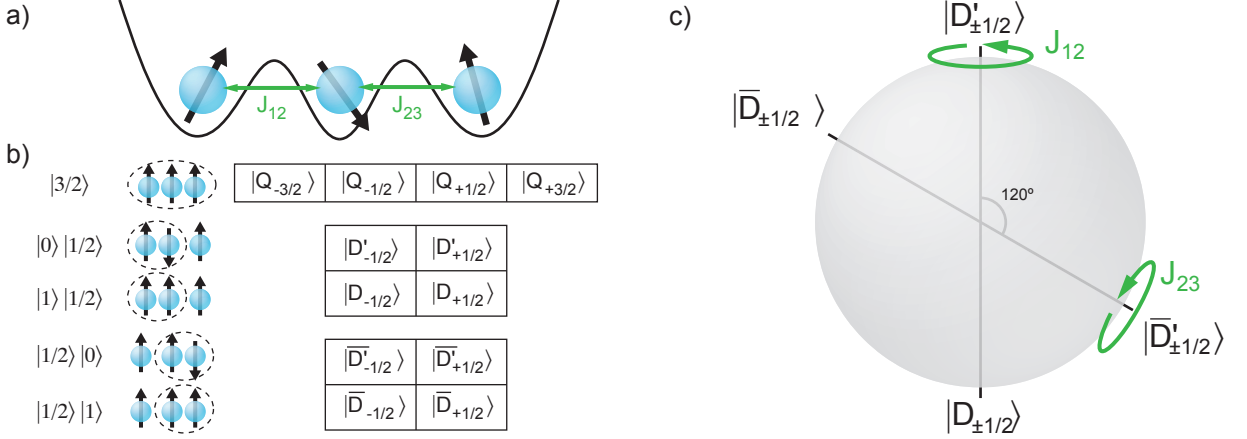


Figure 4.1: An exchange-only qubit. **a**, Electron spins in three adjacent quantum dots are coupled by nearest-neighbour exchange. **b**, The eight states of the system form a quadruplet  $Q$  and two doublets  $D'$  and  $D$  characterized by the multiplicity (singlet or triplet) of the leftmost pair of spins. Alternatively the doublets can be classified according the multiplicity of the rightmost pair and labelled  $\bar{D}$  and  $\bar{D}'$ . **c**, Choosing an element from each doublet as the qubit basis, arbitrary unitary transformations are equivalent to rotations on the Bloch sphere shown. Doublet states  $|D'_{\pm 1/2}\rangle$  and  $|D_{\pm 1/2}\rangle$  are denoted by the north and south poles, and states  $|\bar{D}'_{\pm 1/2}\rangle$  and  $|\bar{D}_{\pm 1/2}\rangle$  by points on an axis rotated by  $120^\circ$ . Exchange between left and middle dots drives rotations about the  $D - D'$  axis, whereas exchange between middle and right dots drives rotations about the  $\bar{D} - \bar{D}'$  axis. In combination, any rotation can be accomplished.

## 4.2 Exchange in a three-spin system

To see how exchange interaction allows arbitrary qubit operations, consider three electron spins coupled by nearest-neighbour exchange strengths  $J_{12}$  and  $J_{23}$  (Fig. 4.1(a)) [93]. The eight spin states can be classified by both overall multiplicity and multiplicity of the leftmost spin pair, and comprise a quadruplet of states  $|Q_{S_z}\rangle$  and two doublets of states  $|D'_{S_z}\rangle$  and  $|D_{S_z}\rangle$ , where  $S_z$  denotes the  $z$ -component of total spin and takes values  $S_z = \pm 1/2$  or  $\pm 3/2$  for the quadruplet and  $S_z = \pm 1/2$  for the doublets (Fig. 4.1(b)) [95]. Whereas for  $|D'_{S_z}\rangle$  states, the leftmost pair of spins is a singlet, for  $|D_{S_z}\rangle$  states, the leftmost pair is a mixture of triplet states. An alternative doublet classification is based on the multiplicity of the rightmost pair: States  $|\bar{D}'_{S_z}\rangle$  correspond to singlets on the right whereas states  $|\bar{D}_{S_z}\rangle$  correspond to triplet states.

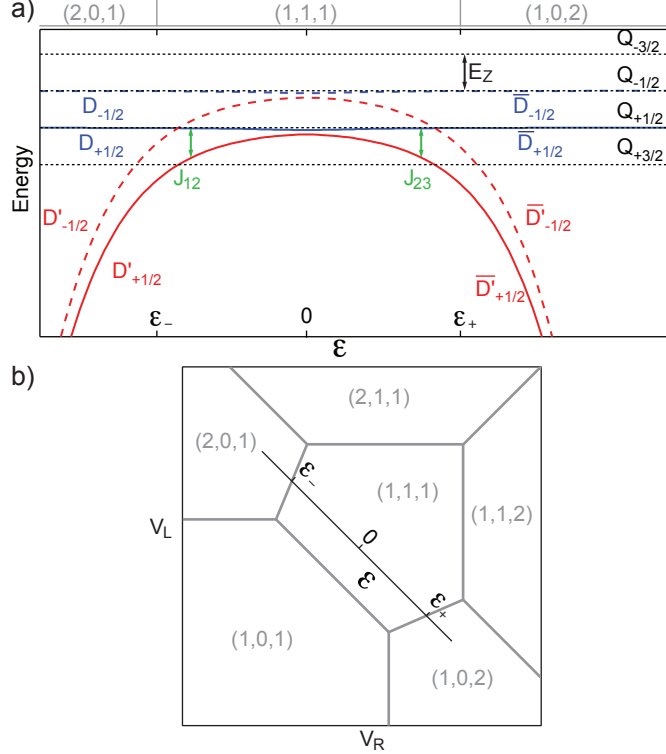


Figure 4.2: Electron states of a triple quantum dot. **a**, Energy levels as a function of detuning  $\epsilon$ , showing Zeeman and exchange splitting. Near zero detuning the device is configured in  $(1,1,1)$  with negligible exchange; increasing (decreasing)  $\epsilon$  lowers the energy of the  $\bar{D}'$  ( $D'$ ) doublet by exchange  $J_{23}$  ( $J_{12}$ ). For  $\epsilon > \epsilon_+$  ( $\epsilon < \epsilon_-$ ), states in doublet  $\bar{D}'$  ( $D'$ ) correspond to a predominant  $(1,0,2)$  ( $(2,0,1)$ ) configuration. **b**, Ground-state configuration of a triple dot as a function of gate voltages  $V_L$  and  $V_R$  coupled to left and right dots. The detuning axis is shown.

The logical basis is formed from two states with equal  $S_z$ , one taken from each doublet  $|D'_{S_z}\rangle$  and  $|D_{S_z}\rangle$ . States of the qubit correspond to points on the surface of the Bloch sphere shown in Fig. 4.1(c). Whereas exchange  $J_{12}$  between the leftmost spin pair drives qubit rotations about the vertical axis, exchange  $J_{23}$  between the rightmost pair drives rotations about an axis tilted by  $120^\circ$  and connecting elements from doublets  $|\bar{D}'_{S_z}\rangle$  and  $|\bar{D}_{S_z}\rangle$ . Arbitrary single-qubit operations can be achieved by concatenating up to four exchange pulses [93]. Implementation of this scheme is simplified by the fact that valid qubits can be formed using either  $S_z = +1/2$  or  $S_z = -1/2$  doublet components; it is therefore only necessary to prepare and read out two of the three spins to operate the qubit.

The energy levels of the triple quantum dot are tuned with an external magnetic field  $B$  and by using gate voltages to adjust the energy differences between different charge configurations  $(N_L, N_M, N_R)$ , where  $N_L$ ,  $N_M$  and  $N_R$  denote electron occupancies of left, middle and right dots respectively. Defining the detuning  $\epsilon$  as the energy difference between  $(2,0,1)$  and  $(1,0,2)$  configurations, three regimes are accessible (Fig. 4.2(a)). Near  $\epsilon = 0$ , the device is in the  $(1,1,1)$  configuration with negligible exchange. Neglecting hyperfine coupling, spin states are split only by the Zeeman energy  $E_Z = g\mu_B B$ , where  $g$  is the electron  $g$ -factor and  $\mu_B$  is the Bohr magneton. As  $\epsilon$  is decreased, hybridization between  $(1,1,1)$  and  $(2,0,1)$  configurations lowers the energy of  $|D'_{S_z}\rangle$  states, until for  $\epsilon < \epsilon_-$ , the ground state configuration becomes predominantly  $(2,0,1)$ . Because Pauli exclusion prevents occupation of the  $(2,0,1)$  configuration with  $|Q_{S_z}\rangle$  and  $|D_{S_z}\rangle$  spin states, an exchange splitting  $J_{12}$  results for  $\epsilon < 0$ . Similarly, with increasing  $\epsilon$  the energy of  $|\bar{D}_{S_z}\rangle$  states is lowered by an amount  $J_{23}$ , and above  $\epsilon = \epsilon_+$  the ground state configuration becomes predominantly  $(1,0,2)$ . The various configurations are accessed by tuning gate voltages  $V_L$  and  $V_R$  coupled predominantly to left and right dots respectively. The lowest-energy configurations of three capacitively coupled dots are modeled in Fig. 4.2(b), which also illustrates the detuning axis in gate space.

### 4.3 Device and methods

The measured device (Fig. 4.3(a)) was fabricated by patterning Ti/Au topgates on a GaAs/AlGaAs heterostructure incorporating a two-dimensional electron gas 100 nm beneath the surface. Depletion gate voltages create a triple quantum dot together with a pair of charge sensing quantum point contacts (QPCs) [27]. Four of the gates, including those marked L and R, were connected to coaxial lines allowing rapid voltage pulses to be

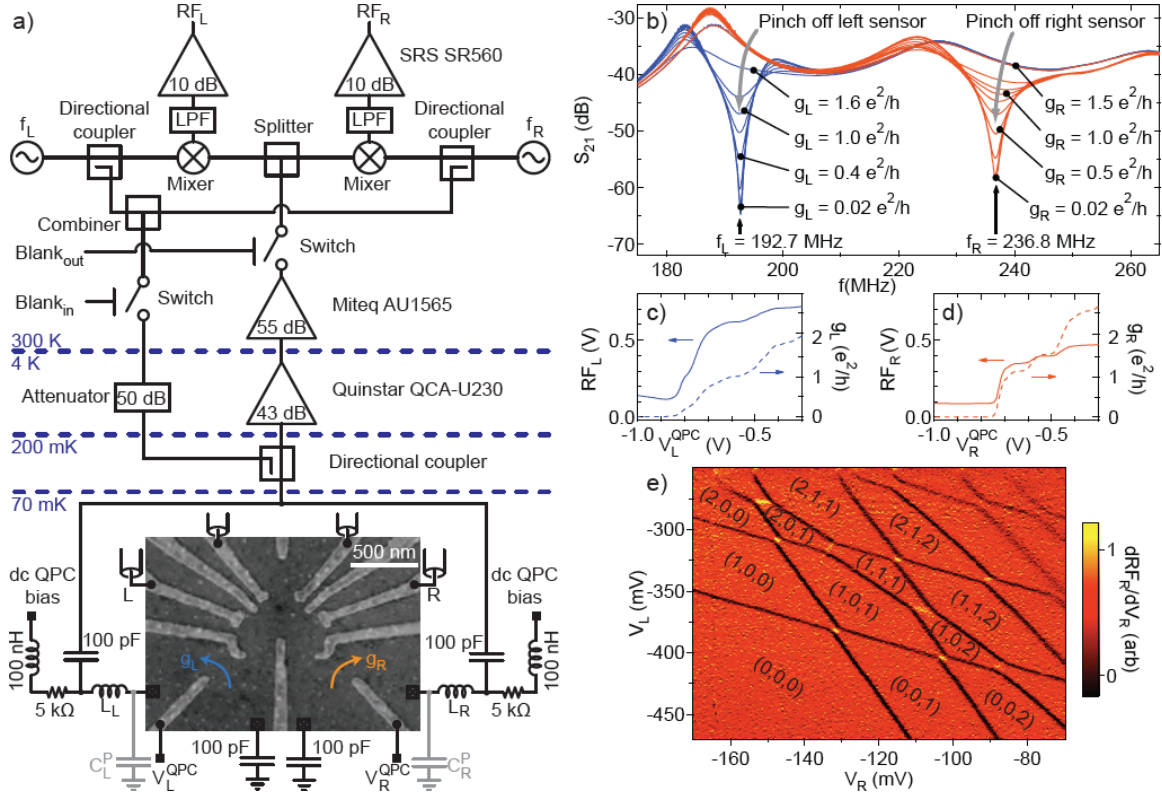


Figure 4.3: Fast measurements with two charge sensors **a**, Device and measurement circuit. Patterned topgates define three quantum dots and QPC charge sensors on left and right; voltages applied to gates L and R control the energy levels of the device, while voltages  $V_L^{QPC}$  and  $V_R^{QPC}$  tune QPC conductances  $g_L$  and  $g_R$ . The QPCs are connected on one side to 100 pF grounding capacitors and on the other to resonant tank circuits comprising chip inductors  $L_L$  and  $L_R$  combined with parasitic capacitances  $C_L^P$  and  $C_R^P$ ; bias tees allow the QPCs to be measured both at DC and via RF reflectometry. An RF carrier, generated by combining signals at resonant frequencies  $f_L$  and  $f_R$ , is applied to the device via a directional coupler; the reflected signal, after amplification, is demodulated by mixing with the original carrier frequencies to yield voltages  $RF_L$  and  $RF_R$  sensitive predominantly to left and right QPCs respectively. **b**, Reflectance  $S_{21}$  of the combined tank circuits as the QPCs are pinched off, showing separate resonances corresponding to left and right. **c** and **d**, QPC pinchoff measured simultaneously in reflectometry and DC conductance. **e**, Reflectometry signal for the right sensor measured as a function of  $V_L$  and  $V_R$ , showing steps corresponding to charge transitions. Electron configurations for each gate setting are indicated.

applied. The device was measured at 150 mK electron temperature in a dilution refrigerator equipped with an in-plane magnetic field.

A frequency-multiplexed radio-frequency (RF) reflectometry circuit [101, 102] was developed to allow both QPCs to be measured independently with MHz bandwidth (Fig. 4.3(a)). Parallel resonant tank circuits incorporating left and right QPCs were formed from proximal chip inductors  $L_L = 910$  nH and  $L_R = 750$  nH together with the parasitic capacitances  $C_L^P$  and  $C_R^P$  of the bond wires. Bias tees coupled to each tank circuit allowed the DC conductances  $g_L$ ,  $g_R$  of left and right QPCs to be measured simultaneously with the reflectance of the RF circuit. As each QPC was pinched off, a separate dip developed in the reflected signal at corresponding resonant frequency  $f_{L,R} \sim 1/2\pi\sqrt{L_{L,R}C_{L,R}^P}$  (Fig. 4.3(b)). To monitor the charge sensors, a carrier wave with components at  $f_L$  and  $f_R$  was injected into the refrigerator (Fig. 4.3(a)). After amplification both cryogenically and at room temperature, the reflected signal was demodulated by mixing with local oscillators to yield intermediate-frequency voltages  $RF_L$  and  $RF_R$  sensitive predominantly to  $g_L$  and  $g_R$  (Fig. 4.3(c) and (d)). To suppress backaction and reduce pulse coupling into the readout circuit, the RF carrier was blanked on both signal and return paths when not needed for readout.

Tuning  $g_R$  to the point of maximum charge sensitivity  $g_R \sim 0.4e^2/h$ , the configuration of the triple dot could be monitored via  $RF_R$  [102]. Sweeping voltages  $V_L$  and  $V_R$  on gates L and R, the charge stability diagram of the triple dot is mapped out as shown in Fig. 4.3(e)). Dark transition lines are seen to run with three different slopes, corresponding to changes of electron number in each of the three dots [96, 97]. For the most negative gate voltages, no more transitions are seen; this indicates that the device has been completely emptied, allowing absolute electron occupancies to be assigned to each region of the diagram.

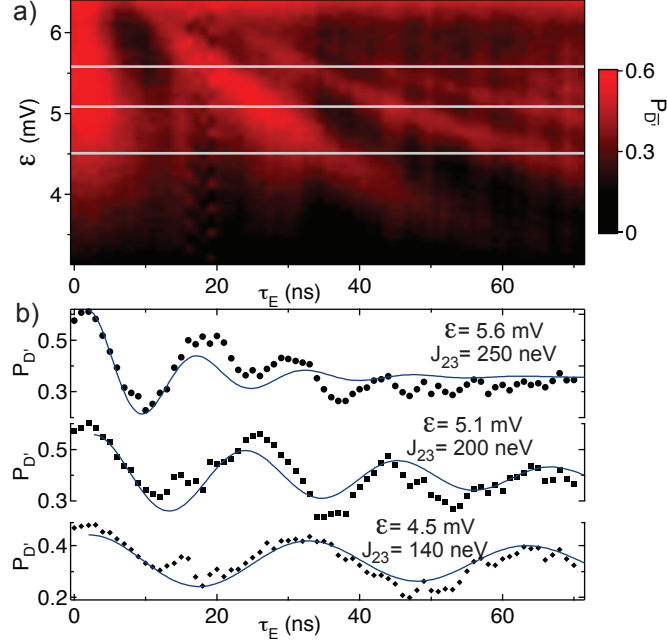


Figure 4.4: Coherent spin exchange **a**, Probability  $P_{\overline{D'}}$  to return to the initial  $|\overline{D'}_{S_z}\rangle$  state following an exchange pulse sequence, measured as a function of  $\epsilon$  during the exchange pulse and pulse duration  $\tau_E$ . Dark and bright regions respectively indicate odd and even numbers of complete spin exchanges. **b**, Points: Measured  $P_{\overline{D'}}$  as a function of  $\tau_E$  for values of  $\epsilon$  indicated by horizontal lines in **a**. Lines: Fits to exponentially damped phase-shifted cosines. The fitted exchange  $J_{23}(\epsilon)$  for each curve is shown.

#### 4.4 Coherent exchange in a triple dot

We demonstrate state preparation, coherent exchange, and readout using the following cycle of voltage pulses [40] applied to gates L and R to rapidly tune  $\epsilon$ . Beginning at  $\epsilon > \epsilon_+$  configures the device in (1,0,2) where tunneling to the leads initializes the qubit within the doublet  $|\overline{D'}_{S_z}\rangle$ . The detuning is then decreased to  $\epsilon \sim 0$  over 1  $\mu$ s, configuring the device in (1,1,1). Because this ramp time is adiabatic compared to the characteristic hyperfine interaction strength, it causes the spin system to enter a ground state defined by the random instantaneous configuration of the lattice nuclei, such as  $|\uparrow\downarrow\uparrow\rangle$  [40, 103]. Pulsing the detuning close to  $\epsilon_+$ , where  $J_{23}$  is large, for a time  $\tau_E$  leads to coherent exchange of spins between the right-hand dots. Finally, the detuning is ramped back to its original value  $\epsilon > \epsilon_+$ . The charge configuration is now determined by the outcome of the exchange pulse: Whereas the

hyperfine ground state reenters the  $|\overline{D}'_{S_z}\rangle$  doublet in the (1,0,2) configuration, a swapped state such as  $|\uparrow\uparrow\downarrow\rangle$  evolves into a superposition of  $|\overline{D}_{S_z}\rangle$  and  $|Q_{\pm 1/2}\rangle$  states, causing the device to remain in (1,1,1). At the end of this final ramp, the carrier is unblanked for readout of the charge sensor.

Averaged over many pulse cycles, the resulting voltage  $RF_R$  is converted to a spin state probability by calibrating it against the known values corresponding to (1,1,1) and (1,0,2) configurations. The probability  $P_{\overline{D}'}$  to return to the initial spin state is shown in Fig. 4.4(a) as a function of  $\tau_E$  and  $\epsilon$  during the exchange pulse. As a function of  $\tau_E$ ,  $P_{\overline{D}'}$  oscillates corresponding to coherent rotation between spin states, and as expected from Fig. 4.2(a), the oscillation frequency, set by  $J_{23}(\epsilon)$ , increases with  $\epsilon$ . The measured  $P_{\overline{D}'(\tau_E)}$  is fitted for three values of  $\epsilon$  with an exponentially damped cosine, corresponding to dephasing by electric fields with a white noise spectrum [40, 103]; the resulting values of  $J_{23}$  are shown in Fig. 4.4(b). The contrast of the oscillations, here taken as a fit parameter, is below unity; this can be qualitatively explained by pulse imperfections [41], which also cause the small phase shift observed.

## 4.5 Conclusion and acknowledgements

The exchange interaction is attractive for qubit control because it acts on ns timescales, can be tuned with gate voltage pulses, and does not rely on any particular property of the host material [40, 39]. The techniques demonstrated here to control and read out a three-spin system open the way to performing arbitrary qubit operations using this single physical interaction.

We acknowledge C. Barthel and D. J. Reilly for discussions.

## Chapter 5

# Towards a two-qubit gate in the singlet-triplet basis

This chapter presents an attempt to demonstrate a two-qubit gate in the singlet-triplet basis, mediated by capacitive coupling between a pair of double dots. By measuring the shift in the charge stability diagram of each double dot when the configuration of the other double dot changes, the coupling is estimated at  $\sim 60 \mu\text{eV}$ , large enough in principle for ns-timescale operations.

## 5.1 Introduction

Although many experiments on electron spins in semiconductor quantum dots have shown their potential as a quantum computer basis, no two-qubit operation has yet been demonstrated [9, 18, 40, 17]. In the simplest approach, with each qubit represented by a single spin [9], single-qubit operations are achieved by pulsed electron spin resonance and two-qubit operations using exchange between electrons in adjacent dots. Although both these elements have been demonstrated independently [40, 17], the separate technical demands they place on the qubit device have so far prevented their use in combination.

An alternative basis encodes each qubit using two electron spins in a double dot; the logical subspace is defined by the singlet  $S$  and  $m_s = 0$  triplet  $T$  states [38, 39]. The qubit can be initialized by preparing two spins in a single dot, where Pauli exclusion favors the singlet state; arbitrary single-qubit operations can be accomplished through the combination of controlled inter-dot exchange and magnetic field gradients [38, 39, 40]. For readout, the device is configured so that the two electrons occupy the same dot if they form a singlet but not if they form a triplet, so that the two states can be distinguished using a nearby charge sensor [27, 40, 19].

Proposed physical mechanisms for two-qubit operations in this basis include exchange and Coulomb interaction [38, 39], of which the latter is appealing because it keeps both qubits within the logical subspace [39]. To see how a logic operation can be carried out, consider the capacitively coupled pair of qubits shown in Figure 5.1(a). A tilt in the electrostatic potential of each double dot leads to a spin-dependent probability of double occupancy because singlet-state spatial wavefunctions can overlap in the same dot. The resulting spin-

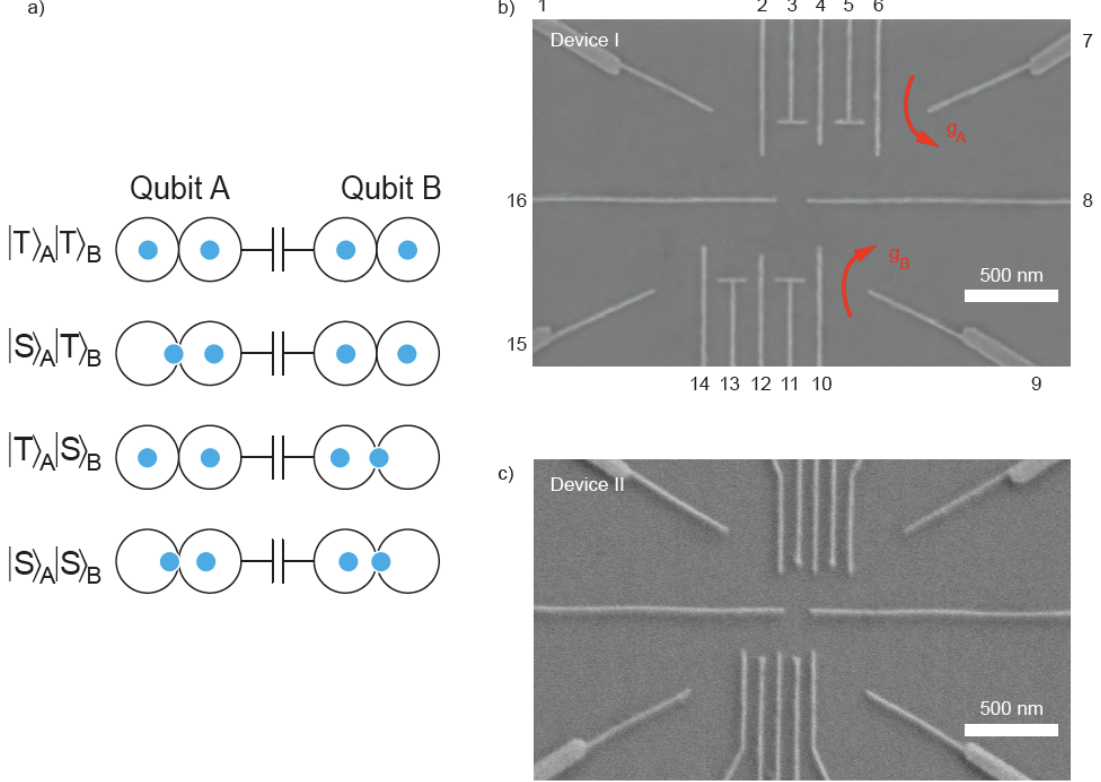


Figure 5.1: (a) Protocol for two-qubit coupling. Because the wavefunctions of two electrons can overlap only if they are in a singlet spin state, tilting the potential in a pair of double dots induces a spin-selective dipole-dipole coupling. This coupling mediates a controlled-phase gate between qubits [39]. (b) and (c) Two devices designed to demonstrate this interaction. Charge sensor conductances  $g_A$  and  $g_B$  are sensitive to the occupancies of upper and lower double dots respectively.

selective dipole-dipole interaction leads to a term in the effective Hamiltonian [39]:

$$H_{AB} = E_{cc} \sin^4 \theta |S\rangle_A |S\rangle_B \langle S|_A \langle S|_B, \quad (5.1)$$

where  $\sin^2 \theta$  is the probability of double occupancy for the singlet, and

$$E_{cc} \equiv U(0, 2, 2, 0) - U(1, 1, 2, 0) - (U(0, 2, 1, 1) - U(1, 1, 1, 1)) \quad (5.2)$$

is the differential cross-capacitance energy between the two double dots [39]. Here  $U(N_L^A, N_R^A, N_L^B, N_R^B)$

is the energy of the system with charge configuration  $(N_L^A, N_R^A)$  in double dot A and  $(N_L^B, N_R^B)$  in double dot B. If both qubits are in state  $S$ , their overall wavefunction acquires a phase  $\pi$  after a time  $\hbar\pi/E_{cc} \sin^4 \theta$ , thus executing a controlled-phase gate, which

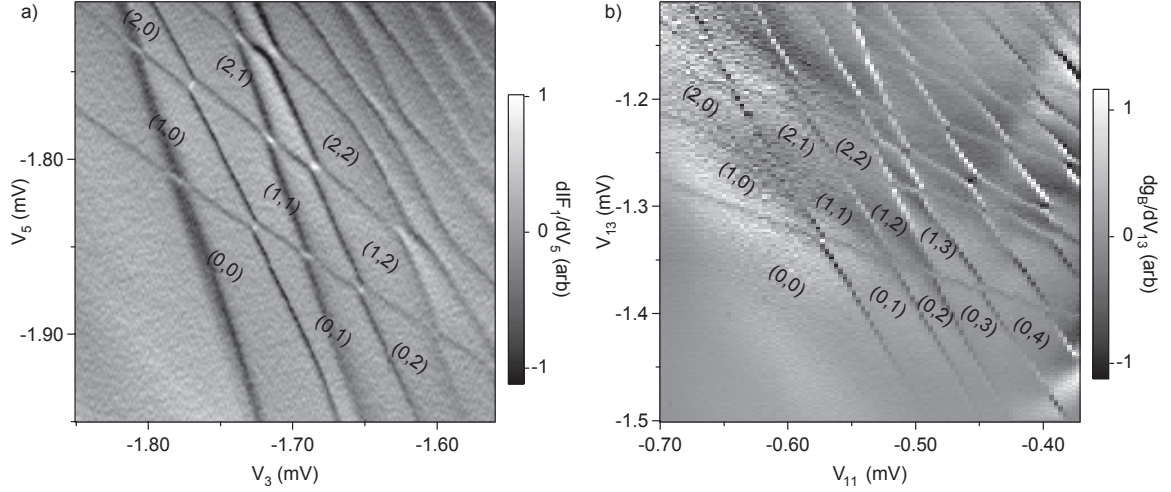


Figure 5.2: Charge stability diagrams of upper (a) and lower (b) double dots, measured using the charge sensors as a function of their respective plunger gate voltages. Both double dots can be tuned into the few-electron regime. The two broad near-vertical lines in (a) are resonances of the charge sensor.

is universal for quantum computation [13].

Previous work has measured the capacitive coupling between a pair of double dots [104, 105]. Recently, a pair of few-electron double quantum dots was realized, although it was not possible to measure the coupling in a charge configuration useful for qubit operation [106]. In this chapter I configure both double dots to the desired charge transitions and measure their coupling, finding that it is large enough in principle for rapid two-qubit gates.

## 5.2 Device and methods

To demonstrate two-qubit operation, we fabricated the devices shown in Figure 5.1. Depletion gates 1-16 defined a pair of double quantum dots and four charge sensing point contacts, two of which were measured by lock-in conductance measurements and frequency-multiplexed reflectometry. The conductance  $g_A$  of the upper sensor, also monitored via output voltage  $RF_1$  of the reflectometry circuit, was sensitive predominantly to the upper double dot; the conductance  $g_B$  of the lower sensor, monitored via reflectometry voltage

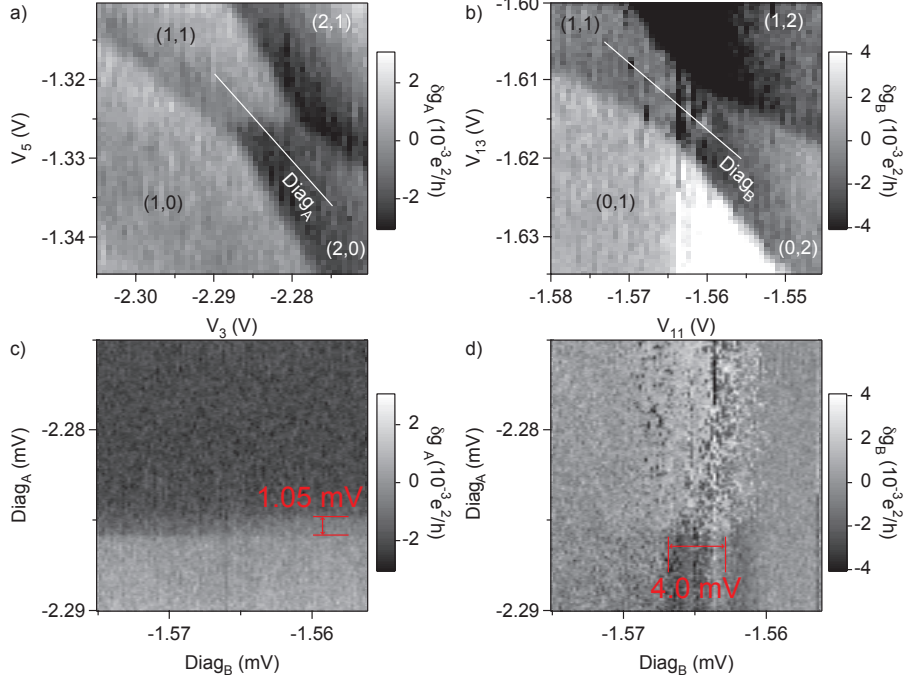


Figure 5.3: Measuring the electrostatic coupling between double dots. (a) and (b) Charge stability diagrams of upper and lower quantum dots around the charge transitions of interest. White lines define the detuning axes  $\text{Diag}_A$  and  $\text{Diag}_B$ . (c) and (d) The charge sensor conductances as a function of  $\text{Diag}_A$  and  $\text{Diag}_B$ . Shifts in the location of the charge transition allow measurement of the inter-qubit coupling.

$RF_2$ , was sensitive predominantly to the lower double dot.

Data presented in this chapter is measured entirely using Device I. The occupation states of upper and lower double dots were mapped out by monitoring the corresponding charge sensors as the plunger gates  $V_3$ ,  $V_5$ ,  $V_{11}$  and  $V_{13}$  were swept. As expected from the geometry of Figure 5.1,  $V_3$  and  $V_5$  primarily couple to the upper double dot whereas  $V_{11}$  and  $V_{13}$  couple to the lower double dot. The respective charge stability diagrams, presented in Figure 5.2, show that the device could be configured with only a few electrons in each dot.

### 5.3 Measuring the coupling

The dipole-dipole coupling was investigated with the device configured in the qubit regime, close to the degeneracy of (1,1) and (2,0) in the upper double dot and (1,1) and (0,2) in the lower double dot. Detailed charge stability diagrams in this regime are shown in Figure 5.3 (a) and (b). The coupling between double dots is investigated by measuring the shift of the stability diagram in one double dot when the other is swept through a charge transition [104, 105]. A pair of gate voltage detuning axes,  $\text{Diag}_A$  and  $\text{Diag}_B$ , were defined as shown in Figure 5.3 (a) and (b). Measuring the charge sensors as a function of both detunings, the location of the (1,1)-(2,0) transition in the upper double dot is seen to change around the value of  $\text{Diag}_B$  corresponding to the (1,1)-(0,2) transition in the lower double dot (Figure 5.3(c)). A corresponding shift in the location of the lower double dot transition is seen (less clearly) in (Figure 5.3(d)).

The magnitude of the shift in gate voltage is measured as  $1.1 \pm 0.2 \times 10^{-3}$  V in the upper double dot and  $4.0 \pm 2 \times 10^{-3}$  V in the lower dot. The constant of proportionality between gate voltage to energy is deduced separately for each double dot by measuring the shift of the charge transitions (not shown) when a known voltage bias is applied across the device [29]. When converted to an energy, the measured gate voltage shift corresponds to an energy  $E_{cc} = 60 \pm 15$   $\mu\text{eV}$  or  $E_{cc} = 90 \pm 50$   $\mu\text{eV}$ , measured from Figure 5.3(c) and Figure 5.3(d) respectively.

### 5.4 Summary and outlook

I have configured a pair of capacitively coupled double quantum dots in the few-electron regime, and measured the coupling at an occupancy of interest for qubit operation. The

measured coupling is in principle sufficient for ns-timescale two-qubit operations [39].

Attempts to actually realize a pair of qubits in Device I proved unsuccessful, and several variations to the design produced no improvement. The most common failure mode was for each double dot to break up into three or more dots as the electron number was reduced. (Incipient breakup can be seen in Figure 5.2(c), where adjacent charge transition lines have different slopes.) Another common problem was very low tunnel rates between quantum dots and to the leads, whereas fairly rapid tunneling is needed for qubit initialization and inter-dot exchange. What prevented qubit operation in Device I was a lack of spin blockade, making readout impossible.

Apart from the larger number of elements that must work together in a four-dot rather than a two-dot device, I hypothesize that the common difficulty is the longitudinal arrangement of quantum dots. In contrast to devices shown in previous chapters, the tunnel barriers in Figure 5.1 are located on opposite sides of each quantum dot. In order to be tunnel-coupled to both sides, each dot must take on an elongated shape, prone to being broken up by disorder. The elongated shape also leads to a low intra-dot exchange [107] and therefore inhibits spin blockade.

In an attempt to circumvent this problem, much smaller devices were fabricated, including Device II (Figure 5.1(c)). The upper part of this device was fairly easy configured as a few-electron double dot; however, the lower part of the device could not be properly configured as a double dot at all, presumably because of disorder. The difficulty of realizing two qubits in the same device illustrates the severe design and materials challenges involved in scaling a spin-based quantum computer.

# Appendix A

## Fabrication recipe

### A.1 Introduction

Most of the fabrication techniques for the devices described in this thesis are well-established in the Marcus group [21, 108, 109, 110], although incremental improvements have been made during my time in the group. In this Appendix I summarize my recipe and key parameters. Over several runs my lithographic yield has averaged over 70% even for complex multi-dot devices.

### A.2 Generic photolithography recipe

- Sonicate for 5 min in trichloroethylene, acetone and isopropanol.
- Bake for 5 min at 200 °C.
- Spin Shipley S1813 resist for 60 s at 4000 rpm.
- Bake for 2 min at 115 °C.
- Expose corner bead removal pattern for 40 s in AB-M mask aligner
- Develop for 15 s in CD-26 developer, rinse in water.

- Expose main pattern for 4 s in AB-M mask aligner, making sure to press chip firmly against mask.
- Develop for 60 s in CD-26 developer, rinse in water.

### A.3 Complete fabrication procedure

#### A.3.1 Mesa etch

- Define mesa pattern photolithographically as described above, omitting corner bead removal.
- Etch chip in a solution of 1:8:240 H<sub>2</sub>O: H<sub>2</sub>O<sub>2</sub>: H<sub>2</sub>SO<sub>4</sub> to a depth 20 nm below the 2DEG (A typical etch rate is 8 nm/s.)

#### A.3.2 Ohmic contacts

- Define ohmic pattern photolithographically as described above.
- Oxygen plasma clean in Technics 220 series micro-stripper at 160 mT pressure and 60 W power for 60 s.
- Dip in 10 % ammonium hydroxide solution for 5 s.
- Evaporate in Sharon electron beam evaporator
  - 50 Å Pt at 1.0 Å/s
  - 1200 Å Au at 3.0 Å/s
  - 800 Å Ge at 2.0 Å/s
  - 500 Å Pt at 1.5 Å/s
  - 500 Å Au at 3.0 Å/s.

- Liftoff in acetone.
- Anneal for 100 s at 510 °C.

### A.3.3 Gate pads

- Define gate pad pattern photolithographically as described above.
- Oxygen plasma clean in Technics 220 series micro-stripper at 160 mT pressure and 60 W power for 60 s.
- Evaporate in Sharon thermal evaporator
  - 250 Å Ti at 1.0 Å/s
  - 1200 Å Au at 3.0 Å/s.
- Liftoff in acetone.

### A.3.4 Fine gates

- Sonicate chip for 5 min in trichloroethylene, acetone and isopropanol
- Bake for 2 min at 170 °C.
- Spin 950 PMMA A4 for 60 s at 4000 rpm.
- Bake for 15 min at 170 °C.
- Expose fine features using 10  $\mu\text{m}$  aperture at 6 nm step size. Set area dose to 900  $\mu\text{As}/\text{cm}^2$ , line dose to 2700  $\text{pAs}/\text{cm}$ . If possible design your finest features as single-pixel lines.
- Expose connector features using 120  $\mu\text{m}$  aperture at 56 nm step size. Set area dose to 1080  $\mu\text{As}/\text{cm}^2$ .

- Develop for 60 s in a solution of 1:3 methyl isobutyl ketone: isopropanol cooled to 0 °C, rinse in isopropanol.
- Evaporate in Sharon thermal evaporator  
50 Å Ti at 0.5 Å/s  
150 Å Au at 1.0 Å/s.
- Liftoff in acetone.

## Appendix B

# Constructing and using a multiplexed reflectometry setup

This Appendix describes the fast readout system I created and used for the measurements described in Chapters 4 and 5. As well as details of the hardware, I explain how to use the setup efficiently. The Appendix has four sections. Sections B.1 and B.2 describe the hardware inside and outside the cryostat respectively. Section B.3 describes the code I adapted to take data fast. Section B.4 describes the tuning process.

### B.1 Hardware inside the cryostat

The fast readout system I constructed, based on an Oxford Instruments Kelvinox 100 dilution refrigerator, was partly copied from the one built by David Reilly [102]. I extended Reilly's design to allow for multiplexed readout, more pulse lines and heat sinking, and easier sample exchange. Photographs and schematics of the modified cryostat are shown in Figures B.1 and B.2.

The design must fulfill two opposing criteria: good electrical access to the device, without unacceptable heat load. This must be achieved for three separate types of connection to the device:  $\sim 25$  dc wires, with bandwidth up to  $\sim 20$  kHz; four pulse lines, with bandwidth up to  $\sim 10$  GHz; and a multiplexed reflectometry line, operating at frequencies

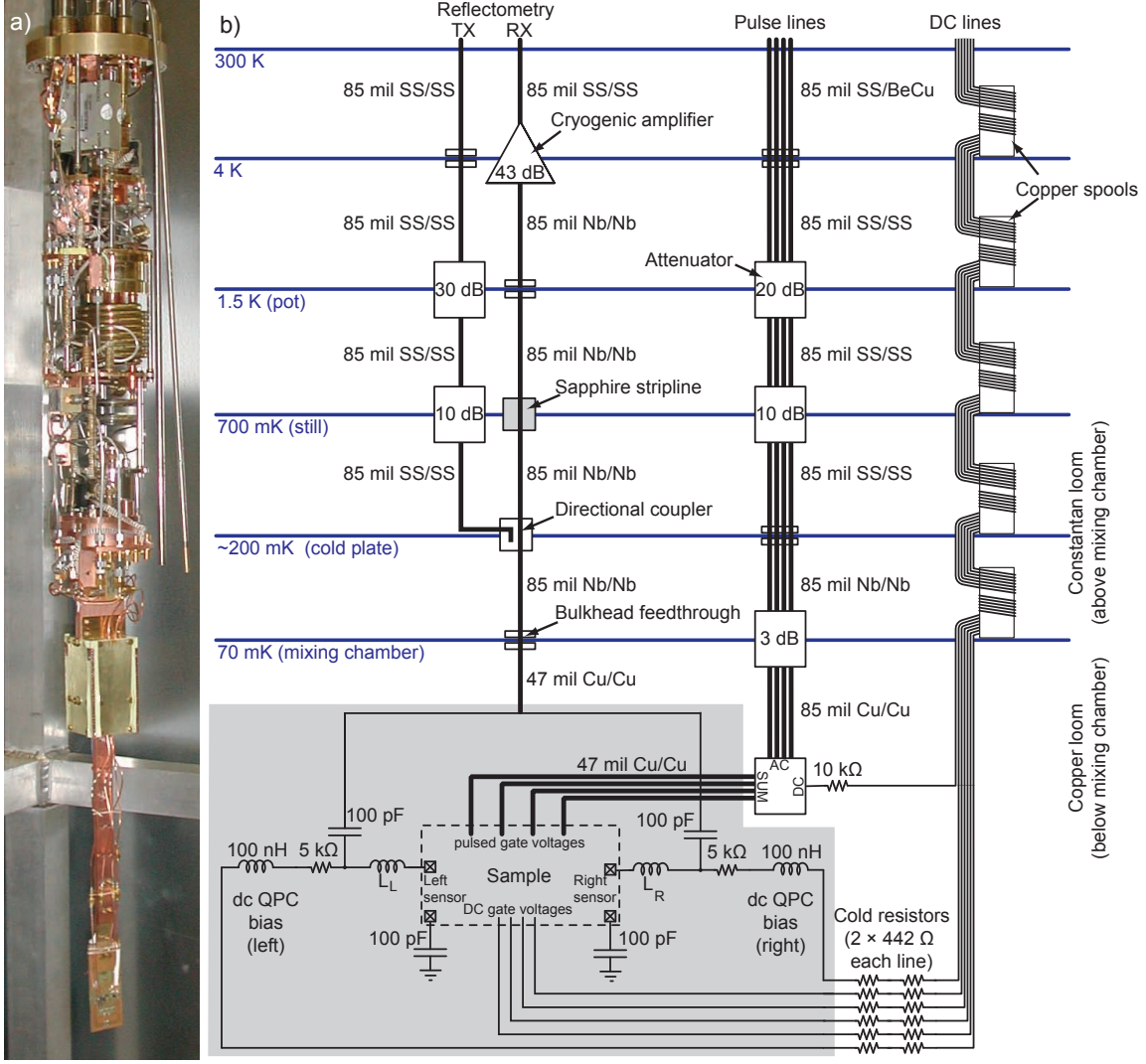


Figure B.1: Dilution refrigerator equipped with radio-frequency reflectometry setup. (a) Photograph of the cryostat. (b) Schematic of the electronics inside the cryostat. The grey background indicates components mounted on the PC board. Key components are: Cryogenic amplifier: Quinstar QCA-U230, custom-built; Sapphire stripline: Home-built [111]; Directional coupler: Mini-circuits ZEDC-15-2B; Bias tees: Anritsu K251.

$\sim 190 - 250$  MHz.

For the DC wiring, long ( $\sim 3$  m) sections of constantan loom are used with a total resistance  $\sim 200 \Omega$  from room temperature to the mixing chamber. At each stage of the fridge, the loom is wound around one or more copper spools, and between stages a generous amount of slack is left to minimize the heat load down the fridge. Below the mixing chamber, copper loom is used to maximize cooling of the sample. As a final stage of filtering, two

banks of resistors are fitted tightly into brass plates at the cold finger and fixed with Stycast.

For the high-frequency wiring, it is necessary to use semi-rigid coaxial cable. The potential for large heat loads is here much greater, because the cables can transmit black-body microwave radiation down the fridge, and because the inner conductor is quite poorly thermalized through the dielectric. Increasing the cable length does reduce the heat load, but also creates frequency-dependent attenuation that is undesirable for pulse-gate experiments. Instead, we rely mainly on broadband attenuators mounted at each refrigerator stage. To allow gate voltage offsets to be applied without ohmic heating, DC connections are made through bias tees mounted at the final cooling stage.

The choice of diameter and material for the coaxial cables was determined by the length of each coax segment and the temperature and cooling power at each refrigerator stage. Over most of the length of the fridge, .085" diameter stainless steel (SS) coax was used because it combines comparatively weak attenuation with low thermal conductivity. From the top of the fridge to the pot, coax with BeCu inner conductor was used to reduce attenuation over the longest length of cable, and because the pot has enough cooling power to handle the extra heat load. From the cold plate to the mixing chamber superconducting Nb coax is used to take advantage of its lower thermal conductivity (below  $\sim 90$  mK) and weaker attenuation [112]. Below the last set of attenuators, thermal conductivity is no longer an issue, and copper is used for its low attenuation, with 47 mil diameter cable chosen to save space in the cold finger. Over the whole length of the fridge, the attenuation of the pulse lines is found to increase smoothly with frequency up to at least 6 GHz, with roll-off  $\sim 5\text{dB}/\sqrt{\text{GHz}}$  at room temperature.

Wiring the reflectometry lines is in some ways easier because the highest operating frequency is much lower (although definitely high enough to require semi-rigid coax). How-

ever, attenuators cannot be used on the measurement path because the signal would also be reduced. The solution that Reilly developed was to heat sink the signal path at the still with a sapphire stripline and at the cold plate through the directional coupler (which acts as a short to ground at DC). At other refrigerator stages, the outer conductor was thermalized using bulkheads. Coaxial segments in both reflectometry and pulse lines were heavily looped<sup>1</sup> to increase the cable length and thermal load between stages by a factor  $\sim 2$ .

My cold finger is shown in Figure B.2, and is fairly similar to previous Marcuslab designs [20]. The design was made easier by Jason Petta's earlier expansion of the cryostat's inner vacuum chamber. The main novel feature is the  $1/4" \times 1/2"$  copper spine brazed to the top plate of the cold finger and running down to the sample holder. This provides good thermal contact down the center and allows various heat sinking elements (bias tees, bulkheads and resistor plates) to be mounted accessibly on the outside of the cold finger.

The PC board sample holder (Figure B.2(c)) follows Reilly's design. Connection to the fridge wiring is through a Cristek connector for the DC wiring and through SMM connectors for the coaxial cables. With the exception of the reflectometry connection, which is via a microwave launcher, all cables are soldered directly to the PC board. Strain relief for the dc wires is provided by a drop of Stycast on the back of the board (although Ferdinand reckons dental floss is preferable).

---

<sup>1</sup>It has since become fashionable to make coax segments as short as possible, for the following reason. For a normal-metal coax of length  $L$ , the frequency-dependent attenuation  $\alpha$  is proportional to  $\sqrt{\rho}L/D$ , where  $\rho$  is its resistivity and  $D$  is the diameter [113]. By the Wiedemann-Franz law, the thermal conductance due to the conduction electrons is  $\Theta \propto D^2/\rho L \propto L/\alpha^2$ . So for given attenuation, the heat load is minimized by using a short length of thin, high-resistance coax. Of course, coax is available in only a few discrete diameters, so ideal parameters are often not realizable in practice.

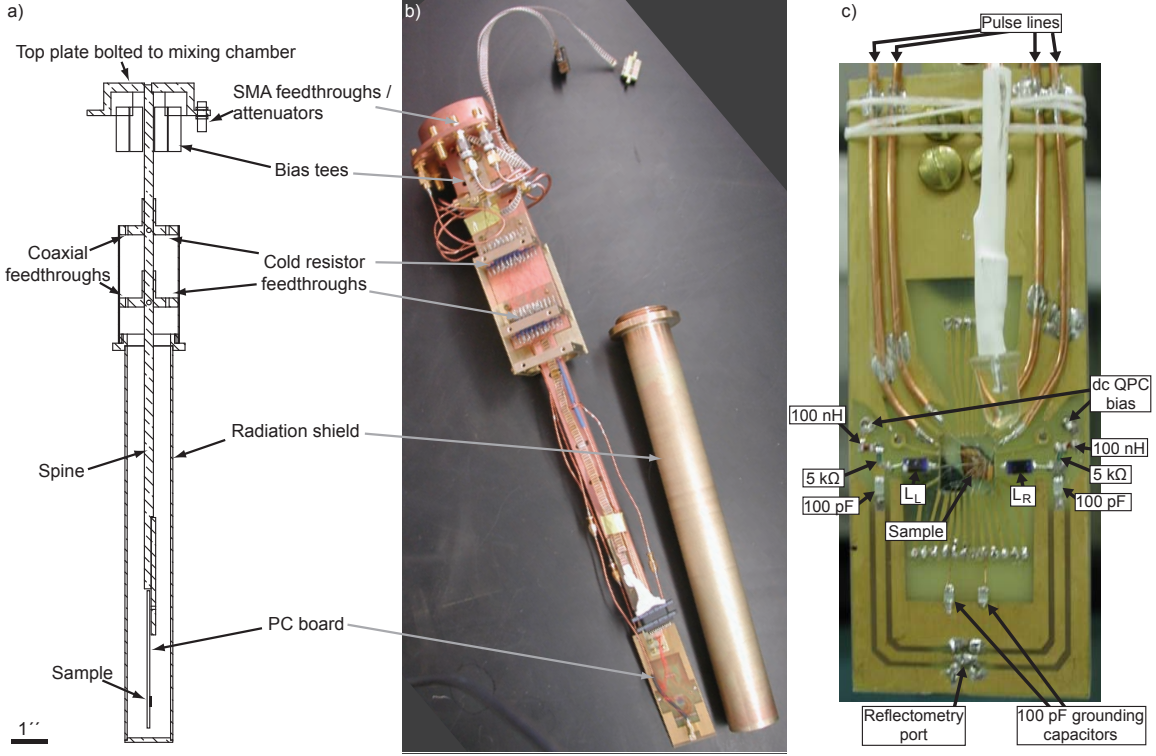


Figure B.2: Cold finger and sample board. (a) Cross-section of cold finger, showing key components. The structure is entirely of brass except for the top plate and spine, which are of copper. The feedthroughs and radiation shield are designed to provide an almost completely sealed sample space. (b) Photograph of cold finger. To show the structure more clearly, two out of four brass plates screening the feedthroughs have been removed and the main radiation shield has been unscrewed. (c) PC board holding sample. Key components are indicated, including the electronic components making up the QPC bias tee and the tank circuit inductors  $L_L$  and  $L_R$ . An LED allowed illumination of the cold sample but this was never found to have a beneficial effect.

## B.2 Hardware outside the cryostat

The experimental configuration must allow for quasistatic and pulsed gate voltages to be applied to the device, and for three kinds of measurement: Lock-in and reflectometry measurements of the charge sensors, and dc transport measurements of the dots. A simplified version of the setup is shown in Figure B.3. Quasistatic gate voltages are supplied by a 20-channel digital-to-analog converter (DecaDAC) from the Harvard Physics electronics shop supplemented by a battery box. For a few channels, a divider/adder allows rapid ramping of the gate voltage with an HP33210A function generator. Gate pulses are provided by a

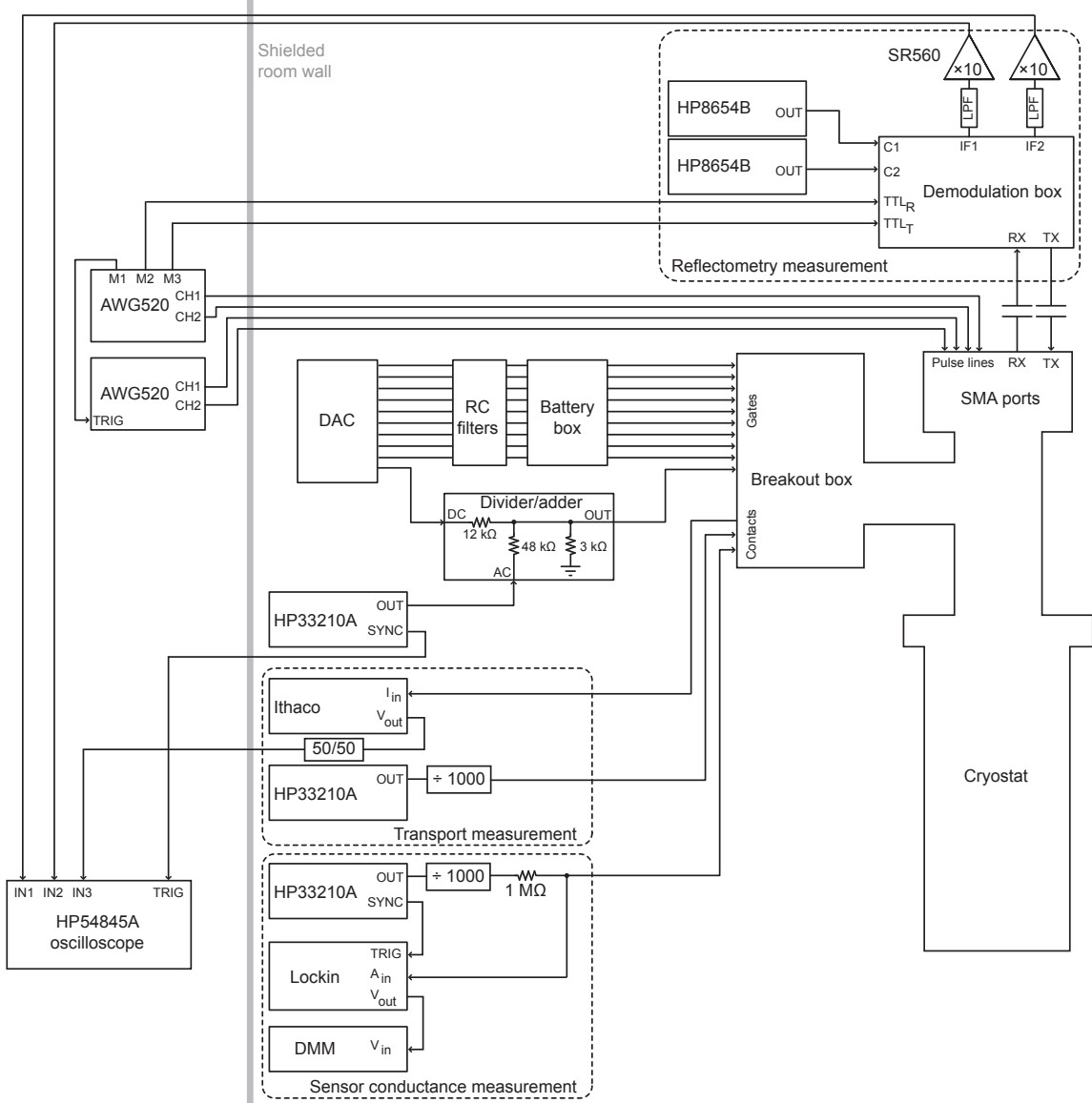


Figure B.3: Schematic of the room temperature measurement setup. For a description, see the text.

pair of Tektronix AWG520s ganged together (see Appendix C).

The usual purpose of the lock-in measurement is to ensure that the charge sensor is tuned for optimum sensitivity, usually corresponding to a conductance around  $0.4e^2/h$ . The conductance is measured using a 1 nA current bias at of 137 Hz and digitized via a DMM at  $\sim 10$  Hz. The bias, supplied by an HP33210A, is blanked during reflectometry measurements.

For reflectometry, carrier signals generated by a pair of HP8654Bs are fed into the fridge. The returned signal is mixed with the carriers inside a home-built demodulation box (see Section B.2.1), generating two IF voltages which are filtered, amplified and finally digitized using an oscilloscope. Low-frequency ground loops are suppressed with inside/outside DC blocks (Midwest Microwave DCB-3537-IO-SMA-02) on Rx and Tx lines.

Transport measurement of the dots is performed in voltage bias using a DC excitation<sup>2</sup> of  $\sim 100\mu\text{V}$ . The current is detected using an Ithaco 1211 current amplifier set to its highest bandwidth, with its output again digitized using an HP54845A oscilloscope. A ground loop between Ithaco and oscilloscope is suppressed by  $50\ \Omega$  resistors on inner and outer conductors of the connecting BNC cable.

To map reflectometry and charge sensing signals to gate voltages, the oscilloscope is triggered from the synchronization signal of the HP33210 that ramps the gate. Typically the gate is ramped at 47 Hz in a sawtooth pattern, and the oscilloscope averages 16 ramps to generate each slice of data.

### B.2.1 The demodulation box

The demodulation box is shown in Figure B.4. Carrier signals supplied through ports C1 and C2 are combined and transmitted to the fridge via an optional RF switch for blanking. The signal from the fridge is amplified, fed through a second switch, and then mixed with the carriers to generate voltages IF1 and IF2. Voltages PS1 and PS2 tune the relative phase

---

<sup>2</sup>Supplying the DC bias with a function generator, as shown in Figure B.3, is presumably unnecessary. The reason for this extravagance is historical; until last year the usual method to measure transport was with a lock-in amplifier. I have found that measuring with the scope is just as useful and much faster, but I never got round to replacing the HP33210A by a DAC channel.

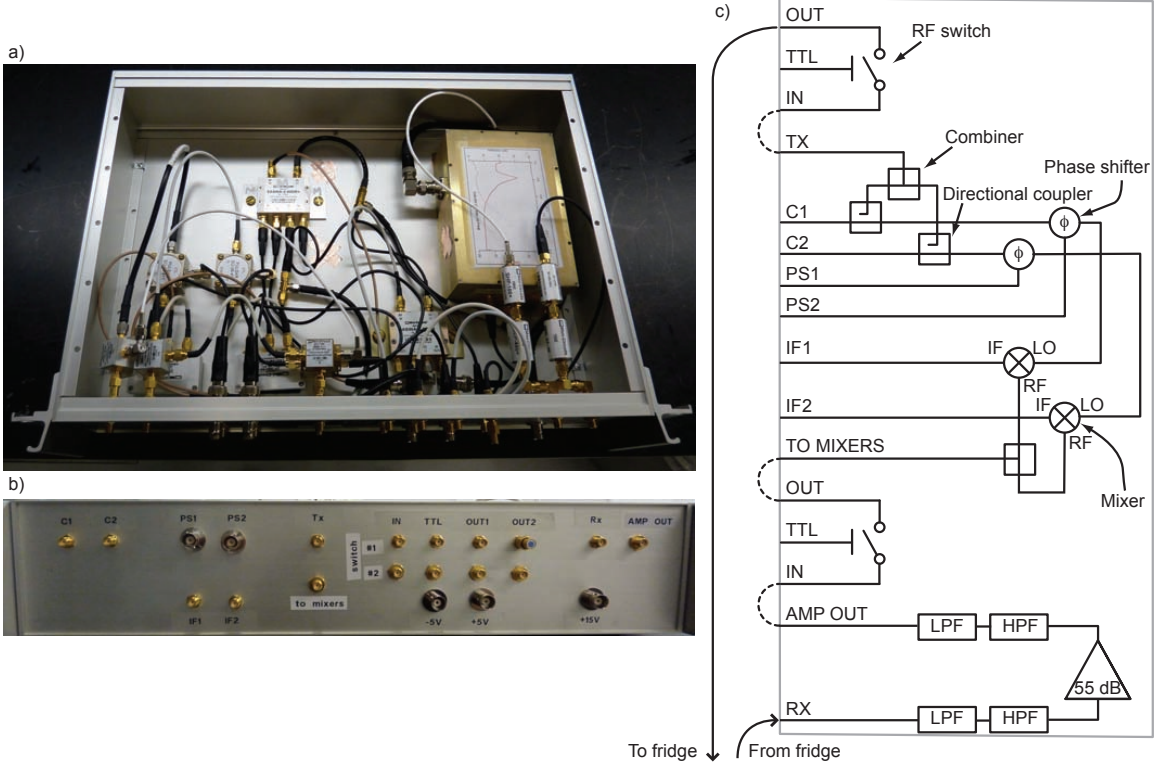


Figure B.4: Room temperature demodulation box. (a) and (b) Top and front view (cover removed). (c) Circuit diagram. Dashed lines denote cabling outside the box that allows input and output signals to be fed into optional blanking switches. Power wiring for switches and amplifier (BNC connectors labelled  $\pm 5$  V and 15 V in (b)) is not shown. Components are: RF switch: Mini-circuits ZASWA-2-50DR+; Combiner/splitter: Mini-circuits ZESC-2-11; Directional coupler: ZEDC-15-2B; Phase shifter: Pulsar SO-06-411; Mixer: Mini-circuits ZP-3MH; Filters: Mini-circuits ZHP-100 and ZLP-450.

between LO and RF inputs; these are set by hand to maximize IF1 and IF2. For tidiness and shielding, the entire setup is assembled inside a Lansing aluminum enclosure.

### B.3 Igor code

Data acquisition was performed using Wavemetrics' Igor Pro, which as usual was more than up to the task. The main acquisition code I based on Alex Johnson's library of routines [20] and modified in a fairly obvious way to acquire data from the oscilloscope as well as from DMMs. A few supplementary tasks need to be performed before each scan, including

optimizing the charge sensor conductance and setting the gate voltage ramp appropriately.

To carry these out efficiently and automatically, I wrote the function `do2dfast()`. The functions `tuneg()` and `calsensor()`, which automatically optimize the sensor conductance, are also given below. The functions `WC_stream()`, `WC_QPCname()` and `WC_idloc()` are not given here; they are look-up functions for which sensor associates with which swept gate and are on the MarcusLab Wiki<sup>3</sup>.

### B.3.1 do2dfast()

```

function do2dfast(idstr1,start1,stop1,numdivs1,delay1,idstr2, start2,stop2)
    //Function to do fast 2D sweeps
    string idstr1          // id of outer loop (a code for the variable scanned - see description
                           // of Alex Johnson's code in his thesis)
    variable start1         // outer loop starting value
    variable stop1          // ending value
    variable numdivs1       // number of points minus 1
    variable delay1         // seconds of delay between sweeps
    string idstr2          // same for inner loop
    variable start2,stop2

    variable hpnum=hpfromidstr(idstr2)                      // Address of function generator on gate
    variable QPCstimulus=3                                    // Address of function generator for QPC bias
    variable calsteps=3                                      // Number of QPC calibration steps

    // Begin by calibrating the charge sensor
    setval(idstr2,(start2+stop2)/2)                         // Make sure we're not ramping the gate ...
    setfuncHP(hpnum,"DC")                                     // ... and that the lock-in excitation is unblanked.
    setfuncHP(QPCstimulus,"SIN")
    wait(1)
    strswitch(idstr1)
        case "b":                                         // Scan parameters other than gates.
        case "ts":
        case "te":
            tuneg(WC_stream(idstr1), WC_QPCname(idstr1)) // Stepping these variables barely changes
                                                               // the sensor conductance, so we need only optimize it once.
        default:
            if (WC_idloc(idstr1)>=0)                      // If the stepped parameter is a gate, we must optimize the
                                                               // sensor across the full range of the scan.
                calsensor(idstr1,start1,stop1,calsteps-1)    // Optimize the charge sensor across the swept range.
            else
                print "do2dfast(): idstr1 not recognized"
            endif
    endswitch

    setfuncHP(QPCstimulus,"DC")                      // Blank the lock-in excitation.
    oscilforwallwall()                            // Set up oscilloscope.
    if (start2<stop2)
        setfuncHP(hpnum,"RAMPUP")                  // Start ramping the gate.
        osciltrigslope(1)
    else
        setfuncHP(hpnum,"RAMPDOWN")

```

---

<sup>3</sup><https://qhall.fas.harvard.edu>

```

        osciltrigslope(0)
    endif
    setval("vac"+num2str(hpnum),abs(start2-stop2)*1000)      // Set gate ramp amplitude.
    wait(2)

    //The next seven lines handle bookkeeping for do2d() so the wave ends up displaying correctly.
    variable channum
    sscanf idstr2, "c%g", channum
    if ((channum>0)|!stringmatch(idstr2,"c0"))
        idstr2="f"+idstr2
    else
        idstr2="nscope"
    endif

    do2d(idstri,start1,stop1,numdivs1,delay1,idstr2, start2,stop2,0,0)
    setfuncHP(hpnum,"DC")                                // Stop ramping the gate.
    setfuncHP(QPCstimulus,"SIN")                         // Unblank lock-in excitation.
end

```

### B.3.2 tuneg()

```

function tuneg(stream,idstr)
    // Optimizes QPC conductance for charge sensing by tuning a nearby gate.
    // Two simple search algorithms for the optimal point are applied. The first algorithm measures the
    // conductance and adjusts the gate by an amount proportional to the mismatch from the target value. It
    // repeats until the conductance gets close to the ideal value or a counter is exceeded.
    // After the first algorithm completes, the second algorithm fine-tunes the conductance by scanning once in
    // and then out with the gate until the target value is passed.
    string idstr           // QPC gate
    variable stream         // Acquisition stream for QPC conductance (see Alex's thesis for details)

    variable /G targetcon                         // Optimal conductance value to aim for.

    variable target=targetcon
    variable toplimit=400                          // Limits within gate voltage can safely be swept (in mV).
    variable bottomlimit=-1950
    variable waittime=0.1                          // Settling time after changing gate (in s).

    wave DAC=DAC
    variable QPCnum
    sscanf idstr, "c%g", QPCnum
    if (numtype(getdata(stream))||numtype(QPCnum)) // Input checking.
        printf "tuneg(): Invalid number %g %g", stream, QPCnum
        AbortOnValue 1, 1
        return -1
    endif
    variable returnval

    setval(idstr, max(bottomlimit, min(toplimit, DAC[QPCnum])))
    // Make sure we start off in the allowed range .
    wait(4*waittime)

    // Run the first search algorithm
    variable maxstep=20, minstep=0.1                // mV
    variable gradient=0.2                          // How much to change gate voltage for a given conductance
    // mismatch. The best value depends on how steep the QPC pinchoff is. Too large, and the search
    // is slow; too small, and iteration may not converge.
    variable counter=200                           //Maximum number of iterations.
    do
        wait(2*waittime)
        variable stepsize=-(getdata(stream)-target)/gradient
        if (stepsize < 0)
            stepsize=-max(min(-stepsize,maxstep),minstep)
        else
            stepsize=max(min(stepsize,maxstep),minstep)
        endif

```

```

        if (((DAC[QPCnum]+stepsize)>bottomlimit)&&((DAC[QPCnum]+stepsize)<toplimate))
            returnval = setval(idstr, DAC[QPCnum]+stepsize)
            if (((returnval == -1)&&(stepsize<0))||((returnval==2)&&(stepsize>0)))
                printf "tuneg() part 1: Exceeded limit, %g %g", stepsize, returnval
                counter=0
            endif
        endif
        doupdate
        counter=1
    while ((abs(stepsize)>minstep)&&(counter>0))

        wait(2*waittime)

        // Run the second search algorithm
        variable downstep=2, upstep=0.3                                //mV
        do
            returnval = setval(idstr, DAC[QPCnum]-downstep)           //Go down until conductance is below target.
            if (returnval==2)
                printf "tuneg() crawl down: Exceeded limit, %g %g", downstep, returnval
                return NaN
            endif
            doupdate
            wait(2*waittime)
        while((DAC[QPCnum]-downstep>bottomlimit)&&(getdata(stream)>target))
        if (DAC[QPCnum]-downstep<=bottomlimit)
            print "tuneg():hit bottomlimit"
            AbortOnValue 1, -2
        endif
        do
            returnval = setval(idstr, DAC[QPCnum]+upstep)           //Now go up until conductance is above target.
            if (returnval==2)
                printf "tuneg() crawl up: Exceeded limit, %g %g", upstep, returnval
                return NaN
            endif
            doupdate
            wait(waittime)
        while((DAC[QPCnum]+upstep<toplimate)&&(getdata(stream)<target))
        if (DAC[QPCnum]+upstep>toplimate)
            print "tuneg():hit toplimate"
            AbortOnValue 1, -3
        endif
        return DAC[QPCnum]
    end

```

### B.3.3 calsensor()

```

function calsensor(idstr,start,stop,numdivs)
    // Over a range of values of gate idstr, find the optimal QPC gate settings, and fit those settings with a
    // parabola to allow optimized sensing across the entire range.
    string idstr           // Gate voltage to be swept
    variable start, stop, numdivs // Sweep range, and number of points to tune QPC at.

    newdatafolder /0 root:util:calsensor
    wave wKK0 = root:util:calsensor:KK0                                // These waves store estimates (derived from previous runs
    wave wKK1 = root:util:calsensor:KK1                                // of this function) for the parabola fit coefficients.
    wave wKK2 = root:util:calsensor:KK2

    variable KK0=wKK0[WC_idloc(idstr)]
    variable KK1=wKK1[WC_idloc(idstr)]
    variable KK2=wKK2[WC_idloc(idstr)]

    // If no valid estimates for the fit parameters are found, then guess.
    if (numtype(KK0))
        KK0=-1000
    endif

```

```

if (numtype(KK1))
    KK1=0
endif
if (numtype(KK2))
    KK2=0
endif

strswitch (idstr)                                // Look up the QPC gate and data stream associated with
                                                // gate idstr.

    default:
        if (WC_idloc(idstr)>=0)
            string QPCstr=WC_QPCname(idstr)
            variable stream=WC_stream(idstr)
        else
            print "calsensor(): wall not recognized."
            return 0
        endif
    endswitch

//Make waves to store the gate settings in.
make /O /N=(numdivs+1) calx=start+(stop-start)/numdivs * p
duplicate /o calx caly
caly=NaN

// Now search for the optimal QPC setting at each point.
variable i
for (i=0; i<=numdivs; i+=1)
    setval(idstr,calx[i])
    try
        variable tunegreturn=tuneg(stream,QPCstr)
    catch
        if (V_Abortcode==1)
            abort
        endif
        if ((V_Abortcode == -2) || (V_Abortcode == -3))
            tunegreturn=NaN
        endif
    endtry
    caly[i]=min(tunegreturn,400)
    wKK0[WC_idloc(idstr)]+=caly[i]-(KK0 + KK1 * calx[i] + KK2 * calx[i]^2) // Set the offset for the
                                                // next point based on this point. This usually speeds up
                                                // the next search.
endfor

CurveFit /Q /NTHR=0 poly 3, caly /X=calx /D      //Fit the parabola.

wKK0[WC_idloc(idstr)]=K0                         //Store the results.
wKK1[WC_idloc(idstr)]=K1
wKK2[WC_idloc(idstr)]=K2
end

```

## B.4 Tuning hints

Here are outline instructions for tuning up a double-double device with a gate layout similar to that shown in Figure 5.1(a).

Good tuning starts with appropriate positive bias during cooldown. If you've successfully tuned up your device (or a similar one) before, pick the same positive bias. If it's

a new design, I suggest cooling with 200-300 mV on all gates. If previous tuneups with the same device were unsuccessful, try to modify the potential landscape by adjusting the cooldown bias on individual gates; as a general rule, more positive bias leads to a bigger gate footprint once the dot is formed. Although  $\sim 300$  mV of cooldown bias seems to be optimal for device stability, you can go at least 300 mV in either direction without much trouble.

Once you're cold, establish what voltage on gates 8 and 16 is needed to pinch off the center of the device. Measuring the conductance between top and bottom sets of ohmic contacts, and with all other gates grounded, do a two-dimensional scan of  $V_8$  and  $V_{16}$ . With luck, you will get smooth pinchoff down to zero. Where this happens, you can guarantee that the two pairs are separated. Usually I repeat the scan with the other gates all depleted (say at -500 mV), to get an idea of how much they help to pinch off the center.

Next, try to form dots in the top and bottom pairs. Set up transport measurements through each pair, and deplete gates 3-5 and 11-13. Over a range of  $V_8$  and  $V_{16}$  values sufficient to pinch off the center, do 2-D scans ('wall-walls') of  $V_2$  and  $V_6$ , and of  $V_{10}$  and  $V_{14}$ . Try to find a value of  $V_8$  and  $V_{16}$  where Coulomb blockade lines appear in both upper and lower pairs.

Having found Coulomb blockade, try to establish clear double-dot behavior, manifested by Coulomb blockade lines forming a honeycomb in the wall-walls. In a good device, the most likely scenario is for each pair of dots to be merged initially, so you will need to decrease  $V_4$  and  $V_{12}$  to separate them. Quite often, it will happen that one dot of a pair will be too open to show Coulomb blockade or too isolated from its partner to make a honeycomb. In these cases, you will have to adjust  $V_3 - V_5$  and  $V_{11} - V_{13}$  to try to create space for your dots in favorable locations. You will find that tuning one pair messes up the tuning in the

other; to make both work, switch between them every few hours until you end up with both tuned at the same time.

Assuming you are successful, set  $V_2$ ,  $V_6$ ,  $V_{10}$ , and  $V_{14}$  to values in the honeycomb regions of the wall-wall, and switch to sweeping plunger gates 3, 5, 11 and 13. Once you have verified that you can also see honeycombs sweeping these gates, set up reflectometry measurements. Use a network analyzer to find the resonances of your tank circuits, and set the carrier frequencies to match them. You are now ready to hunt down the last electrons in each dot. Do 2-D scans sweeping  $V_3$  and  $V_5$ , then  $V_{11}$  and  $V_{13}$ , going to more negative values until no more charge sensing transitions appear. This can be a sign that the device is empty, but more likely it means the dots are latching - becoming to pinched off for electrons to leave. A strong indication of latching is charge sensing lines that distort or fade away in the lower left of the gate voltage plane. the best way to prevent it is usually to pull back with the wall voltages.

Eventually you should be able to measure a clear stability diagram similar to Figure 1.3 in each pair, showing a series of well-defined charge transitions down to the last electron. Now you want to open the dots up to the leads until a measurable current ( $\sim 1$  pA at  $\sim 200$   $\mu$ V) is found at the (1,1)-(0,2) (or (0,2)-(1,1)) transitions. Usually this means pulling back with  $V_2$ ,  $V_6$ ,  $V_{10}$  and  $V_{14}$  (and possibly  $V_8$  and  $V_{16}$  as well). Once you are close, charge sensing can help you work out which of the three tunnel barriers in each pair of dots limits the current: In a plot such as Figure 1.4(e), the charge sensing triangles will be dominated by the charge state which is slowest to decay.

Now you need to optimize spin blockade. For bias voltages  $V_{sd} \sim \pm 400$   $\mu$ V, attempt to reproduce the data shown in Figure 1.4. If you can't find spin blockade at the (1,1)-(0,2) transition, try the (0,2)-(1,1) transition. For spin readout, you will need an exchange energy

of at least  $J_{02} \sim 300 \mu\text{V}$ . If  $J_{02}$  is too small, you may be able to tune it to a higher value by adjusting gate voltages.

I never got beyond this point with a quadruple dot, but have tuned up several double dots, so I can make an educated guess what the next steps would be. To demonstrate spin readout, apply the pulse schemes of [65] or [40] and look for the pulse triangle in charge sensing, taking care not to be confused by latching. Often the clearest signal is due to the S-T+ degeneracy [40], which gives a sharp line in gate voltage space with unmistakable field dependence. The visibility of the pulse triangle can often be improved by tweaking gate voltages.

The last step of tuning is to measure coherent exchange oscillations. For these to show up, the intra-dot tunnel coupling needs to be fairly large. A good way to measure it is by measuring the field difference of the S-T<sub>+</sub> degeneracy; aim to have it broaden out fairly smoothly, as in Figure 3.2(c). Experiment with various pulse parameters within the scheme of Figure 4A in [40] until the oscillations become clear. Congratulations! You have achieved what eluded me for nearly two years.

## Appendix C

# Synchronizing two Tektronix AWG520s

When running an experiment involving more than two pulsed gates, synchronizing the pulses becomes an issue. Recently Tektronix introduced the AWG5014, whose automatically synchronized outputs solve the problem for up to four gates (at a price). I have also devised a technique to synchronize at least four (and probably arbitrary many) AWG520 outputs. I sketch it briefly below.

For convenient operation you will need the Igor procedure files `AWGhighlevel.ipf`, `AWGPtmanipW.ipf`, `AWGsequencesW.ipf`, `AWG520W.ipf`, `AWG520DictW.ipf`, `AWG710W.ipf` and `AWG710DictW.ipf`, available on the Marcuslab Wiki. I will explain briefly what the key steps are.

Begin by synchronizing the clock frequencies of your AWGs by running an external 10 MHz reference (for example from an HP3325A) into the 10MHZ REF IN ports of your AWGs. Then choose one of your AWGs as the master, and run one of its marker channels (arbitrarily chosen) to the TRIG IN port of the slave(s). Setting the `model` variable to 2520, run the Igor command `InitAWG()` in the file `AWGhighlevelW.ipf`, available on the MarcusLab Wiki. This will set the AWG clocks to use the reference signal, and set the slave(s) to generate externally triggered output.

Edit the pulse table, which specifies the output waveform, so that the marker channel that supplies the trigger is set to 1 during the last pulse step and 0 during the rest of the cycle. To output pulses, run `setpulsesAWG()`. This will upload the pulse table waveform to the AWGs. For triggered operation, it will automatically rotate the slave waveform forward by the trigger delay (typically 31 ns, although you may have to tweak this depending on cable lengths.)

Your AWGs will now be synchronized within one clock cycle. The largest source of remaining asynchronicity is that the length of the trigger cable does not correspond to an integer number of clock cycles. To correct for this, examine the outputs of master and slave on an oscilloscope while adjusting the marker delay of the master to bring them into alignment. By this technique, synchronicity of  $\sim 70$  ps should be achievable.

# Bibliography

- [1] A. Romito and Y. Gefen, *Weak values of electron spin in a double quantum dot*, Phys. Rev. Lett. **100**, 4 (2008).
- [2] N. Katz, M. Neeley, M. Ansmann, R. C. Bialczak, M. Hofheinz, E. Lucero, A. O'Connell, H. Wang, A. N. Cleland, J. M. Martinis, and A. N. Korotkov, *Reversal of the weak measurement of a quantum state in a superconducting phase qubit*, Phys. Rev. Lett. **101**, 200401 (2008).
- [3] I. T. Vink, K. C. Nowack, F. H. L. Koppens, J. Danon, Y. V. Nazarov, and L. M. K. Vandersypen, *Locking electron spins into magnetic resonance by electron-nuclear feed-back*, Nat Phys **5**, 764 (2009).
- [4] D. J. Reilly, J. M. Taylor, E. A. Laird, J. R. Petta, C. M. Marcus, M. P. Hanson, and A. C. Gossard, *Measurement of temporal correlations of the Overhauser field in a double quantum dot*, Phys. Rev. Lett. **101**, 236803 (2008).
- [5] J. A. Jones, S. D. Karlen, J. Fitzsimons, A. Ardavan, S. C. Benjamin, G. A. D. Briggs, and J. J. L. Morton, *Magnetic field sensing beyond the standard quantum limit using 10-spin NOON states*, Science **324**, 1166 (2009).

- [6] M. A. Nielsen and I. A. Chuang, *Quantum Computation and Quantum Information* (Cambridge University Press, 2000).
- [7] N. D. Mermin, *Quantum Computer Science* (Cambridge University Press, 2007).
- [8] R. Hanson, L. P. Kouwenhoven, J. R. Petta, S. Tarucha, and L. M. K. Vandersypen, *Spins in few-electron quantum dots*, Rev Mod Phys **79**, 1217 (2007).
- [9] D. Loss and D. P. DiVincenzo, *Quantum computation with quantum dots*, Phys. Rev. A **57**, 120 (1998).
- [10] P. Shor, *Algorithms for quantum computation: Discrete logarithms and factoring*, in *Proceedings, 35th Annual Symposium on Foundations of Computer Science* (1994).
- [11] L. Grover, *Quantum mechanics helps in searching for a needle in a haystack*, Phys. Rev. Lett. **79**, 325 (1997).
- [12] D. P. DiVincenzo, *2-bit gates are universal for quantum computation*, Phys. Rev. A **51**, 1015 (1995).
- [13] A. Barenco, *A universal 2-bit gate for quantum computation*, P Roy Soc Lond A Mat **449**, 679 (1995).
- [14] A. Kitaev, *Quantum computations: algorithms and error correction*, Russ Math Surv+ **52**, 1191 (1997).
- [15] A. Steane, *Multiple-particle interference and quantum error correction*, P Roy Soc Lond A Mat **452**, 2551 (1996).
- [16] D. P. DiVincenzo and D. Loss, *Quantum information is physical*, Superlattice Microst **23**, 419 (1998).

- [17] F. H. L. Koppens, C. Buizert, K. J. Tielrooij, I. T. Vink, K. C. Nowack, T. Meunier, L. P. Kouwenhoven, and L. M. K. Vandersypen, *Driven coherent oscillations of a single electron spin in a quantum dot*, *Nature* **442**, 766 (2006).
- [18] J. Elzerman, R. Hanson, L. van Beveren, B. Witkamp, L. Vandersypen, and L. P. Kouwenhoven, *Single-shot read-out of an individual electron spin in a quantum dot*, *Nature* **430**, 431 (2004).
- [19] C. Barthel, D. J. Reilly, C. M. Marcus, M. P. Hanson, and A. C. Gossard, *Rapid single-shot measurement of a singlet-triplet qubit*, *Phys. Rev. Lett.* **103**, 160503 (2009).
- [20] A. C. Johnson, *Charge sensing and spin dynamics in GaAs quantum dots*, Ph.D. Thesis, Harvard University (2005).
- [21] A. G. A. Huibers, *Electron transport and dephasing in semiconductor quantum dots*, Ph.D. Thesis, Harvard University (1999).
- [22] T. Drummond, W. T. Masselink, and H. Morcok, *Modulation-doped GaAs/(Al,Ga)As heterojunction field-effect transistors - modfets*, *P IEEE* **74**, 773 (1986).
- [23] B. J. van van Wees, L. P. Kouwenhoven, C. J. P. M. Harmans, J. Williamson, C. Timmering, M. Broekaart, C. Foxon, and J. Harris, *Observation of zero-dimensional states in a one-dimensional electron interferometer*, *Phys. Rev. Lett.* **62**, 2523 (1989).
- [24] L. P. Kouwenhoven, C. M. Marcus, P. L. McEuen, S. Tarucha, R. M. Westervelt, and N. S. Wingreen, *Electron transport in quantum dots*, in *Mesoscopic Electron Transport* (Kluwer Academic, Dordrecht, 1997).

- [25] C. Buizert, F. H. L. Koppens, M. Pioro-Ladrière, H.-P. Tranitz, I. T. Vink, S. Tarucha, W. Wegscheider, and L. M. K. Vandersypen, *In situ reduction of charge noise in  $GaAs/Al_xGa_{1-x}As$  Schottky-gated devices*, Phys. Rev. Lett. **101**, 1 (2008).
- [26] C. W. J. Beenakker, *Theory of Coulomb-blockade oscillations in the conductance of a quantum dot*, Phys Rev B **44**, 1646 (1991).
- [27] M. Field, C. G. Smith, M. Pepper, D. Ritchie, J. Frost, G. A. C. Jones, and D. Hasko, *Measurements of Coulomb blockade with a noninvasive voltage probe*, Phys. Rev. Lett. **70**, 1311 (1993).
- [28] J. R. Petta, A. C. Johnson, C. M. Marcus, M. Hanson, and A. C. Gossard, *Mnipulation of a single charge in a double quantum dot*, Phys. Rev. Lett. **93**, 186802 (2004).
- [29] W. G. V. D. Wiel, S. D. Franceschi, J. Elzerman, T. Fujisawa, S. Tarucha, and L. P. Kouwenhoven, *Electron transport through double quantum dots*, Rev Mod Phys **75**, 1 (2003).
- [30] J. Elzerman, R. Hanson, J. S. Greidanus, L. H. W. V. Beveren, S. D. Franceschi, L. M. K. Vandersypen, S. Tarucha, and L. P. Kouwenhoven, *Few-electron quantum dot circuit with integrated charge read out*, Phys Rev B **67**, 4 (2003).
- [31] A. C. Johnson, J. R. Petta, and C. M. Marcus, *Singlet-triplet spin blockade and charge sensing in a few-electron double quantum dot*, Phys Rev B **72**, 7 (2005).
- [32] E. Lieb and D. Mattis, *Ordering energy levels of interacting spin systems*, J Math Phys **3**, 749 (1962).

- [33] K. Ono, *Current rectification by Pauli exclusion in a weakly coupled double quantum dot system*, Science **297**, 1313 (2002).
- [34] A. Abragam, *Principles of Nuclear Magnetism* (Oxford Science Publications, 1961).
- [35] J. J. Sakurai, *Modern Quantum Mechanics* (Addison Wesley Longman, 1994).
- [36] K. Il'in, M. Siegel, A. Semenov, A. Engel, and H.-W. Hübers, *Critical current of Nb and NbN thin-film structures: The cross-section dependence*, phys. stat. sol. (c) **2**, 1680 (2005).
- [37] S. Amasha, *Toward the manipulation of a single spin in an AlGaAs/GaAs single-electron transistor*, Proc. of SPIE **6244**, 624419 (2006).
- [38] J. Levy, *Universal quantum computation with spin-1/2 pairs and Heisenberg exchange*, Phys. Rev. Lett. **89**, 147902 (2002).
- [39] J. M. Taylor, H.-A. Engel, W. Dür, A. Yacoby, C. M. Marcus, P. Zoller, and M. D. Lukin, *Fault-tolerant architecture for quantum computation using electrically controlled semiconductor spins*, Nat Phys **1**, 177 (2005).
- [40] J. R. Petta, A. C. Johnson, J. M. Taylor, E. A. Laird, A. Yacoby, M. D. Lukin, C. M. Marcus, M. P. Hanson, and A. C. Gossard, *Coherent manipulation of coupled electron spins in semiconductor quantum dots*, Science **309**, 2180 (2005).
- [41] S. Foletti, H. Bluhm, D. Mahalu, V. Umansky, and A. Yacoby, *Universal quantum control of two-electron spin quantum bits using dynamic nuclear polarization*, Nat Phys **5**, 1 (2009).

- [42] E. A. Laird, C. Barthel, E. I. Rashba, C. M. Marcus, M. P. Hanson, and A. C. Gossard, *Hyperfine-mediated gate-driven electron spin resonance*, Phys. Rev. Lett. **99**, 246601 (2007).
- [43] E. A. Laird, C. Barthel, E. I. Rashba, C. M. Marcus, M. P. Hanson, and A. C. Gossard, *A new mechanism of electric dipole spin resonance: hyperfine coupling in quantum dots*, Semicond. Sci. Technol. **24**, 064004 (2009).
- [44] E. I. Rashba, *Properties of semiconductors with an extremum loop: 1. Cyclotron and combinational resonance in a magnetic field perpendicular to the plane of the loop*, Sov. Phys. Sol. State. **2**, 1109 (1960).
- [45] R. Bell, *Electric dipole spin transitions in InSb*, Phys. Rev. Lett. **9**, 52 (1962).
- [46] B. McCombe, S. Bishop, and R. Kaplan, *Combined resonance and electron g-values in InSb*, Phys. Rev. Lett. **18**, 748 (1967).
- [47] E. I. Rashba and V. I. Sheka, *Landau Level Spectroscopy* (Elsevier Science Publishers, 1991).
- [48] F. Jelezko, T. Gaebel, I. Popa, A. Gruber, and J. Wrachtrup, *Observation of coherent oscillations in a single electron spin*, Phys. Rev. Lett. **92**, 076401 (2004).
- [49] D. Rugar, R. Budakian, H. J. Mamin, and B. W. Chui, *Single spin detection by magnetic resonance force microscopy*, Nature **430**, 329 (2004).
- [50] M. Xiao, I. Martin, E. Yablonovitch, and H. Jiang, *Electrical detection of the spin resonance of a single electron in a silicon field-effect transistor*, Nature **430**, 435 (2004).

- [51] S. I. Pekar and E. I. Rashba, *Combined resonance in crystals in inhomogeneous magnetic fields*, Sov. Phys. - JETP **20**, 1295 (1965).
- [52] Y. Kato, R. Myers, D. C. Driscoll, A. C. Gossard, J. Levy, and D. Awschalom, *Giga-hertz electron spin manipulation using voltage-controlled g-tensor modulation*, Science **299**, 1201 (2003).
- [53] Y. Tokura, W. G. V. D. Wiel, T. Obata, and S. Tarucha, *Coherent single electron spin control in a slanting Zeeman field*, Phys. Rev. Lett. **96**, 4 (2006).
- [54] V. N. Golovach, M. Borhani, and D. Loss, *Electric-dipole-induced spin resonance in quantum dots*, Phys Rev B **74**, 10 (2006).
- [55] K. C. Nowack, F. H. L. Koppens, Y. V. Nazarov, and L. M. K. Vandersypen, *Coherent control of a single electron spin with electric fields*, Science **318**, 1430 (2007).
- [56] M. Pioro-Ladrière, T. Obata, Y. Tokura, Y. S. Shin, T. Kubo, K. Yoshida, T. Taniyama, and S. Tarucha, *Electrically driven single-electron spin resonance in a slanting Zeeman field*, Nat Phys **4**, 776 (2008).
- [57] H.-A. Engel and D. Loss, *Detection of single spin decoherence in a quantum dot via charge currents*, Phys. Rev. Lett. **86**, 4648 (2001).
- [58] M. Gueron and C. Ryter, *Overhauser effect in metallic lithium*, Phys. Rev. Lett. **3**, 338 (1959).
- [59] M. Dobers, K. V. Klitzing, J. Schneider, G. Weimann, and K. H. Ploog, *Electrical detection of nuclear magnetic-resonance in  $GaAs-Al_xGa_{1-x}As$  heterostructures*, Phys. Rev. Lett. **61**, 1650 (1988).

- [60] J. Baugh, Y. Kitamura, K. Ono, and S. Tarucha, *Large nuclear overhauser fields detected in vertically coupled double quantum dots*, Phys. Rev. Lett. **99**, 4 (2007).
- [61] M. S. Rudner and L. S. Levitov, *Electrically driven reverse Overhauser pumping of nuclear spins in quantum dots*, Phys. Rev. Lett. **99**, 4 (2007).
- [62] D. Goldhaber-Gordon, H. Shtrikman, D. Mahalu, D. Abusch-Magder, U. Meirav, and M. Kastner, *Kondo effect in a single-electron transistor*, Nature **391**, 156 (1998).
- [63] R. Hanson, B. Witkamp, L. M. K. Vandersypen, L. H. W. V. Beveren, J. Elzerman, and L. P. Kouwenhoven, *Zeeman energy and spin relaxation in a one-electron quantum dot*, Phys. Rev. Lett. **91**, 196802 (2003).
- [64] F. H. L. Koppens, J. A. Folk, J. Elzerman, R. Hanson, L. H. W. V. Beveren, I. T. Vink, H.-P. Tranitz, W. Wegscheider, L. P. Kouwenhoven, and L. M. K. Vandersypen, *Control and detection of singlet-triplet mixing in a random nuclear field*, Science **309**, 1346 (2005).
- [65] A. C. Johnson, J. R. Petta, J. M. Taylor, A. Yacoby, M. D. Lukin, C. M. Marcus, M. P. Hanson, and A. C. Gossard, *Triplet-singlet spin relaxation via nuclei in a double quantum dot*, Nature **435**, 925 (2005).
- [66] K. Ono and S. Tarucha, *Nuclear-spin-induced oscillatory current in spin-blockaded quantum dots*, Phys. Rev. Lett. **92**, 256803 (2004).
- [67] L. Khazan, Y. Rubo, and V. Sheka, *Exchange-induced optical spin transitions in semimagnetic semiconductors*, Phys Rev B **47**, 13180 (1993).

- [68] E. A. Laird, J. R. Petta, A. C. Johnson, C. M. Marcus, A. Yacoby, M. P. Hanson, and A. C. Gossard, *Effect of exchange interaction on spin dephasing in a double quantum dot*, Phys. Rev. Lett. **97**, 4 (2006).
- [69] E. I. Rashba, *Theory of electric dipole spin resonance in quantum dots: Mean field theory with Gaussian fluctuations and beyond*, Phys Rev B **78**, 195302 (2008).
- [70] I. A. Merkulov, *Electron spin relaxation by nuclei in semiconductor quantum dots*, Phys Rev B **65**, 8 (2002).
- [71] L. S. Levitov and E. I. Rashba, *Dynamical spin-electric coupling in a quantum dot*, Phys Rev B **67**, 5 (2003).
- [72] I. Rabi, *Space quantization in a gyrating magnetic field*, Phys Rev **51**, 0652 (1937).
- [73] F. H. L. Koppens, D. Klauser, W. A. Coish, K. C. Nowack, L. P. Kouwenhoven, D. Loss, and L. M. K. Vandersypen, *Universal phase shift and nonexponential decay of driven single-spin oscillations*, Phys. Rev. Lett. **99**, 106803 (2007).
- [74] D. Paget, G. Lampel, B. Sapoval, and V. Safarov, *Low field electron-nuclear spin coupling in gallium-arsenide under optical-pumping conditions*, Phys Rev B **15**, 5780 (1977).
- [75] L. Dicarlo, H. Lynch, A. C. Johnson, L. I. Childress, K. Crockett, C. M. Marcus, M. Hanson, and A. C. Gossard, *Differential charge sensing and charge delocalization in a tunable double quantum dot*, Phys. Rev. Lett. **92**, 226801 (2004).
- [76] A. Khaetskii, D. Loss, and L. Glazman, *Electron spin decoherence in quantum dots due to interaction with nuclei*, Phys. Rev. Lett. **88**, 186802 (2002).
- [77] A. Overhauser, *Polarization of nuclei in metals*, Phys Rev **91**, 476 (1953).

- [78] M. Pioro-Ladrière, Y. Tokura, T. Obata, T. Kubo, and S. Tarucha, *Micromagnets for coherent control of spin-charge qubit in lateral quantum dots*, Appl. Phys. Lett. **90**, 024105 (2007).
- [79] P. Franken, G. Weinreich, C. Peters, and A. Hill, *Generation of optical harmonics*, Phys. Rev. Lett. **7**, 118 (1961).
- [80] A. De, C. E. Pryor, and M. E. Flatte, *Electric-field control of a hydrogenic donor's spin in a semiconductor*, Phys. Rev. Lett. **102**, 017603 (2009).
- [81] T. Fujisawa, D. Austing, Y. Tokura, Y. Hirayama, and S. Tarucha, *Allowed and forbidden transitions in artificial hydrogen and helium atoms*, Nature **419**, 278 (2002).
- [82] A. S. Bracker, E. A. Stinaff, D. Gammon, M. E. Ware, J. G. Tischler, A. Shabaev, A. L. Efros, D. Park, D. Gershoni, V. L. Korenev, and I. A. Merkulov, *Optical pumping of the electronic and nuclear spin of single charge-tunable quantum dots*, Phys. Rev. Lett. **94**, 4 (2005).
- [83] P.-F. Braun, X. Marie, L. Lombez, B. Urbaszek, T. Amand, P. Renucci, V. K. Kalevich, K. V. Kavokin, O. Krebs, P. Voisin, and Y. Masumoto, *Direct observation of the electron spin relaxation induced by nuclei in quantum dots*, Phys. Rev. Lett. **94**, 4 (2005).
- [84] R. Hanson, L. H. W. V. Beveren, I. T. Vink, J. Elzerman, W. J. M. Naber, F. H. L. Koppens, L. P. Kouwenhoven, and L. M. K. Vandersypen, *Single-shot readout of electron spin states in a quantum dot using spin-dependent tunnel rates*, Phys. Rev. Lett. **94**, 4 (2005).

- [85] S. Erlingsson, Y. Nazarov, and V. Fal'ko, *Nucleus-mediated spin-flip transitions in gaas quantum dots*, Phys Rev B **64**, art. no. (2001).
- [86] N. Turro, *Influence of nuclear-spin on chemical-reactions - magnetic isotope and magnetic-field effects (a review)*, P Natl Acad Sci Usa **80**, 609 (1983).
- [87] A. Buchachenko, *Magnetic isotope effect: Nuclear spin control of chemical reactions*, J Phys Chem A **105**, 9995 (2001).
- [88] H. Staerk, W. Kuhnle, R. Treichel, and A. Weller, *Magnetic-field dependence of intramolecular exciplex formation in polymethylene-linked A-D systems*, Chem Phys Lett **118**, 19 (1985).
- [89] V. Tarasov, N. Ghatlia, A. Buchachenko, and N. Turro, *Probing the exchange interaction through micelle size: 1. Probability of recombination of triplet geminate radical pairs*, J Am Chem Soc **114**, 9517 (1992).
- [90] W. A. Coish and D. Loss, *Singlet-triplet decoherence due to nuclear spins in a double quantum dot*, Phys Rev B **72**, 12 (2005).
- [91] J. R. Petta, A. C. Johnson, A. Yacoby, C. M. Marcus, M. Hanson, and A. C. Gossard, *Pulsed-gate measurements of the singlet-triplet relaxation time in a two-electron double quantum dot*, Phys Rev B **72**, 161301 (2005).
- [92] D. M. Zumbuhl, C. M. Marcus, M. Hanson, and A. C. Gossard, *Cotunneling spectroscopy in few-electron quantum dots*, Phys. Rev. Lett. **93**, 256801 (2004).
- [93] D. P. DiVincenzo, D. Bacon, J. Kempe, G. Burkard, and K. Whaley, *Universal quantum computation with the exchange interaction*, Nature **408**, 339 (2000).

- [94] E. Step, A. Buchachenko, and N. Turro, *Paramagnetic interactions of triplet radical pairs with nitroxide radicals - an antiscavenging effect*, J Am Chem Soc **116**, 5462 (1994).
- [95] A. Buchachenko and V. Berdinsky, *Electron spin catalysis*, Chem Rev **102**, 603 (2002).
- [96] L. Gaudreau, S. A. Studenikin, A. S. Sachrajda, P. Zawadzki, A. Kam, J. Lapointe, M. Korkusinski, and P. Hawrylak, *Stability diagram of a few-electron triple dot*, Phys. Rev. Lett. **97**, 4 (2006).
- [97] D. Schröer, A. D. Greentree, L. Gaudreau, K. Eberl, L. C. L. Hollenberg, J. P. Kotthaus, and S. Ludwig, *Electrostatically defined serial triple quantum dot charged with few electrons*, Phys Rev B **76**, 11 (2007).
- [98] L. Gaudreau, A. Kam, G. Granger, S. A. Studenikin, P. Zawadzki, and A. S. Sachrajda, *A tuneable few electron triple quantum dot*, arXiv:0907.1322v1 (2009).
- [99] G. Toth and C. Lent, *Quantum computing with quantum-dot cellular automata*, Phys. Rev. A **63**, 052315 (2001).
- [100] L. Gaudreau, A. S. Sachrajda, S. A. Studenikin, P. Zawadzki, and A. Kam, *Spin blockade of quantum cellular automata effects in a few electron triple quantum dot*, Physica E **40**, 978 (2008).
- [101] T. Stevenson, F. Pellerano, C. Stahle, K. Aidala, and R. J. Schoelkopf, *Multiplexing of radio-frequency single-electron transistors*, Appl. Phys. Lett. **80**, 3012 (2002).
- [102] D. J. Reilly, C. M. Marcus, M. P. Hanson, and A. C. Gossard, *Fast single-charge sensing with a rf quantum point contact*, Appl. Phys. Lett. **91**, 162101 (2007).

- [103] J. M. Taylor, J. R. Petta, A. C. Johnson, A. Yacoby, C. M. Marcus, and M. D. Lukin, *Relaxation, dephasing, and quantum control of electron spins in double quantum dots*, Phys Rev B **76**, 1 (2007).
- [104] G. Shinkai, T. Hayashi, Y. Hirayama, and T. Fujisawa, *Controlled resonant tunneling in a coupled double-quantum-dot system*, Appl. Phys. Lett. **90**, 103116 (2007).
- [105] F. Perez-Martinez, I. Farrer, D. Anderson, G. A. C. Jones, D. A. Ritchie, S. J. Chorley, and C. G. Smith, *Demonstration of a quantum cellular automata cell in a GaAs/AlGaAs heterostructure*, Appl. Phys. Lett. **91**, 032102 (2007).
- [106] K. D. Petersson, C. G. Smith, D. Anderson, P. Atkinson, G. A. C. Jones, and D. A. Ritchie, *Microwave-driven transitions in two coupled semiconductor charge qubits*, Phys. Rev. Lett. **103**, 016805 (2009).
- [107] D. Austing, S. Sasaki, S. Tarucha, S. Reimann, M. Koskinen, and M. Manninen, *Ellipsoidal deformation of vertical quantum dots*, Phys Rev B **60**, 11514 (1999).
- [108] M. Switkes, *Decoherence and adiabatic transport in semiconductor quantum dots*, Ph.D. Thesis, Harvard University (1999).
- [109] S. R. Patel, *Electron transport and dephasing in semiconductor quantum dots*, Ph.D. Thesis, Harvard University (2002).
- [110] S. M. Cronenwett, *Coherence, charging and spin effects in quantum dots and point contacts*, Ph.D. Thesis, Harvard University (2001).
- [111] L. DiCarlo, *Mesoscopic electronics beyond dc transport*, Ph.D. Thesis, Harvard University (2007).
- [112] F. Pobell, *Matter and Methods at Low Temperatures* (Springer, 1996).

[113] D. M. Pozar, *Microwave Engineering* (John Wiley, 1988).